

**COMPUTATIONAL ANALYSIS OF ADVANCED COMPOSITE ARMOR
SYSTEMS**

**A THESIS SUBMITTED TO
THE GRADUATE SCHOOL OF NATURAL AND APPLIED SCIENCES
OF
MIDDLE EAST TECHNICAL UNIVERSITY**

BY

BÜLENT BAŞARAN

**IN PARTIAL FULFILLMENT OF THE REQUIREMENTS
FOR
THE DEGREE OF MASTER OF SCIENCE
IN
MECHANICAL ENGINEERING**

SEPTEMBER 2007

Approval of the thesis:

**COMPUTATIONAL ANALYSIS OF ADVANCED COMPOSITE ARMOR
SYSTEMS**

submitted by **Bülent BAŞARAN** in partial fulfillment of the requirements for the degree of **Master of Science in Mechanical Engineering, Middle East Technical University** by,

Prof. Dr. Canan ÖZGEN
Dean, Graduate School of **Natural and Applied Sciences**

Prof. Dr. Kemal İDER
Head of Department, **Mechanical Engineering**

Prof. Dr. Levend PARNAS
Supervisor, **Mechanical Engineering, METU**

Examining Committee Members:

Prof. Dr. M.A.Sahir ARIKAN.
Mechanical Engineering, METU

Prof. Dr. Levend PARNAS
Mechanical Engineering, METU

Prof. Dr. R.Orhan YILDIRIM
Mechanical Engineering, METU

Asst.Prof. Dr. Serkan DAĞ
Mechanical Engineering, METU

Fikret ŞENEL
Barış Elektrik Endüstrisi A.Ş.

Date: **17 September 2007**

I hereby declare that all information in this document has been obtained and presented in accordance with academic rules and ethical conduct. I also declare that, as required by these rules and conduct, I have fully cited and referenced all material and results that are not original to this work.

Name, Last Name: Bülent BAŞARAN

Signature :

ABSTRACT

COMPUTATIONAL ANALYSIS OF ADVANCED COMPOSITE ARMOR SYSTEMS

BAŞARAN, Mustafa Bülent

M.Sc., Department of Mechanical Engineering

Supervisor: Prof. Dr. Levend PARNAS

September 2007, (116 Pages)

Achieving light weight armor design has become an important engineering challenge in the last three decades. As weapons becoming highly sophisticated, so does the ammunition, potential targets have to be well protected against such threats. In order to provide mobility, light and effective armor protection materials should be used.

In this thesis, numerical simulation of the silicon carbide armor backed by KevlarTM composite and orthogonally impacted by 7.62mm armor piercing (AP) projectile at an initial velocity of 850 m/s is analyzed by using AUTODYN hydrocode. As a first step, ceramic material behavior under impact conditions is validated numerically by comparing the numerical simulation result with the test result which is obtained from the literature. Then, different numerical simulations are performed by changing the backing material thickness, i.e. 2, 4, 6 and 8mm, while the thickness of the ceramic is held constant, i.e. 8mm. At the end of the simulations, optimum ceramic/composite thickness ratio is sought.

The results of the simulations showed that for the backing thickness values of 4, 6 and 8mm, the projectile could not perforate the armor system. On the contrary, the projectile could penetrate and perforate the armor system for the backing thickness value of 2mm and it has still some residual velocity. From these results,

it is inferred that the optimum ceramic/composite thickness ratio is equal to about 2 for the silicon carbide and kevlar configuration.

Keywords: Composite armor, numerical impact simulation, silicon carbide, kevlar, aramid, ceramic/composite thickness ratio.

ÖZ

İLERİ KOMPOZİT ZIRH SİSTEMLERİNİN HESAPLAMALI YÖNTEMLERLE ANALİZİ

BAŞARAN, Mustafa Bülent

Yüksek Lisans, Makine Mühendisliği Ana Bilim Dalı

Tez Yöneticisi: Prof. Dr. Levend PARNAS

Eylül 2007, (116 Sayfa)

Hafif zırh tasarımı son otuz yılda mühendisliğin önemli bir dalı olmuştur. Silahlar ve kullanılan mühimmat geliştikçe araçların da bu tehditlere karşı daha iyi korunması gereği ortaya çıkmıştır. Araçların hareket kabiliyetinin korunması için hem hafif hem de etkin zırh malzemelerinin kullanılması gerekmektedir.

Bu çalışmada AUTODYN programı kullanılarak 850 m/s'lik ilk hız verilmiş olan 7.62mm zırh delici mermi çarptırılan KevlarTM ile güçlendirilmiş silikon karbür zırhın nümerik benzeşim analizi yapılmıştır. İlk olarak, darbeye maruz kalan seramik malzeme davranışı, nümerik analiz sonuçlarının literatürden bulunan test sonuçlarıyla karşılaştırılmasıyla doğrulanmıştır. Daha sonra sabit kalınlıktaki (8mm) seramik malzemesi kullanılarak ve destek malzeme kalınlığı değiştirilerek (2, 4, 6, 8mm) değişik nümerik simülasyonlar yapılmış ve optimum seramik/kompozit kalınlık oranı incelenmiştir. Simülasyon sonuçları göstermiştir ki; 4, 6 ve 8mm kalınlığındaki destek plakaya sahip zırh sistemi atılan mermi tarafından delinememiştir. Ancak, 2mm destek plaka kalınlığına sahip olan zırh sistemi mermi tarafından delinebilmiştir ve bu delinme sonrasında merminin hala belirli bir hıza sahip olduğu görülmüştür. Bu sonuçlar ışığında, silikon karbür ve kevlar zırh birleşimi için optimum seramik/kompozit kalınlık oranı yaklaşık 2 olarak bulunmuştur.

Anahtar Kelimeler: Kompozit zırh, sayısal darbe simülasyonu, silikon karbür, kevlar, aramid, seramik/kompozit kalınlık oranı.

To My Family

ACKNOWLEDGEMENTS

I would like to express my sincere appreciation to my thesis supervisor Prof. Dr. Levend PARNAS and Fikret ŐENEL for their supervision and suggestions during the course of my thesis study.

I would like to thank my colleagues at ASELSAN for their support.

I would also like to thank my friend BaŐar YALŐINER from FİGES A.Ő. for his help.

I want to give my deepest thanks to my dear family for their endless support and encouragements.

Finally, many thanks to my fiancée İrem ŐZDEMİR for her continuous help and encouragement.

TABLE OF CONTENTS

PLAGIARISM.....	iii
ABSTRACT	iv
ÖZ.....	vi
ACKNOWLEDGEMENTS	ix
TABLE OF CONTENTS	x
LIST OF TABLES	xii
LIST OF FIGURES.....	xiii
LIST OF ABBREVIATIONS	xvi
NOMENCLATURE	xvii
1 INTRODUCTION.....	1
1.1 Motivation	1
1.2 Impact Event.....	6
1.3 Literature Survey.....	8
1.3.1 Mechanics.....	8
1.3.2 Analytical Models	13
1.3.3 Numerical Studies	14
1.4 Scope of the Study.....	18
2 PROBLEM DEFINITION	19
2.1 Introduction	19
2.2 Impact Theory	19
2.3 Shock Waves in Solids	28
2.3.1 Conservation Equations Under Shock Loading	32
2.4 Mechanics of Composite Materials.....	33
2.4.1 Definitions	34
2.4.2 Impact Damage Modeling of Composites.....	38
3 NUMERICAL ANALYSIS OF THE BALLISTIC IMPACT PROBLEM	42
3.1 Introduction	42
3.2 Finite Element Analysis of the Impact Event.....	43

3.2.1 Nonlinear Dynamic Problems and Explicit Method	43
3.3 Theory Behind the Numerical Analysis	47
3.3.1 Conservation of Mass	47
3.3.2 Conservation of Momentum.....	48
3.3.3 Conservation of Energy	50
3.3.4 Material Model	50
3.3.5 Failure Models.....	57
3.3.6 Lagrange Meshes.....	58
3.3.7 Time Step	60
3.3.8 Smoothed Particle Hydrodynamics (SPH) Solver.....	60
3.4 Description of the Material Models Used In Numerical Simulations	63
3.4.1 Johnson-Cook Strength Model For The Projectile.....	63
3.4.2 Johnson-Cook Failure Model For The Projectile	64
3.4.3 Johnson-Holmquist (JH) Strength Model For The Ceramic Armor..	65
3.4.4 Johnson-Holmquist (JH) Fracture Model For The Ceramic Armor..	67
3.4.5 Orthotropic Material Model For The Composite Armor.....	70
3.4.6 Orthotropic Failure Model For The Composite Armor.....	75
3.5 Validation of Material Models	77
3.5.1 Validation of Ceramic Model.....	77
3.5.2 Validation of Kevlar TM Model.....	87
3.6 Numerical Simulations of the Advanced Composite Armor.....	88
3.6.1 Finite Element Models of the Armor System and the Projectile.....	89
3.6.2 Numerical Results	93
4 DISCUSSION AND CONCLUSION	106
4.1 Discussion of Results	106
4.2 Conclusion.....	108
REFERENCES	110

LIST OF TABLES

Table 1.1 Material properties of various metals and ceramics	2
Table 1.2 Impact response of materials	4
Table 3.1 Material properties and constants for SiC	80
Table 3.2 Material properties and constants for 4340 steel.....	81
Table 3.3 Number of elements for backing plates.....	91
Table 3.4 Material properties and constants for Kevlar TM plate	92
Table 4.1 Areal densities of different configuration of the armor system.....	109

LIST OF FIGURES

Figure 1.1 Florence impact model.....	5
Figure 1.2 Mechanisms of penetration of armor.	7
Figure 1.3 Fracture conoid formation.....	9
Figure 2.1 Nomenclature for rod element.	25
Figure 2.2 Strain distribution in a rod produced by constant velocity impact at end	27
Figure 2.3 Details of uniaxial strain behavior.	30
Figure 2.4 Regions of elastic, elasto-plastic and shock wave propagation.	31
Figure 2.5 Progress of a plane shock wave.	32
Figure 2.6 Definition of isotropic and anisotropic materials.....	34
Figure 2.7 Response of an orthotropic plate by the impact of an non-rigid striker	41
Figure 3.1 Mass-Spring-Damper system.....	44
Figure 3.2 Displacement versus time graph.	45
Figure 3.3 Material deformation histories.....	51
Figure 3.4 Yield criteria.	55
Figure 3.5 Phase Diagram, Hugoniot and Adiabats.	56
Figure 3.6 Lagrange subgrid.	58
Figure 3.7 Calculation cycle.....	59
Figure 3.8 Rod of steel with SPH particles.	61
Figure 3.9 Calculation cycle (SPH).....	62
Figure 3.10 JH-1 Strength Model.....	66
Figure 3.11 JH-1 Damage Model.	66
Figure 3.12 Pressure-volumetric strain.	67
Figure 3.13 Typical in-plane stress-strain behavior of Kevlar TM -epoxy.....	70
Figure 3.14 Schematic illustration of crack softening algorithm.	76
Figure 3.15 Edge-on impact (quarter) model.	77
Figure 3.16 Edge-on impact (full) model.	78
Figure 3.17 Meshed (quarter) model.	79

Figure 3.18 Damage velocity versus impact velocity.	82
Figure 3.19 Damage plot for initial velocity of 400 m/s at 4.0 μ s.	83
Figure 3.20 Damage plot for initial velocity of 400 m/s at 6.0 μ s.	83
Figure 3.21 Damage plot for initial velocity of 700 m/s at 4.0 μ s.	84
Figure 3.22 Damage plot for initial velocity of 700 m/s at 6.0 μ s.	84
Figure 3.23 Damage plot for initial velocity of 900 m/s at 4.0 μ s.	85
Figure 3.24 Damage plot for initial velocity of 900 m/s at 6.0 μ s.	85
Figure 3.25 Simulated Damage Development.	87
Figure 3.26 Back surface velocity.	88
Figure 3.27 Finite element model (half model) of the composite armor system .	89
Figure 3.28 Finite element model (half model) of the projectile	90
Figure 3.29 Principal material directions for the composite	91
Figure 3.30 Progress of the damage for configuration C1	94
Figure 3.31 Progress of the damage for configuration C2	95
Figure 3.32 Progress of the damage for configuration C3	96
Figure 3.33 Progress of the damage for configuration C4	97
Figure 3.34 Velocity history of the projectile for configuration C1.....	98
Figure 3.35 Velocity history of the projectile for configuration C2.....	98
Figure 3.36 Velocity history of the projectile for configuration C3.....	99
Figure 3.37 Velocity history of the projectile for configuration C4.....	99
Figure 3.38 Crack propagation on the rear side of the ceramic tile for configuration C1	101
Figure 3.39 Crack propagation on the rear side of the ceramic tile for configuration C2.....	102
Figure 3.40 Crack propagation on the rear side of the ceramic tile for configuration C3.....	102
Figure 3.41 Crack propagation on the rear side of the ceramic tile for configuration C4.....	103
Figure 3.42 Damage level on the surface of the ceramic tile at the end of the simulation for configuration C1	103
Figure 3.43 Damage level on the surface of the ceramic tile at the end of the simulation for configuration C2	104

Figure 3.44 Damage level on the surface of the ceramic tile at the end of the simulation for configuration C3	104
Figure 3.45 Damage level on the surface of the ceramic tile at the end of the simulation for configuration C4	105

LIST OF ABBREVIATIONS

AFV	Armored fighting vehicles
Al_2O_3	Alumina
AP	Armor piercing
CDM	Continuum damage mechanics
CFRP	Carbon fiber reinforced plastic
EOS	Equation of state
FEA	Finite element analysis
FEM	Finite element method
FSP	Fragment simulating projectile
GFRP	Glass fiber reinforced plastic
HEL	Hugoniot elastic limit
KFRP	Kevlar fiber reinforced plastic
SiC	Silicon carbide
SPH	Smoothed particle hydrodynamics
UTS	Ultimate tensile strength

NOMENCLATURE

A	Yield stress
a_p	Radius of the projectile
B	Hardening coefficient
c	Wave speed
C	Strain rate constant
[C]	Stiffness matrix
c_E	Elastic wave speed
c_p	Plastic wave speed
E	Modulus of elasticity
f_i	Body forces
$F(t)$	Loading distributed force
G	Shear modulus
G_f	Fracture energy
h_1	Thickness of the front plate
h_2	Thickness of the backing plate
K	Bulk modulus
M_p	Mass of the projectile
N	Hardening exponent
P	Pressure
q_{mn}	Load distribution on the plate
[S]	Compliance matrix
S_{fmax}	Maximum fracture strength
S_{ij}	Deviatoric stress components
T^*	Homologous temperature
Δt	Time step
u_i	Components of the displacement vector

U_s	Pressure pulse velocity
u_p	Particle velocity
V_p	Predicted ballistic velocity
w	Natural frequency
w_{mn}	Natural frequencies of the target plate
ε_{ij}	Components of the strain tensor
ε_2	Breaking strain of the backing plate
$\dot{\varepsilon}^*$	Dimensionless plastic strain rate
σ_{ij}	Components of the stress tensor,
σ_2	Ultimate tensile strength of backing plate (UTS)
ρ	Density
ρ_2	Density of the backing plate
ρ_1	Density of the front plate
λ and μ	Lame constants
δ_{ij}	Kronecker's delta
ν	Poisson's ratio
Ψ_x	Shear rotation in x-direction
Ψ_y	Shear rotation in y-direction
ζ	Damping factor
σ_m	Average of the three normal stresses
$\bar{\sigma}$	von Mises equivalent stress
σ_{fail}	Failure stress

CHAPTER 1

INTRODUCTION

1.1 Motivation

People have always attempted to protect themselves against their enemies and the weapons being used, but this has always been balanced by their need to be mobile. The earliest form of armor was not intended to protect any form of transportation but to protect the person. From the middle ages, the foot soldier was protected with some kind of body vest, a helmet and a shield. When the scale of attack was dramatically increased with the advent of fire arms, any form of protection was easily overmatched and it was soon abandoned in favor of the greater mobility given to the individual. When the need for fighting vehicles was arisen, the importance of achieving lightweight protection has also been recognized. [1].

If an ideal armor material is sought, there would be several factors to consider; but the major consideration would be that the armor should be effective. It must do the job it is designed to do, and it should be light. A generally applicable characteristic of armor is areal density, which is defined as the weight per square meter of its area normal to the direction of attack. Areal density ranges from 40 kg/m² for very light vehicles to 3.5 tonnes/m² for the frontal armor of battle tanks [2].

Ceramics are materials that have been extensively used for body armor protection and they are particularly interesting to the vehicle designer as they show most promise as armor protection for light vehicles. They originated in 1960s as protection of US helicopter crews in Vietnam and only began to be used on light

Armored Fighting Vehicles (AFV) around 1990. Table 1.1 shows the density and hardness (Vickers) values of steel (as Rolled Homogenous Armor and Dual Hard Steel Face), aluminum and various ceramic materials. There are several candidate ceramic materials, but the most common are boron carbide, silicon carbide and alumina (aluminum oxide). Armor Piercing (AP) bullet design favors high-density, high-hardness core materials such as tungsten carbide, so in order to shatter bullets made of this material the candidate armor materials must exceed this hardness.

All ceramic materials are extremely hard, but they are also too brittle. They provide protection because extreme hardness causes the projectile to shatter as the ceramic itself shatters. Ceramic materials, as armor, are commonly used as tiles (100x100 mm) so that cracks caused by a hit are confined to one tile, and they are no or very little multi hit capability. They are too brittle to be used by itself so they have to be mounted other types of armor, i.e. the backing plate [2].

Table 1.1 Material properties of various metals and ceramics [2].

Material	Density (kg/m³)	Vickers hardness	Specific hardness
RHA (Rolled Homogeneous Armor)	7850	240-380	0.031-0.048
Dual hard steel, face	7850	600-750	0.076-0.096
7039 aluminum	2780	150	0.054
Alumina 85%	3450	900-970	0.261-0.281
Alumina 99%	3900	1500-1700	0.385-0.436
Silicon carbide	3150	2200-2500	0.698-0.794
Titanium diboride	4250	2500-2700	0.588-0.635
Boron carbide	2450	3000	1.224

If further reduction in weight is desired, as in the case of protection of airplane cockpits or a helicopter seat, it is reasonable to select a backing material that is efficient in ballistic performance and also has low density. Fiber-reinforced composite materials have become an important class of engineering materials over the last three decades, this being due to their outstanding mechanical properties, flexibility in design capabilities, and ease of fabrication. Additional advantages include high strength-to-weight and stiffness-to-weight ratios, good corrosion, wear and impact resistance, and excellent thermal and acoustical insulation. Fiber composites are used routinely in such diverse applications as the automobile, aircraft, piping, offshore and space industries. Due to the light weight of fiber-reinforced plastic materials, they are being used increasingly in the military applications as armor [3].

The modern composite armor, typically consisting of a combination of a hard facing layer of ceramic tiles and a fiber reinforced composite backing plate, is under development to satisfy ballistic and structural requirements, while providing weight savings of approximately 30–40%. The function of the ceramic layer is to deform and erode the projectile and thereby reduce the local pressure in the composite backing plate. The composite layer holds the fragmented ceramic particles while absorbing a significant part of the kinetic energy of the projectile by a variety of deformation processes [4].

Armor design and analysis has been approached from three analysis perspectives, namely: empirically, analytically, and numerically. Empirical analyses generally include tests. These tests regarding penetration and perforation studies can be divided into three main categories when the impact velocity of the projectile is concerned, i.e. V_i , namely low velocity impact ($V_i < 50$ m/s), ordnance velocity regime ($50 < V_i < 1300$ m/s), and finally high velocity penetration ($V_i > 1300$ m/s) [5]. The classification of the penetration and perforation studies is summarized in Table 1.2. However, by its nature the tests are time consuming and are not cost effective. Furthermore experimental approach does not yield detailed information of the impact event; i.e. the history of the projectile, the trends when changing the

configurations of the armor system. Moreover, the complexity of impact problems caused by the high number of involving parameters like relative velocity of impact, shape of impacting objects, dimensions and material characteristics, etc., increases when composite materials are involved, due to the orthotropic properties and distinct failure modes that may occur. [5,6]

Table 1.2 Impact response of materials [7]

$\dot{\epsilon}$	V_i	Effect	Method of Loading
10^8	>12 km/s	Explosive Impact Colliding Solids Vaporized	-
10^6	3-12 km/s	Hydrodynamic Material Compressibility not negligible	Explosive Acceleration
	1-3 km/s	Fluid Behavior in Materials; Pressures Approach or Exceed Material Strength; Density a Dominant Parameter	Powder Guns, Gas Guns
10^4	500-1000 m/s	Viscous-Material Strength Still Significant	Powder Guns
10^2	50-500 m/s	Primarily Plastic	Mechanical Devices, Compressed Air Gun
10^0	<50 m/s	Primarily Elastic Some Local Plasticity	Mechanical Devices, Compressed Air Gun

As with analytical models, the most famous one that deals with two component armors is the Florence model [8]. This model assumes a ceramic hard facing and a ductile backing plate impacted by a rigid projectile. It predicts the protection ballistic limit velocity which is defined as the minimum velocity at which a particular projectile is expected to consistently, completely penetrate armor of

given thickness at a specified angle of obliquity. It is a measurement of the resistance of protective armor to projectile penetration [9].

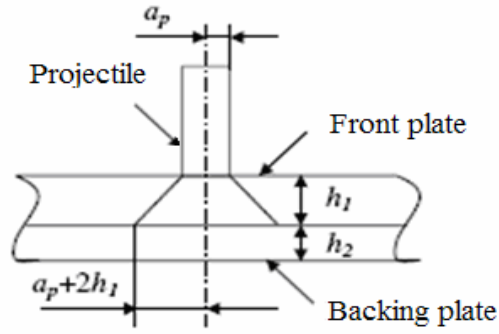


Figure 1.1 Florence impact model [9].

The Florence model is described by:

$$V_p = \sqrt{\frac{\varepsilon_2 \sigma_2 h_2}{0.91 M_p f(a)}} \quad (1.1)$$

$$f(a) = \frac{M_p}{[M_p + (\rho_1 h_1 + \rho_2 h_2) \pi a^2] \pi a^2} \quad \text{and} \quad a = a_p + 2h_1 \quad (1.2)$$

where

V_p : predicted ballistic velocity,

ε_2 : breaking strain of the backing plate,

σ_2 : ultimate tensile strength of backing plate (UTS),

ρ_2 : density of the backing plate,

h_2 : thickness of the backing plate,

ρ_1 : density of the front plate,

h_1 : thickness of the front plate,

M_p : mass of the projectile,

a_p : radius of the projectile.

Nevertheless, the complexity of many impact problems often makes it very difficult or sometimes impossible to use closed-form analytical solutions. Numerical models, based on solving all the governing equations over a spatial grid at successive time increments, have proven to be valuable design tools since they can help achieve a comprehensive understanding of the ballistic impact process. A number of numerical models simulating the ballistic impact process on two-component ceramic–metal and ceramic–composite armors have been published since the early 90s [10].

Although simulation of ballistic impact event is a complicated job due to complex material parameters and the need for the definition of advanced strength and failure models for the interaction between the projectile and the armor materials, once these aspects are well defined various different impact problems (different armor thickness, different impact velocity of the projectile etc.) can be solved without further effort.

1.2 Impact Event

Impact may be defined as the relatively sudden application of impulsive force, to a limited volume of material or part of a structure. Results of an impact can be largely elastic, with some energy dissipated as heat, sound, internally in the material etc. Alternatively there may be deformation, permanent damage, entry of the projectile into the target (penetration) or passing through of the projectile through the target (perforation) [11]. Figure 1.2 summarizes the various failure mechanisms of armors.

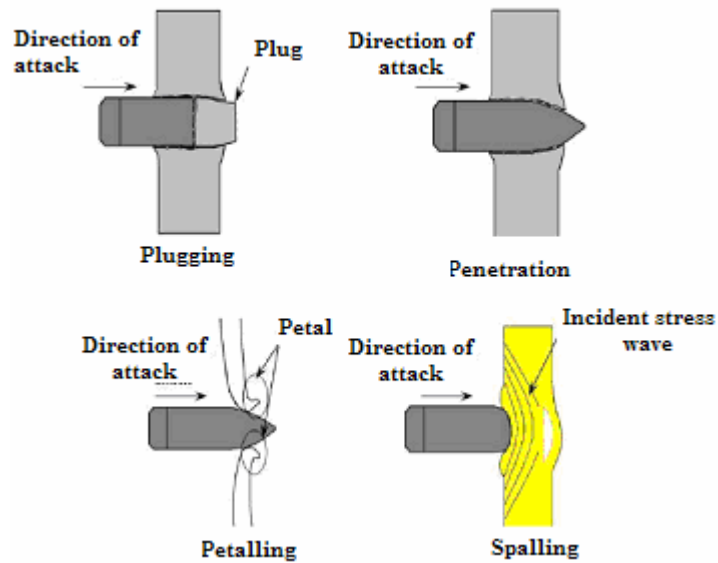


Figure 1.2 Mechanisms of penetration of armor [12].

Spalling, tensile failure as a result of the reflection of the initial compressive wave from the rear surface of a finite-thickness plate, is a commonplace mechanism under explosive and intense impact loads, especially for materials that are stronger in compression than they are in tension (e.g. ceramics) [12].

Impact by a blunt or hemispherical-nosed striker at a velocity close to the ballistic limit (the minimum velocity required for perforation) of a finite-thickness target results in the formation of a nearly cylindrical slug of approximately the same diameter as the projectile which is termed as the *plugging failure* [12].

Petalling is produced by high radial and circumferential tensile stresses after the passage of the initial stress wave. The intense-stress fields occur near the tip of the projectile. Bending moments created by the forward motion of the plate material pushed by the striker cause the characteristic deformation pattern. It is most frequently observed in thin plates struck by conical bullets at relatively low-impact velocities or by blunt projectiles near the ballistic limit [12].

1.3 Literature Survey

1.3.1 Mechanics

There are various mechanisms that contribute to the penetration/perforation of armor plates. When different types of armor plates are used together, i.e. ceramic tiles backed by composite plates, the mechanisms get more complex. Therefore the history of the analysis of impact on armor plates starts with the studies on the mechanics of penetration and perforation.

Cristescu et al. [13] analyzed the failure mechanisms of glass/epoxy 0/90 composite targets perforation by 1 cm-diameter cylindrical steel projectiles. This study suggested that the typical failure mechanism was indentation of the projectile in the first lamina, which caused fiber stretching while cutting-out the lamina. The stretching resulted in strain-induced delamination that progressed over the fiber stretch area. The process developed lamina-by-lamina. The more layers within a lamina, the stronger its resistance to plugging and the larger the corresponding delamination area.

Mechanics of penetration and perforation is analyzed in detailed by Wilkins [14]. Wilkins offers two types of material failure that are involved in the impact problems. One of them is when the elastic limit is exceeded and the plastic flow occurs. The other one is when the cohesive strength of the material is exceeded and fracture occurs. He also explained the stress wave phenomenon when a projectile strikes a target; first wave into the target is a compression wave followed by a release wave. An additional release wave is generated when the compression wave reaches the free boundary of the target opposite the impact. The interaction of the two release waves can cause very high tensile stresses to develop in the target. Finally tensile failure what is called as spall which is the first failure mode can occur in the target.

Wilkins gave some important parameters of target plates to resist penetration as bulk and shear moduli, strength, density, and thickness.

He stated that one of the most important parameters for a target to defeat a pointed projectile is to break off the point as early as possible. The target property that could satisfy this is a large resistance to deformation. The material properties responsible for resisting deformation are high moduli and high shear strength. The shear strength is a volume effect and to utilize this property the thickness of the target must be sufficiently large compared to the projectile dimensions.

Wilkins [14] also mentioned the composite armors which are comprised of two or more armor plates. He explained the required armor properties to defeat a projectile as being thick plates, high bulk and shear moduli, high yield stress to maintain the resistance to deformation at high stress levels, and resistance to fracture when large tensile stresses (spall) occur. Nevertheless it is not possible to find one material that maximizes all of these properties when the total areal density of the target must be minimized. He suggests using ceramic plates backed by some other material which is resistant to tensile stresses in contrast to ceramics. In his analysis, he pointed to the formation of fracture conoid in the ceramic material at the impact surface and spread of the conoid to the interface between the ceramic and the backup plate. Figure 1.3 represents the formation of the fracture conoid in the ceramic target.

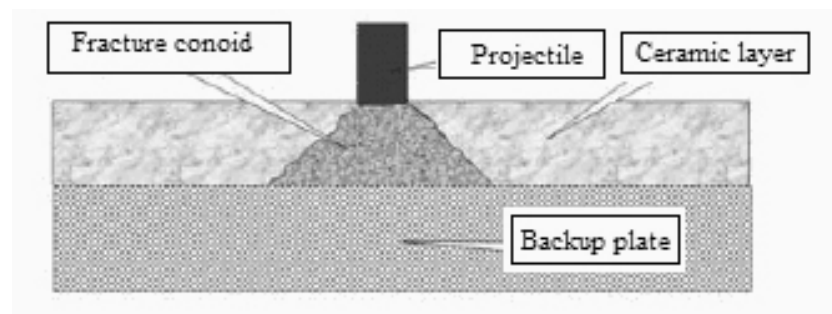


Figure 1.3 Fracture conoid formation [15].

Finally Wilkins [14] emphasized the conoid formation event. He explained the effect of the conoid as being to limit the amount of ceramic that participates in transmitting the load to the backup plate. In his analysis he found the highest stress level on the backup plate occurred at the center of impact where greatest compression occurs.

Sierakowski and Takeda [16] studied in-plane failure mechanisms of glass/epoxy composite systems due to impact by 9.5 mm, blunt and hemi-spherically-nosed steel projectiles. Hemispherical nose impactors generated localized delamination, at the same time generating a single crack. For the blunt nosed projectiles a generator strip (a piece of lamina delaminated from the target along the fiber direction) of width $2D$ (D is projectile's diameter) ran along the fibers at the rear (distal) side of the target.

Sun and Wang [17] performed pendulum ball impact tests on graphite/epoxy laminated samples. Matrix cracking and delamination were prevailing damage modes for low velocity impact, and fiber breakage is observed at projectile velocity of about 10-100m/s. The material response of a composite target to ballistic impact is characterized by a shorter time of applied load (the projectile-target interaction time), when compared with the low velocity impact load time. Hence the studies on the damage of composite materials under ballistic impact are focused on the localized damages (damage concentration).

Ruiz and Duffin [18] studied the localized damage of reinforced carbon/epoxy laminates impacted by 10g impactor launched with a velocity up to 600 m/s at an angle of 40° . The following failure modes on plates impacted by projectiles were observed:

- Total destruction at an impact velocity of 280 m/s,
- Extensive cracking and delamination at an impact velocity of 240 m/s,
- Small damage at an impact velocity of 200 m/s.

They observed relatively large area of plastic deformation at sub critical velocities of impact. An increase in the impact velocity resulted in stronger localization of the damage area around the impact point.

Bruchey and Horwath [19] expressed the importance of utilizing the backing and the surrounding plates to the ceramic facing layer. They explained the function of the ceramic material in the armor system as being the breaking up of the Armor Piercing (AP) threat while terminating of fragment energy in the backing material. It was postulated that the performance of these “composite” armor systems was influenced by the ability of the ceramic to shatter and destroy some portion of the AP threat on the tile surface -interface defeat of the AP projectile or dwell- by forcing the projectile flow radially outward without penetrating significantly, with some harder ceramics being considerably more effective armor components.

Gellert et al. [20] analyzed the ballistic impact of conical and flat projectiles against glass-fiber plastics. The test results reveal that the dependence of impact energy at the ballistic limit velocity (this critical energy can be reduced to the perforation energy) is a bilinear function of the target thickness. The fracture analysis showed that indentation and dishing (disc shape removal of the target material which is larger in diameter than the projectile) are two main deformation mechanisms, which are responsible for perforation. The indentation and dishing energies are linear functions of the target thickness, so the perforation energy, which is just a sum of those, is a bilinear function. The dishing effect is observed mainly at small thicknesses of the targets and a combination of indentation that is associated with the fiber breakage and dishing is observed for thick targets.

Fink and Kaufmann et al. [21, 22] emphasized the roles of ceramic tiles and fiber composite backing plates as follows: ceramics destroy the tip of the projectile and distribute the impact load over a large area of the composite, and decelerate the projectile. The composite layer, however, supports the ceramic tiles and acts as a barrier against the ceramic fragments and while further resisting the projectile.

Dechaene et al. [23] identified important mechanisms of fiber composite materials under low velocity impact. Initially, the damage starts with matrix cracking on the back of a laminate, where tensile stresses are dominant. The matrix-cracking gradually develops radially over a larger area and in the through-the-thickness direction, starting from the point at the back of a laminate, which is opposite to the projectile-target contact point, but the damage does not usually reach projectile-target contact point, where the compression stress state is established. Delamination develops concurrently with matrix damage and the extent of this damage in laminated structural material depends on the interfacial strength between laminas. Finally, fiber breakage occurs, when the tensile stress achieves extreme magnitude in the fibers.

In the paper by Fujii et al. [24] Carbon Fiber Reinforced Plastic (CFRP) samples with different fiber strength are analyzed. Study has shown that impact delamination for laminates with stronger fibers and larger failure strain is larger and deeper. This study has also revealed that within the range of high velocities (from 500 up to 1230 m/s), fracture occurs in a fluid manner for 2 mm-samples. For 6 mm-samples, the front layers were damaged as the 2 mm-samples did, however, the rear layers were damaged in an extrusive manner with delamination and plugging mechanism. Plugging develops as a result of a nearly cylindrical slug of approximately the same diameter as the projectile being set in motion by the projectile. Failure occurs due to large shears produced around the moving slug. The delamination width increased with impact energy for thick laminates but remained constant for thin laminates. The failure mechanism for thin targets in this velocity range is fluid-like and the fracture is smaller.

Hammond et al. [25] studied impact of 12.7 mm steel projectiles onto the carbon-fiber composites. Observations revealed that the target damage was in the vicinity of the projectile diameter at the moment of the projectile's entrance into the target. After the target was fully exited, cracking occurred in the outer ply both in the fiber direction and orthogonally to the fiber direction resulting in the ply's delamination.

1.3.2 Analytical Models

Analytical models that turn the impact problem into a mathematical model generally give insight about some parameters/properties of the armors. The basic form of the analytical model was proposed by Florence [8] the details of which were given previously.

Hetherington [26] study aimed at seeking the ratio of front plate thickness ratio to back plate thickness which will provide a specified level of protection at minimum weight by using the Florence model [8]. He kept the armor material properties ($\epsilon_2, \sigma_2, \rho_1, \rho_2$), areal density of the armor system ($\rho_1 h_1 + \rho_2 h_2$) and the threat parameters (M_p, a_p) while changing the ratio of ceramic to backing plate thickness (h_1 / h_2). At the end of his work, an insight is obtained into the factors governing the optimum value of (h_1 / h_2) by seeking an optimum to the Florence equation analytically:

$$\frac{h_1}{h_2} \approx 4 \frac{\rho_2}{\rho_1} \quad (1.3)$$

Equation (1.3) reveals that the ratio of ceramic to backing plate thickness is determined principally by the density of the materials employed. Hetherington suggested that optimum h_1 / h_2 for alumina/aluminum combination is in the region of 2.9, that for alumina/Glass Fiber Reinforced Plastic (GFRP) is about 2.5, and that for alumina/Kevlar is about 1.6.

Wang and Lu [27] studied the same problem. They kept the total thickness of the armor plates constant rather than areal density and sought a solution to find the ratio of the front plate thickness to that of backing plate.

Benloulo and Gálvez [28] developed a very simple one-dimensional and fully analytical model of ballistic impact against ceramic/composite armors. The model

made it possible to calculate the residual velocity, residual mass, the projectile velocity and the deflection or the strain histories of the backup material. The authors also checked the validity of the analytical model both with ballistic tests and numerical simulations giving good predictions in good agreement with them.

Ben-Dor et al. [29] investigated the problem considered in Hetherington's [26] study for an arbitrary two-component armor. The aim of this study was to find the thickness of the plates that provide the maximum ballistic limit velocity for a given areal density of the armor. It was shown that the thickness of the plates can be changed in a quite broad range in the neighborhood of the optimal design of the armor without decline in its defense properties.

1.3.3 Numerical Studies

As stated previously, analyzing the ballistic event with numerical models gives detailed information about the impact problem in various aspects. However, it is a valuable tool as long as the solution (or findings) is confirmed with tests or some agreed behaviors of the involving materials.

Nandlall et al. [30] studied on the ballistic response of glass-fiber-reinforced plastic (GFRP) laminates by numerical simulations. A new constitutive model is implemented into the finite element code LS-DYNA2D. The ballistic limit velocities obtained numerically compare well with experimental ballistic limit data. The model enables the strain softening feature and thus providing the ability to simulate energy absorption due to fracture. The ability to display the level of damage in a spatially continuous fashion is an attractive feature of the model developed in this study.

Mahfuz et al. [31] analyzed the high velocity-impact on Al_2O_3 ceramic backed by S2-glass fiber composites by fragment simulating projectiles (FSP). The numerical study was performed using the LS-DYNA3D, which is an explicit finite element code dedicated to analyze dynamic problem associated with large

deformation, low and high velocity impact, ballistic penetration and wave propagation. The main objective of the finite element analysis was to investigate the response of the armor in the event of a projectile striking at a velocity close to V_{50} ballistic limit velocity which is defined as the velocity at which the probability of perforation of an armor material is 50 percent. The energy histories of the projectile, target and the total system were analyzed.

In the paper by Jovicic and Zavaliangos [32], the finite element (FE) analysis was performed to simulate the structural behavior of composite armors, and assess the effect of materials selection and fiber architecture. Baseline performance of the model was evaluated by the 2D simulation of the impact on a ceramic plate. Residual velocity and back-plane displacement time history were evaluated as a function of different impact site and the projectile incident angle. The effect of the ceramic facing size on the projectile residual velocity and displacement of the backing plate was investigated, and it was found that projectile impact between two spheres, and smaller facing size compared to projectile size, lower residual velocity and back-plane displacement.

Lamina failure model for fabric composites was extended to model progressive post failure by Yen [33]. Continuum damage mechanics (CDM) model which characterizes the growth of damage by decreasing the material stiffness was used in this respect. Simulations of the ballistic impact of S2-Glass/Epoxy composite panels were conducted by taking account for the strain-rate sensitivity properties by using LS-DYNA. The implemented model was successfully utilized to predict the ballistic limit composite laminates subjected to high velocity ballistic impact conditions.

Numerical simulation of impact, for both low and moderately high speed, of 5mm radius steel sphere on composite laminate plates reinforced with Kevlar 29 was studied by Silva et al. [5]. All the simulations presented in the paper were carried out by using the hydrocode AUTODYN, which is specially designed for non-linear, transient, dynamic events. Deflection history of the head of the striker,

maximum impact load obtained from the numerical simulation were in good agreement with those obtained from the experimental results. Another numerical study of ballistic impact of a simulated fragment on Kevlar fiber reinforced panel was held in order to determine the V_{50} and the global damage. The simulation result for predicting the V_{50} was in an good correlation with the test result. Very similar trends were also observed for the global damage and delamination patterns.

A combined numerical and experimental study for the analysis of Ceramic/Kevlar 29 composite armor system against 4.0g NATO 5.56 mm calibre bullet has been performed [34]. The simulations were performed using hydrocode AUTODYN, and all simulations were done by changing the thickness of the ceramic tiles while keeping the areal density of the armor system constant. It was shown that the results obtained from the present simulation match fairly well with the theoretical ones obtained by the Florence model.

Another study was held by Mahdi and Gillespie [35]. In this study, the mechanism of load transfer and deformation of alumina (Al_2O_3) ceramic layer backed by fiber composite subjected to bending loads were investigated. The numerical simulations were performed using both 2D and 3D models. The results from the 2D model were shown to compare well with that of the 3D model.

In the study of Fawaz et al. [36], several sets of 3-D finite element models were developed to investigate the response of a ceramic-composite integral armor system to normal and oblique penetrating projectiles (7.62 AP round). Comparison of the energy histories as well as stress and force distributions of armors subjected to normal and oblique impacts have been conducted by using the finite element code LS DYNA3D. Developed models were able to simulate projectile erosion, ceramic conoid formation, as well as the failure of ceramic and composite plates. The interlaminar stresses at the ceramic-composite interface and the forces at the projectile-ceramic interface for oblique impact were found to be smaller than those for normal impact. Furthermore, it was found that when a

projectile impacts obliquely on the armor, it changes its angle during the perforation, forming an elliptical cavity at the tip of projectile. Finally, it was observed that the projectile erosion in oblique impact is slightly greater than that in normal impact. It was also shown that the preliminary computations demonstrated reasonable correlation with existing experimental data.

A three-dimensional model to provide a reasonable predictions of the deformation response of polymer matrix composites including strain rate effects developed in the study of Ala et al. [37]. This model is implemented into the explicit dynamic finite element code LS-DYNA. Simulations included the behavior of composite structures under various loads such as impact and tensile loading. Examples of composite materials under crash and tensile loading are used to validate the model. The predicted results compared well to experimentally obtained stress–strain curves.

The ballistic performance of low weight Al_2O_3 Ceramic-Glass Fiber Reinforced Plastic (GFRP) laminated armor system against 7.62 mm AP rounds is investigated by using AUTODYN hydrocode by Aydinel, Ögel and Yıldırım [38]. In this analysis the thickness of the ceramic plate kept at a constant value of 8mm while the thickness of the GFRP was changed between 1 to 20 mm and the residual velocity of the projectile was analyzed. The results of the numerical simulations were compared with those of the experimental work and Florence's analytical studies.

Grujicic et al. [39] carried out a detailed computational analysis of the ballistic performance of composite and hybrid armor panels hard-faced with Al_2O_3 ceramic tiles by using AUTODYN software. The initial simulations were performed to validate the composite material model. In these simulations, there was an agreement between the V_{50} values obtained from the numerical simulations and those from the experimental results. Next, the simulations were done by considering the whole armor system, i.e. composite panels hard-faced

with alumina ceramic tiles. Again the overall agreement between the experimental and computational results is quite good.

1.4 Scope of the Study

In this thesis, the numerical analysis of the advanced composite armor system impacted by an AP bullet will be performed. The composite armor is composed of two main layers which include two different materials. In the front layer, there is silicon carbide (SiC) ceramic. KevlarTM fiber reinforced plastic (KFRP) will be used as the backing plate for the ceramic, which is highly brittle. The projectile to be used in the numerical simulations will be of 7.62 mm. In all of the simulations the ceramic plate thickness is held constant, while different KFRP plate thicknesses are used to propose an optimum thickness values for these materials in armor applications. After getting the simulation results, areal densities of different configurations of the armor system will be compared. At the end, weight saving in the armor system will be discussed when the armor configuration has the optimum ceramic/composite ratio. Details of these studies will be explained in the following chapters

CHAPTER 2

PROBLEM DEFINITION

2.1. Introduction

The response of materials and structures to intense impulsive loading is quite complex. The behavior of impacted solids may be divided into three regimes. First one is for loading conditions that result in stresses below the yield point, materials behave elastically and for metals Hooke' s law is applicable. The second regime includes the events when the intensity of the applied loading is increased and the material is driven into the plastic range. The behavior here involves large deformations, heat generation, and often material failure of the colliding solids through a variety of mechanisms. The third and the last behavior may be the following one: Loading intensity further increases, pressures are generated that exceed the strength of the colliding solids by several orders of magnitude, and as a consequence the material behaves hydrodynamically.

For low intensity excitations, both the geometry of the entire structure as well as the nature of the material from which it is made play a major role in resisting external forces. As loading intensity increases, the response tends to become highly localized and is more affected by the constitution of the material in the vicinity of load application than the geometry of the total structure [40].

2.2 Impact Theory

Impact processes are encountered when bodies are subjected to rapid impulsive loading, whose duration of application is short compared to the time for the body to respond inertially. The inertial responses are stress pulses propagating through

the body to communicate the presence of loads to interior points. In our everyday experience, such loadings are the result of ballistic impact or explosion [41].

In the evolution of impact theory, four major aspects emerged as distinct subjects of interest. These four aspects are:

- *Classical mechanics*
- *Elastic stress wave propagation*
- *Contact mechanics*
- *Plastic deformation*

The impulse-momentum approach can address the relationship between the velocities before and after impact, given the knowledge of the coefficient of restitution. Nevertheless, it is incapable of calculating the force at the impact point. The wave propagation theory is necessary to predict stresses inside the solid. The contact mechanics approach offers the possibility of treating the contact region as a spring damper system, making it possible to treat the impact as a continuous-time dynamic phenomenon. The large plastic strain theory is most useful in the domain of perforation by projectiles, as in ballistics. [41]

Classical mechanics: This involves the application of the fundamental laws of mechanics to predict the velocities after impact. The impulse-momentum law forms the core of this approach. The algebraic nature of this method makes the mathematical development easy and accessible to most engineers. The loss of energy in any real impact process is taken into account by means of the coefficient of restitution. The accuracy of this coefficient is crucial to obtaining sufficiently good results. Unfortunately, this approach is unable to predict the contact force between bodies or the stresses in them.

Two limit cases are considered in the elementary theory of impact: a perfectly elastic impact, and a perfectly inelastic impact. The former case implies that the kinetic energy of the system is conserved. The latter case assumes that the two

bodies coalesce, to move as a single mass, after impact. The velocity of the combined mass can then be predicted using only the conservation of momentum. However, most impacts are neither fully elastic nor fully inelastic. This partial loss of the initial kinetic energy is expressed in terms of the restitution coefficient, e , first introduced by Newton. This coefficient relates the relative velocities before and after impact according to the equation:

$$V_{1f} - V_{2f} = -e(V_{1i} - V_{2i}) \quad (2.1)$$

where

V_{1f} : final velocity of the colliding body 1,

V_{2f} : final velocity of the colliding body 2,

V_{1i} : initial velocity of the colliding body 1,

V_{2i} : initial velocity of the colliding body 2,

e : coefficient of restitution.

The quantity e is a dimensionless coefficient between 0 and 1 where 0 corresponds to a totally inelastic impact and 1 to a perfectly elastic impact. The restitution coefficient is a global measure of the energy loss during impact and may incorporate different forms of dissipation such as viscoelastic work performed on the materials of the impacting bodies, plastic deformation of contact surfaces and vibration in the two bodies. The restitution coefficient is not an internal material property. It depends on the materials of the bodies, their surface geometry and the relative impact velocity.

Elastic wave propagation: Impact is accompanied by a stress wave that propagates in the impacting bodies away from the region of impact. If the energy transformed into vibrations becomes an important fraction of the total energy, then the classical approach becomes insufficient to examine an impact problem.

The system of equations governing the motion of a homogeneous, isotropic, linearly elastic body consists of the stress equation of motion, Hooke's law, and the strain-displacement relations is given by Achenbach [42]:

$$\sigma_{ij,j} + \rho f_i = \rho \ddot{u}_i \quad (2.2)$$

$$\sigma_{ij} = \lambda \varepsilon_{kk} \delta_{ij} + 2\mu \varepsilon_{ij} \quad (2.3)$$

$$\varepsilon_{ij} = \frac{1}{2}(u_{i,j} + u_{j,i}) \quad (2.4)$$

where

λ and μ : Lamé constants,

σ_{ij} : components of the stress tensor,

ε_{ij} : components of the strain tensor,

u_i : components of the displacement vector,

ρ : density,

f_i : body forces,

δ_{ij} : Kronecker's delta where $\delta_{ij} = \begin{cases} 1, \dots i = j \\ 0, \dots i \neq j \end{cases}$.

In the above equations, the indicial notation is utilized such that the repeated subscripts denote summation. The comma denotes partial differentiation with respect to coordinates whereas the dot indicates a time derivative.

Equations (2.2) – (2.4) may be combined to yield equations of motion:

$$\mu u_{i,jj} + (\lambda + \mu) u_{j,ji} + \rho f_i = \rho \ddot{u}_i \quad (2.5)$$

Equations (2.2) – (2.5) must be satisfied at every interior point of the undeformed body. With the specification of boundary conditions on the surface of the body as

well as initial conditions, the statement of the elastodynamic problem is complete.

In Equation (2.5), body forces can be neglected when compared to other applied loads, which reduces (2.5) to

$$\mu u_{i,jj} + (\lambda + \mu)\Delta_{,i} = \rho \ddot{u}_i \quad (\text{by letting } \Delta = u_{j,j}) \quad (2.6)$$

Differentiating (2.6) with respect to the spatial variables in respective order gives

$$\mu u_{i,jji} + (\lambda + \mu)\Delta_{,ii} = \rho \ddot{u}_{i,i} \quad \text{or} \quad \frac{\rho \partial^2 \Delta}{\partial t^2} = (\lambda + 2\mu) \frac{\partial^2 \Delta}{\partial x_i \partial x_i} \quad (2.7)$$

Since λ , μ , and ρ are constants, (2.7) takes the form of classical wave equation as

$$\frac{\partial^2 \Psi}{\partial t^2} = c^2 \frac{\partial^2 \Psi}{\partial x_i \partial x_i} \quad (2.8)$$

where $\Psi(x, t)$ is the dependent variable and is a measure of some property of the disturbance such as displacement or velocity and c is the wave speed.

Contact mechanics: The contact stresses resulting from the impact of two bodies are another area of interest in the study of impact. Conventional contact mechanics is mainly concerned with static contact although it has been extended to approximate solutions when impact is involved. For spheroidal surfaces, Hertz theory is used to obtain the force-deformation relation needed to calculate the duration of impact and the maximum indentation. This approach has been extended to the cases where contained plastic deformation occurs, generally with the assumption of a material having a yield point. Numerical models of the contact zone are also used when Hertz theory is not applicable. The force-deformation equation is often augmented with a damping term to reflect

dissipation in the contact area, thus allowing one to effectively model the contact area as a spring-damper system.

For conventional materials, Hertz theory predicts the stress distribution in the contact zone between two bodies having a surface of revolution. It also allows one to calculate the normal and shear stress distribution inside the solid. This reveals some interesting and important facts. For example, the maximum shear stress, which is directly related to the material failure, occurs below the contact surface, potentially causing undetected plastic yielding. A very commonly used result is the force-indentation relation for the sphere-to-sphere contact

$$F = K\delta^{3/2} \quad (2.9)$$

where

F : normal force pressing the solids together,

δ : total of deformation of surfaces in contact,

K : constant depending on the sphere radii and elastic properties of the sphere materials.

This equation was combined with the equations of motion by Timoshenko [43] to treat the impact of two spheres. The maximum indentation and the impact duration were calculated. A similar treatment is also found in Goldsmith [44] and Johnson [45]. This analysis constitutes what is known as *Hertz theory of impact*. Equation (2.9) above is also valid for any 3D contact of solids.

Plastic deformation: When plastic strains go beyond the scale of contained deformation, the elastic wave propagation model can no longer be applied to analyze impact problems. This is the domain of high velocity impact generally associated with explosives and projectiles. Goldsmith [44] presented an extended study of the subject using two approaches: the hydrodynamic theory of the behavior of solid bodies and the theory of plastic wave propagation.

In the hydrodynamic theory, the stress tensor may be separated into a uniform hydrostatic pressure (all three normal stresses equal) and a stress deviatoric tensor associated with the resistance of the material to shear distortion and the permanent deformation is considered to be a result of a change in the body's density. An *equation of state*, which is defined as the relationship between the hydrostatic pressure, the local density (or specific volume) and the local specific energy (or temperature), is used together with the laws of conservation of momentum, energy and mass.

The first convincing one dimensional, finite amplitude plastic wave propagation theory was developed independently by Karman [46], Taylor [47], and Rakhmatulin [48]. This theory assumed that the behavior of a material could be described by a single-valued relation between stress and strain in uniaxial stress and that stress-strain curve was concave toward the stress-axis. The theory further implied that the stress-strain relation was the one obtained in a conventional quasistatic tensile test. The theory was totally uniaxial in nature, neglecting any three-dimensional effects such as those that might arise because of lateral inertia. Only axial stresses were considered. Consider an element of rod of original length dx as shown in Figure 2.1. The unbalanced force in the x-direction is

$$dF = A \frac{\partial \sigma}{\partial x} dx \quad (2.10)$$

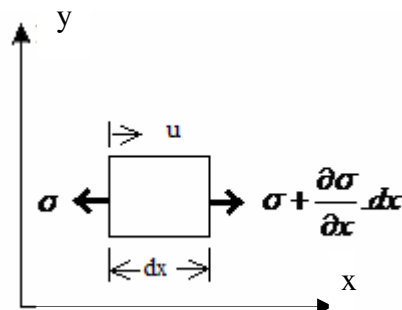


Figure 2.1 Nomenclature for a rod element

and it acts on the element whose mass is $\rho A dx$, where ρ and A are the mass density and the cross-sectional area of the element respectively, and σ is the axial engineering stress. It is assumed that the material behavior can be described by a single-valued relation of the form

$$\sigma = \sigma(\varepsilon) \quad (2.11)$$

where ε is the engineering strain and it can be related to displacements in the x-direction, u

$$\varepsilon = \frac{\partial u}{\partial x} \quad (2.12)$$

$$v = \frac{\partial u}{\partial t} \quad (2.13)$$

where v is the particle velocity. The equation of motion for longitudinal stress in a bar or rod is then

$$\rho \frac{\partial^2 u}{\partial t^2} = \frac{\partial \sigma}{\partial \varepsilon} \frac{\partial \varepsilon}{\partial x} \quad (2.14)$$

Substituting Equation (2.12) into the Equation (2.14) yields the wave equation as

$$\frac{\partial^2 u}{\partial t^2} - c^2(\varepsilon) \frac{\partial^2 u}{\partial x^2} = 0 \quad (2.15)$$

where

$$c^2(\varepsilon) = \frac{1}{\rho} \frac{d\sigma}{d\varepsilon} \quad (2.16)$$

Three solutions to Equation (2.14) could be found and pieced together to give the total solution by Karman and Duwez [49] with the following boundary conditions

$$u = v_1 \text{ at } x=0 \text{ and } u = 0 \text{ at } x \rightarrow -\infty \quad (2.17a)$$

$$\text{for } |x| < c_1 t, \varepsilon = \text{cons.} = \frac{v_1}{c_1} = \varepsilon_1 \quad (2.17b)$$

$$\text{for } c_1 t < |x| < c_0 t, E(\varepsilon) = \frac{x^2}{t^2} \quad (2.17c)$$

$$\text{for } |x| > c_0 t, \varepsilon = 0 \quad (2.17d)$$

The solution for strain as a function of $\xi = x/t$ is presented in Figure 2.2 which shows the two wave fronts traveling at different velocities.

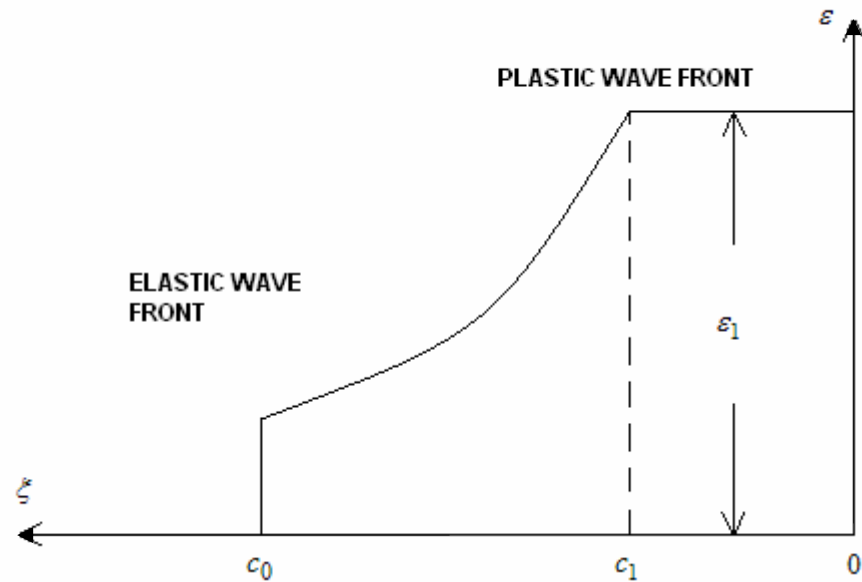


Figure 2.2 Strain distribution in a rod produced by constant velocity impact at end [7]

Nevertheless there were some aspects of wave theory that cannot be readily explained by the rate independent theory and Malvern [50, 51] also proposed a strain-rate dependent version of this theory.

2.3 Shock Waves in Solids

The conventional uniaxial stress-strain curve does not adequately represent the state of stress and strain to which a material is subjected under shock loading. Therefore, the quantities associated with such a curve (elastic modulus, yield strength, ultimate strength and elongation) are not by themselves appropriate to describe the relative behavior of materials [52].

The stresses and strains which occur for 1D deformation can be analyzed to understand how materials behave under shock loading. The principle strains in three principal directions can be separated into their elastic and plastic components as

$$\varepsilon_1 = \varepsilon_1^e + \varepsilon_1^p \quad (2.18a)$$

$$\varepsilon_2 = \varepsilon_2^e + \varepsilon_2^p \quad (2.18b)$$

$$\varepsilon_3 = \varepsilon_3^e + \varepsilon_3^p \quad (2.18c)$$

For 1-D deformation and due to the symmetry

$$\varepsilon_2 = \varepsilon_3 = 0 \quad \text{and} \quad \varepsilon_2^p = \varepsilon_3^p \quad (2.19)$$

and therefore

$$\varepsilon_2^p = -\varepsilon_2^e \quad \text{and} \quad \varepsilon_3^p = -\varepsilon_3^e \quad (2.20)$$

The plastic portion of the strain is taken to be incompressible, so that

$$\varepsilon_1^p + \varepsilon_2^p + \varepsilon_3^p = 0 \quad \text{or} \quad \varepsilon_1^p = -\varepsilon_2^p - \varepsilon_3^p = -2\varepsilon_2^p \quad (2.21)$$

By combining Equations (2.18), (2.19) and (2.21)

$$\varepsilon_1 = \varepsilon_1^e + 2.\varepsilon_2^e \quad (2.22)$$

The elastic strain in terms of the stresses and elastic constants is given by

$$\varepsilon_1^e = \frac{\sigma_1}{E} - \frac{\nu}{E}(\sigma_2 + \sigma_3) = \frac{\sigma_1}{E} - \frac{2\nu}{E}\sigma_2 \quad (\text{since } \sigma_2 = \sigma_3) \quad (2.23a)$$

$$\varepsilon_2^e = \frac{\sigma_2}{E} - \frac{\nu}{E}(\sigma_1 + \sigma_3) = \frac{1-\nu}{E}\sigma_2 - \frac{\nu}{E}\sigma_1 \quad (2.23b)$$

$$\varepsilon_3^e = \frac{\sigma_3}{E} - \frac{\nu}{E}(\sigma_1 + \sigma_2) = \frac{1-\nu}{E}\sigma_3 - \frac{\nu}{E}\sigma_1 \quad (2.23c)$$

Using Equation (2.22) together with Equations (2.23a) and (2.23b) gives

$$\varepsilon_1 = \frac{\sigma_1(1-2\nu)}{E} + \frac{2\sigma_2(1-2\nu)}{E} \quad (2.24)$$

The plasticity condition for von Mises condition for this case is

$$\sigma_1 - \sigma_2 = Y_0 \quad (2.25)$$

where Y_0 is the static yield strength.

Using Equation (2.25) for σ_2 gives

$$\sigma_1 = \frac{E}{3(1-2\nu)}\varepsilon_1 + \frac{2}{3}Y_0 \quad (2.26a)$$

or

$$\sigma_1 = K\varepsilon_1 + \frac{2}{3}Y_0 \quad (2.26b)$$

where $K = \frac{E}{3(1-2\nu)}$ is called the *bulk modulus* and is defined as the pressure increase needed to effect a given relative decrease in volume. Equation (2.26) is the stress-strain relation for uniaxial strain [52].

For the special case of elastic strain where all related plastic strain components of principle strains are all “0”, above equations are rearranged by Zukas [52] and yield

$$\varepsilon_1 = \frac{\sigma_1}{E} - 2\nu^2 \frac{\sigma_1}{E(1-\nu)} \quad \text{or} \quad \sigma_1 = \frac{(1-\nu)}{(1-2\nu)(1+\nu)} E \varepsilon_1 \quad (2.27)$$

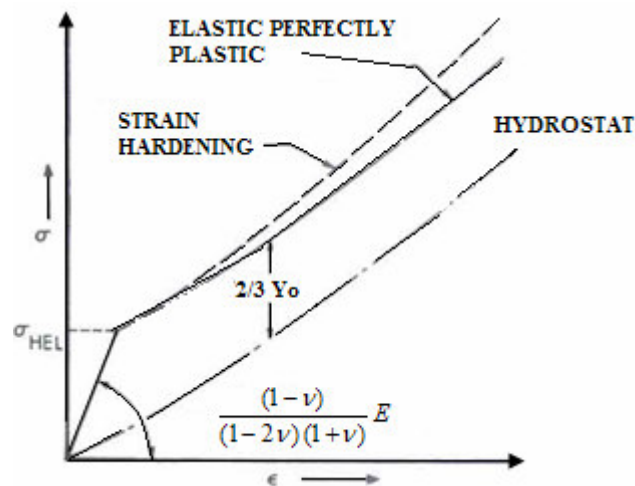


Figure 2.3 Details of uniaxial strain behavior [7].

Figure 2.3 shows representative stress-strain curves for uniaxial strain states, respectively. From this figure following remarks can be concluded [7]

- There is an increase in modulus for the uniaxial strain curve by a factor of $(1-\nu)/[(1-2\nu)(1+\nu)]$
- The yield point for uniaxial strain is referred to as the Hugoniot Elastic Limit (σ_{HEL})

- Uniaxial strain curve is also called as *Hugoniot curve*. There is a constant deviation from the Hugoniot curve of the stress σ_1 by $2Y_0 / 3$

Figure 2.4 shows the uniaxial stress-strain curve taken to much higher load levels. If the loading does not exceed the Hugoniot elastic limit, a single, elastic wave will propagate in the material.

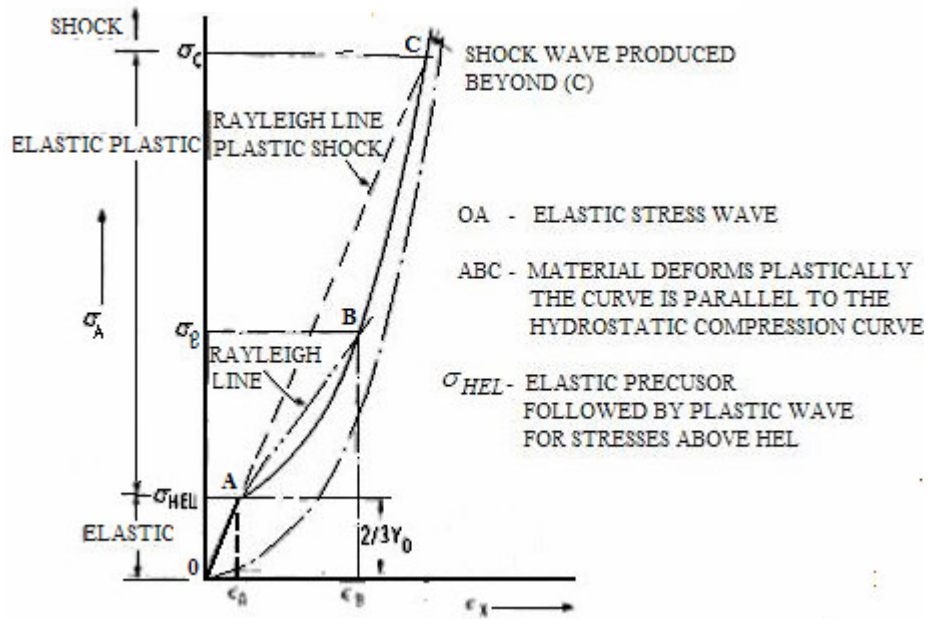


Figure 2.4 Regions of elastic, elasto-plastic and shock wave propagation [52].

If the magnitude of the applied stress pulse exceeds σ_{HEL} , two waves will propagate through the medium. The elastic wave will move with a speed

$$c_E^2 = \frac{E(1-\nu)}{\rho_0(1-2\nu)(1-\nu)} \quad (2.28)$$

This will be followed by a plastic wave moving with a speed that is a function of the slope of the stress-strain curve at a given value of strain and the plastic wave speed is given by

$$c_p^2 = \frac{1}{\rho_0} \frac{d\sigma}{d\varepsilon} \quad (2.29)$$

2.3.1 Conservation Equations Under Shock Loading

Let us consider a uniform pressure P_1 suddenly applied at one face of plate made of compressible material in Figure 2.5. The material is initially at a pressure P_0 . The pressure pulse propagates at a velocity U_S .

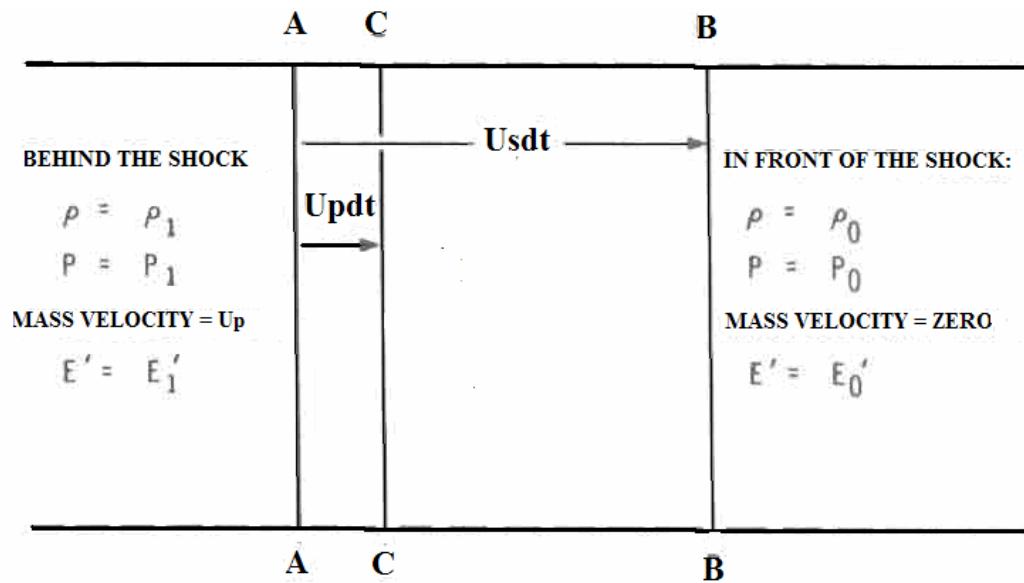


Figure 2.5 Progress of a plane shock wave [7].

The position of the shock front at some instant of time of time is indicated by the line AA. Some dt time later, the shock front advances to BB line while the matter initially at line AA moves to line CC. Across the shock front, mass, momentum and energy are conserved [7].

Conservation of mass across the shock front may be expressed by noting that the mass of material surrounded by the shock wave $\rho_0 U_s dt$ now occupies the volume $(U_s - u_p)dt$ at a density ρ_1

$$\rho_s U_s = \rho_1 (U_s - u_p) \quad (2.30)$$

Conservation of momentum is expressed by noting that the rate of change of momentum of a mass of material $\rho_0 U_s dt$ in time dt accelerated to a velocity u_p by a net force $P_1 - P_0$ is given by

$$P_1 - P_0 = \rho_0 U_s u_p \quad (2.31)$$

Conservation of energy across the shock front is obtained by equating the work done by the shock wave with the sum of the increase of both kinetic and internal energy of the system. Thus

$$P_1 u_p = \frac{1}{2} \rho_0 U_s u_p^2 + \rho_0 U_s (E_1 - E_0), \quad (2.32)$$

Eliminating U_s and u_p in Equation (2.32) resulting Rankie-Hugoniot relation as

$$E_1 - E_0 = \frac{1}{2} (V_0 - V_1) (P_1 - P_0) = \frac{1}{2} \left(\frac{1}{\rho_0} - \frac{1}{\rho_1} \right) (P_1 + P_0) \quad (2.33)$$

2.4 Mechanics of Composite Materials

Fundamental understanding of the composite material behavior under impact loading starts with the understanding of the mechanics of the composite materials. Composite materials have directional dependent mechanical properties

by their nature. Hence it is necessary to give special consideration when analyzing the mechanics of composite materials.

2.4.1 Definitions

A material is said to be *homogeneous* if the material properties remain unchanged throughout. In a *heterogeneous* system, however, the material properties are a function of position. Having defined these, next definitions would be the difference between the isotropy and the anisotropy. A material is *isotropic* if all its material properties at a point are independent of the direction and *anisotropic* if the material exhibits material properties that are directionally dependent, i.e., a given material property can have different values in different directions [53].

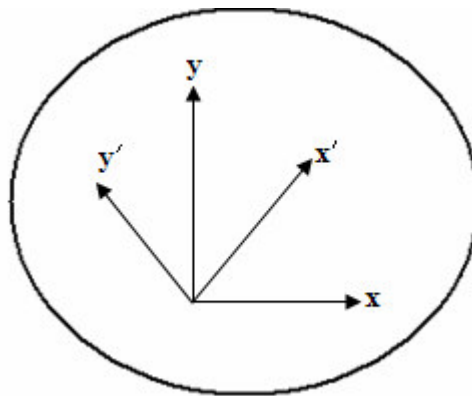


Figure 2.6 Definition of isotropic and anisotropic materials [53].

The generalized Hooke's law which is a linear relation between relation between six stresses and six strains can be expressed as,

$$\sigma_k = C_{kj} \epsilon_j \quad (k, j = 1, 2, \dots, 6) \quad (2.34)$$

where

σ_k : Stress tensor

ε_j : Strain tensor

C_{kj} : Elastic coefficients.

There are 36 C_{kj} terms in Equation (2.34) but they are not all independent of each other. Ochoa and Reddy [53] showed that $C_{kj} = C_{jk}$ and the number of independent elastic constants reduces to 21 from 36 for anisotropic materials. In matrix form Equation (2.34) can be expressed as,

$$\begin{pmatrix} \sigma_1 \\ \sigma_2 \\ \sigma_3 \\ \sigma_4 \\ \sigma_5 \\ \sigma_6 \end{pmatrix} = \begin{pmatrix} C_{11} & C_{12} & C_{13} & C_{14} & C_{15} & C_{16} \\ & C_{22} & C_{23} & C_{24} & C_{25} & C_{26} \\ & & C_{33} & C_{34} & C_{35} & C_{36} \\ & & & C_{44} & C_{45} & C_{46} \\ & & & & C_{55} & C_{56} \\ & \text{sym.} & & & & C_{66} \end{pmatrix} \begin{pmatrix} \varepsilon_1 \\ \varepsilon_2 \\ \varepsilon_3 \\ \varepsilon_4 \\ \varepsilon_5 \\ \varepsilon_6 \end{pmatrix}. \quad (2.35)$$

In Equation (2.35), single subscript notation for stress and strain components are given according to the following relations

$$\sigma_1 = \sigma_{11}, \sigma_2 = \sigma_{22}, \sigma_3 = \sigma_{33}, \sigma_4 = \sigma_{23}, \sigma_5 = \sigma_{13}, \sigma_6 = \sigma_{12} \quad (2.36)$$

$$\varepsilon_1 = \varepsilon_{11}, \varepsilon_2 = \varepsilon_{22}, \varepsilon_3 = \varepsilon_{33}, \varepsilon_4 = 2.\varepsilon_{23}, \varepsilon_5 = 2.\varepsilon_{13}, \varepsilon_6 = 2.\varepsilon_{12} \quad (2.37)$$

There occur some special cases for anisotropic materials in that they may have material symmetry and their behavior can be explained with less independent elastic constants. This situation is described by Ochoa and Reddy [53] as follows

“When the elastic coefficients at a point have the same values for every pair of coordinate systems which are mirror images of each other in a certain plane, that plane is called a plane of elastic symmetry for the material at that point.”

If a material has three orthogonal planes of elastic symmetry, which reduces the number of elastic constants to 9, then that material is said to be *orthotropic*. The stress-strain relation for the orthotropic materials in matrix form is given by Ochoa and Reddy [53] as

$$\begin{pmatrix} \sigma_1 \\ \sigma_2 \\ \sigma_3 \\ \sigma_4 \\ \sigma_5 \\ \sigma_6 \end{pmatrix} = \begin{pmatrix} C_{11} & C_{12} & C_{13} & 0 & 0 & 0 \\ & C_{22} & C_{23} & 0 & 0 & 0 \\ & & C_{33} & 0 & 0 & 0 \\ & & & C_{44} & 0 & 0 \\ & & & & C_{55} & 0 \\ & \text{sym.} & & & & C_{66} \end{pmatrix} \begin{pmatrix} \epsilon_1 \\ \epsilon_2 \\ \epsilon_3 \\ \epsilon_4 \\ \epsilon_5 \\ \epsilon_6 \end{pmatrix} \quad (2.38)$$

Elastic constants for an orthotropic material is expressed in terms of engineering constants by Reddy [54]

$$C_{11} = \frac{1 - \nu_{23} \nu_{32}}{\Delta E_2 E_3}, \quad C_{12} = \frac{\nu_{21} + \nu_{31} \nu_{23}}{\Delta E_2 E_3} = \frac{\nu_{12} + \nu_{32} \nu_{13}}{\Delta E_1 E_2} \quad (2.39a)$$

$$C_{13} = \frac{\nu_{31} + \nu_{21} \nu_{32}}{\Delta E_2 E_3} = \frac{\nu_{13} + \nu_{12} \nu_{23}}{\Delta E_1 E_2}, \quad C_{22} = \frac{1 - \nu_{13} \nu_{31}}{\Delta E_1 E_3} \quad (2.39b)$$

$$C_{23} = \frac{\nu_{32} + \nu_{12} \nu_{31}}{\Delta E_1 E_3} = \frac{\nu_{23} + \nu_{21} \nu_{13}}{\Delta E_1 E_2}, \quad C_{33} = \frac{1 - \nu_{12} \nu_{21}}{\Delta E_1 E_2} \quad (2.39c)$$

$$C_{44} = G_{23}, \quad C_{55} = G_{13}, \quad C_{66} = G_{12} \quad (2.39d)$$

$$\Delta = \frac{1 - \nu_{12} \nu_{21} - \nu_{23} \nu_{32} - \nu_{31} \nu_{13} - 2\nu_{21} \nu_{32} \nu_{13}}{E_1 E_2 E_3} \quad (2.40)$$

The inverse of the $[C]$ matrix is called the *compliance matrix* $[S]$ where

$$[S] = \begin{pmatrix} \frac{1}{E_{11}} & -\frac{\nu_{12}}{E_{11}} & -\frac{\nu_{31}}{E_{33}} & 0 & 0 & 0 \\ & \frac{1}{E_{22}} & -\frac{\nu_{23}}{E_{22}} & 0 & 0 & 0 \\ & & \frac{1}{E_{33}} & 0 & 0 & 0 \\ & & & \frac{1}{2G_{12}} & 0 & 0 \\ & & & & \frac{1}{2G_{23}} & 0 \\ & sym. & & & & \frac{1}{2G_{31}} \end{pmatrix} \quad (2.41)$$

and Equation (2.38) can be written in as the strain-stress relation in the following form

$$\varepsilon_k = S_{kj} \sigma_j \quad (2.42)$$

The stress-strain relations represent a mathematical formulation that describes the behavior of a mathematical model of a physical problem. Hence, the elastic constants should have values that will not violate certain basic physical principles. For example, a tensile force is bound to produce an extension in the direction of the applied force, or a hydrostatic pressure cannot cause an expansion in the material. As a result, some constraints should be imposed on the elastic constants of an orthotropic material and these constraints are obtained by Lempriere [55]:

$$E_{11}, E_{22}, E_{33}, G_{12}, G_{23}, G_{31} > 0 \quad (2.43)$$

$$1 - \nu_{12} \cdot \nu_{21} - \nu_{31} \cdot \nu_{13} - \nu_{23} \cdot \nu_{32} - 2 \cdot \nu_{21} \cdot \nu_{32} \cdot \nu_{13} > 0 \quad (2.44)$$

$$\nu_{21} < \sqrt{\frac{E_{22}}{E_{11}}}, \nu_{32} < \sqrt{\frac{E_{33}}{E_{22}}}, \nu_{13} < \sqrt{\frac{E_{11}}{E_{33}}} \quad (2.45)$$

2.4.2 Impact Damage Modeling of Composites

In general, beam and plate models are commonly used as structural elements for evaluating composite damage due to impact. Nevertheless, in the analysis of damage development in composites, emphasis should be given to the following items [56]:

- Determination of the load-time history of the impact force
- Determination of the stress-time history of the target internal stresses
- Determining the failure modes in the target

One of the failure modes occurring in laminated composites under impact loads is *delamination*. Delamination is driven by transverse shear and transverse normal stresses bearing at the interlaminar planes of a laminate. Dobyns [57] studied the dynamic loading of a simply supported plate. The loading is distributed over a small area of contact so that this region could simulate the projected cross sectional area of the striker. For the analysis, the plate is assumed to be specially orthotropic, and there exists uniform initial stress. Having given all of these, the assumed displacement field, including shear effect is given by

$$u = u^0(x, y, t) + z\Psi_x(x, y, t) \quad (2.46a)$$

$$v = v^0(x, y, t) + z\Psi_y(x, y, t) \quad (2.46b)$$

$$w = w(x, y, t) \quad (2.46c)$$

where u^0 , v^0 and w represent the displacements at the mid-plane of the plate in the x , y , and z directions, respectively, Ψ_x and Ψ_y represent the shear rotations in the x and y directions, respectively [57]

Whitney and Pagano [58] gave the equations of motion as

$$D_{11}\Psi_{x,xx} + D_{66}\Psi_{x,yy} + (D_{12} + D_{66})\Psi_{y,xy} - kA_{55}\Psi_x - kA_{55}w_{,x} + m_x = I\ddot{\Psi}_x \quad (2.47a)$$

$$(D_{12} + D_{66})\Psi_{x,xy} + D_{66}\Psi_{y,xx} + D_{22}\Psi_{y,yy} - kA_{44}\Psi_y - kA_{44}w_{,y} + m_y = I\ddot{\Psi}_y \quad (2.47b)$$

$$kA_{55}\Psi_{x,x} + (kA_{55} + N_x^0)w_{,xx} + kA_{44}\Psi_{y,y} + (kA_{44} + N_y^0)w_{,yy} + P_z + Kw = P\ddot{w} \quad (2.47c)$$

and the boundary conditions for the rectangular plate having uniform thickness with dimensions $(a \times b)$ is given by

$$w = \Psi_{x,x} = 0 \quad \text{at } x = 0, a \quad (2.48a)$$

$$w = \Psi_{y,y} = 0 \quad \text{at } y = 0, b \quad (2.48b)$$

where

$$(A_{ij}, D_{ij}) = \int_{-\frac{h}{2}}^{\frac{h}{2}} Q_{ij}(I, z^2) dz \quad (i, j = 1, 2, 6) \quad (2.49a)$$

$$A_{ij} = \int_{-\frac{h}{2}}^{\frac{h}{2}} C_{ij} dz \quad (i, j = 4, 5) \quad (2.49b)$$

$$(P, I) = \int_{-\frac{h}{2}}^{\frac{h}{2}} \rho(1, z^2) dz \quad (2.49c)$$

P_z , m_x and m_y : the distributed loads,

k : Mindlin shear correction factor,

h : plate thickness

Q_{ij} : reduced in-plane stiffness,

C_{ij} : transverse shear stiffness.

Solutions for w , Ψ_x , Ψ_y are given by Sierakowski and Chaturvedi [59]

$$w(x, y, t) = \frac{1}{P} \sum_m \sum_n \frac{q_{mn} \sin(m\pi x/a) \sin(n\pi y/b)}{w_{mn}} \int_0^t F(\tau) \sin w_{mn}(t-\tau) d\tau \quad (2.50a)$$

$$\Psi_x(x, y, t) = \frac{1}{P} \sum_m \sum_n \left(\frac{L_{12}L_{23} - L_{22}L_{13}}{L_{11}L_{22} - L_{12}^2} \right) x \cdot \frac{q_{mn} \cos(m\pi x/a) \cos(n\pi y/b)}{w_{mn}} \int_0^t F(\tau) \sin w_{mn}(t-\tau) d\tau \quad (2.50b)$$

$$\Psi_y(x, y, t) = \frac{1}{P} \sum_m \sum_n \left(\frac{L_{12}L_{13} - L_{11}L_{23}}{L_{11}L_{22} - L_{12}^2} \right) x \cdot \frac{q_{mn} \sin(m\pi x/a) \sin(n\pi y/b)}{w_{mn}} \int_0^t F(\tau) \sin w_{mn}(t-\tau) d\tau \quad (2.50c)$$

where

$$L_{11} = D_{11}(m\pi/a)^2 + D_{66}(n\pi/b)^2 + kA_{55} \quad (2.51a)$$

$$L_{12} = (D_{12} + D_{66})(m\pi/a)(n\pi/b) \quad (2.51b)$$

$$L_{13} = kA_{55}(m\pi/a) \quad (2.51c)$$

$$L_{22} = D_{66}(m\pi/a)^2 + D_{22}(n\pi/b)^2 + kA_{44} \quad (2.51d)$$

$$L_{23} = kA_{44}(n\pi/b) \quad (2.51e)$$

$$L_{33} = (kA_{55} + N_x^0)(m\pi/a)^2 + (kA_{44} + N_y^0)(n\pi/b)^2 + K \quad (2.51f)$$

q_{mn} : load distribution on the plate,

w_{mn} : natural frequencies of the target plate,

$F(t)$: loading distributed force.

The response of an orthotropic plate by the impact of a non-rigid striker is given by Goldsmith [44]

$$\alpha = w_2 - w_1(c) = v_i t - 1/m \int_0^t dt \int_0^t F dt - w_1(c) \quad (2.52)$$

where α is the difference between the displacement of the striker and deflection of the structure at the contact point (Figure (2.7)).

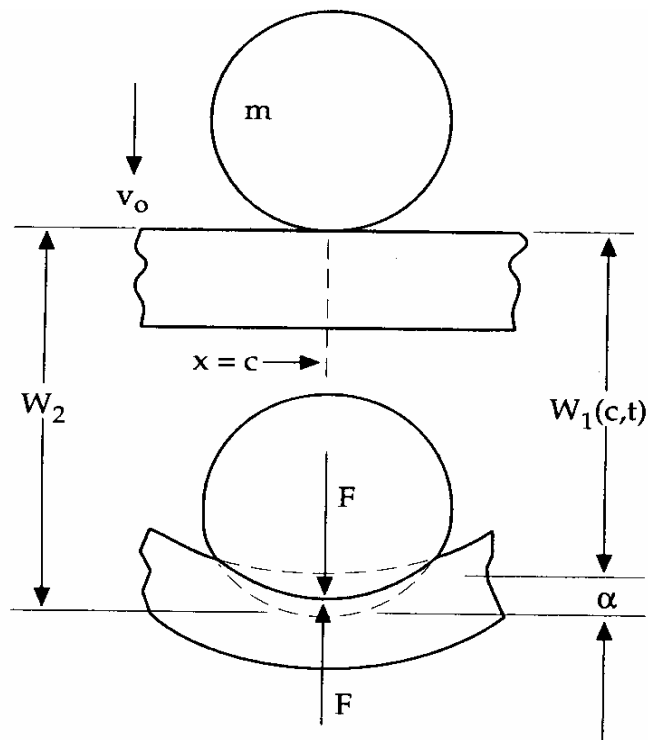


Figure 2.7 Response of an orthotropic plate by the impact of a non-rigid striker [60].

CHAPTER 3

NUMERICAL ANALYSIS OF THE BALLISTIC IMPACT PROBLEM

3.1 Introduction

The finite element method (FEM) is the most powerful numerical technique for solving solid and structural mechanics problems in geometrically complicated regions. The finite element analysis (FEA) of a problem is so systematic that it can be divided into a set of logical steps that can be implemented on a digital computer and can be used to solve variety of problems. Different solutions to different problems (having the same geometry) can be obtained by only changing input data that defines the domain of the problem, e.g. physical properties of the system, initial and boundary conditions.

The domain of the problem is the collection of nonintersecting simple subdomains which are called *finite elements*. The subdivision of a domain into elements is called the *finite element discretization* and the collection of the elements is called the *finite element mesh* of the domain which can be viewed as an approximation to the domain. Over each finite element, the solution of the governing equations is approximated by a linear combination of undetermined parameters and preselected approximation functions, almost always polynomials.

Since the solution is represented by polynomials on each element, a continuous approximation of the solution can be obtained only by requiring the continuity of the finite element solution, and possibly its derivatives, at element interfaces. The procedure of putting the elements together is called the *assembly* of elements [53].

3.2 Finite Element Analysis of the Impact Event

3.2.1 Nonlinear Dynamic Problems and Explicit Method

Nonlinearity means that response is not directly proportional to the action that produces it. In reality, nonlinearity is always present, but in many cases those nonlinearities can be ignored. When nonlinearity is important, software does not automatically detect that it should be taken into account and proceed to do the appropriate analysis.

In structural mechanics, nonlinearity is usually classified as material or geometric. In addition to these causes, changing status (including contact) can be viewed as a reason for the nonlinearity to occur. Material nonlinearity includes yielding and it is a result of nonlinear stress-strain relationship of the material. Geometric nonlinearity is a result of large deformations that a structure experiences. Many common structural features exhibit nonlinear behavior that is status-dependent. Status changes might be directly related to load or they might be determined by some external cause. Situations in which contact occurs are common to many different nonlinear applications. Contact is a distinctive and important category of changing-status nonlinearities.

Explicit and implicit time integration methods can be applied when nonlinearity is present. Explicit methods accommodate nonlinearity more easily than implicit methods do. Explicit methods require little computation time per step but demand a small time step as they are conditionally stable, and hence are best suited to short-duration loads such as impact. [61].

Although engineering processes can be considered as quasi-static processes, the dynamic explicit approach handles these processes as dynamic problems. To understand the basic approach, let's consider a simple mass-spring-damper system as in Figure 3.1.

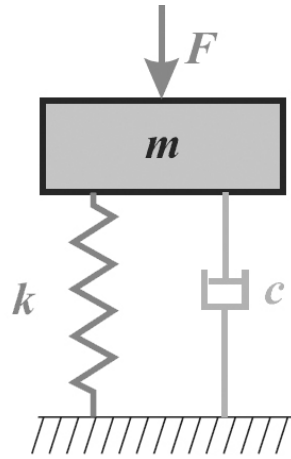


Figure 3.1 Mass-Spring-Damper system [62]

The equation of motion for mass-spring-damper system can be written in the following form:

$$m\ddot{u} + c\dot{u} + ku = F(t) \quad (3.1)$$

where

m : mass,

c : damping constant,

k : spring constant.

The motion equation can be re-written by dividing the whole equation by the mass m

$$\ddot{u} + 2\zeta w\dot{u} + w^2u = f(t) \quad (3.2)$$

where

$$w = \sqrt{\frac{k}{m}} \quad (\text{natural frequency}) \quad (3.3a)$$

$$\zeta = \frac{c}{(2\sqrt{mk})} \quad (\text{damping factor}) \quad (3.3b)$$

$$f(t) = \frac{F(t)}{m} \quad (3.3c)$$

At this points following points should be emphasized:

- $\zeta > 1$ for overdamped systems,
- $\zeta = 1$ for critically damped systems,
- $\zeta < 1$ for critically damped systems,
- For a given initial excitation a critically damped system tends to approach the equilibrium position the fastest.

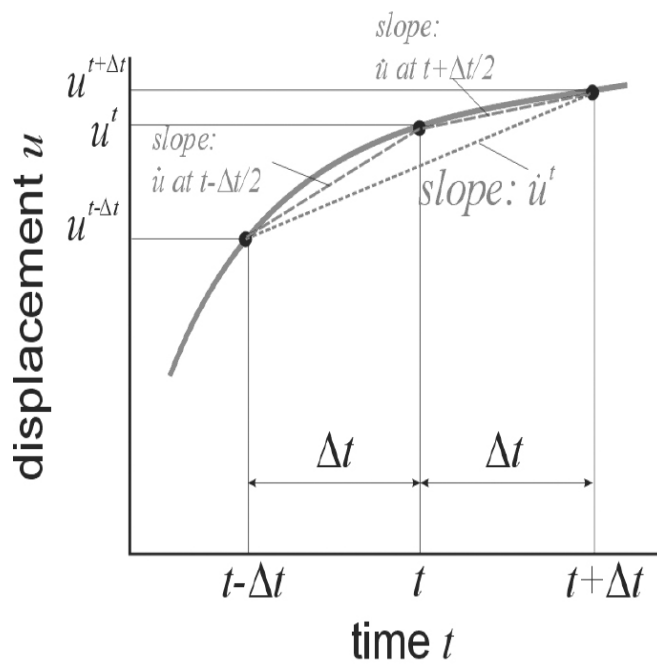


Figure 3.2 Displacement versus time graph [62].

Figure 3.2 represents the central difference method with constant time step. From this graph, the first and the second time derivatives at time t of the displacement can be inferred in the following form [62]:

$$\dot{u}^t = \frac{1}{2\Delta t} (u^{t+\Delta t} - u^{t-\Delta t}) \quad (3.4a)$$

$$\ddot{u}^t = \frac{1}{\Delta t} \left(\dot{u}^{t+\frac{\Delta t}{2}} - \dot{u}^{t-\frac{\Delta t}{2}} \right) \quad (3.4b)$$

where

$$\dot{u}^{t+\frac{\Delta t}{2}} = \frac{1}{\Delta t} (u^{t+\Delta t} - u^t) \quad (3.5a)$$

$$\dot{u}^{t-\frac{\Delta t}{2}} = \frac{1}{\Delta t} (u^t - u^{t-\Delta t}) \quad (3.5b)$$

Combining Equation (3.4b) with Equation (3.5a) and Equation (3.5b) yields

$$\ddot{u}^t = \frac{1}{\Delta t^2} (\dot{u}^{t+\Delta t} - 2u^t + u^{t-\Delta t}) \quad (3.6)$$

The equation of motion can be solved by applying the finite (central) difference method with Equation (3.4a) and (3.6) and yields

$$\left[\frac{1}{\Delta t^2} m + \frac{1}{2\Delta t} c \right] u^{t+\Delta t} = F(t) - ku^t + \frac{m}{\Delta t^2} [2u^t - u^{t-\Delta t}] + \frac{c}{2\Delta t} u^{t-\Delta t} \quad (3.7)$$

Since the solution for time $t+\Delta t$ is only depending on the displacements of the known states at times t and $t-\Delta t$, this approach is named as dynamic explicit integration of the motion equations [62].

3.3 Theory Behind the Numerical Analysis

The numerical analyses are performed using AUTODYN software [63, 64] which is used in non-linear dynamics. This type of program is sometimes referred to as a *hydrocode*. The phenomena to be studied with this program can be characterized as highly time dependent with both geometric non-linearities (e.g. large strains and deformations) and material non-linearities (e.g. plasticity, failure, strain-hardening and softening, multiphase equation of state).

In the numerical analysis, the motion of the system (continuum) is described by:

- Conservation of mass,
- Conservation of momentum,
- Conservation of energy,
- Material model,
- Initial conditions,
- Boundary conditions.

Once the above descriptions are made, the equations are solved numerically using explicit time integration and various solution techniques.

3.3.1 Conservation of Mass

Material associated with a Lagrangian zone stays with that zone (as opposed to the Euler zone where the zone remains unchanged and the material flows through it) under any deformation. Thus, a Lagrangian grid moves and distorts with the material it models and *conservation of mass* is automatically satisfied. The density at any time can be determined from the current volume of the zone and its initial mass

$$\rho = \frac{\rho_o V_o}{V} = \frac{m}{V} \quad (3.8)$$

where

ρ_0 = initial density,

V_0 = initial volume,

ρ = density at time $t > 0$,

V = volume at time $t > 0$.

3.3.2 Conservation of Momentum

The partial differential equations which express the *conservation of momentum* relate the acceleration to the stress tensor σ_{ij}

$$\rho \ddot{x} = \frac{\partial \sigma_{xx}}{\partial x} + \frac{\partial \sigma_{xy}}{\partial y} + \frac{\partial \sigma_{xz}}{\partial z} \quad (3.9a)$$

$$\rho \ddot{y} = \frac{\partial \sigma_{yx}}{\partial x} + \frac{\partial \sigma_{yy}}{\partial y} + \frac{\partial \sigma_{yz}}{\partial z} \quad (3.9b)$$

$$\rho \ddot{z} = \frac{\partial \sigma_{zx}}{\partial x} + \frac{\partial \sigma_{zy}}{\partial y} + \frac{\partial \sigma_{zz}}{\partial z} \quad (3.9c)$$

The stress tensor is separated into a hydrostatic component p and a deviatoric component

$$\sigma_{xx} = -(p + q) + s_{xx} \quad (3.10a)$$

$$\sigma_{yy} = -(p + q) + s_{yy} \quad (3.10b)$$

$$\sigma_{zz} = -(p + q) + s_{zz} \quad (3.10c)$$

$$\sigma_{xy} = s_{xy} \quad (3.10d)$$

$$\sigma_{yz} = s_{yz} \quad (3.10e)$$

$$\sigma_{zx} = s_{zx} \quad (3.10f)$$

The negative sign for the hydrostatic pressure p follows from the usual notation that stresses are positive in tension and negative in compression (the opposite to that for pressure).

The strain tensor ε_{ij} is determined from the relation between the strain rates and the velocities $(\dot{x}, \dot{y}, \dot{z})$

$$\dot{\varepsilon}_{xx} = \frac{\partial \dot{x}}{\partial x} \quad (3.11a)$$

$$\dot{\varepsilon}_{yy} = \frac{\partial \dot{y}}{\partial y} \quad (3.11b)$$

$$\dot{\varepsilon}_{zz} = \frac{\partial \dot{z}}{\partial z} \quad (3.11c)$$

$$\dot{\varepsilon}_{xy} = \frac{1}{2} \left(\frac{\partial \dot{x}}{\partial y} + \frac{\partial \dot{y}}{\partial x} \right) \quad (3.11d)$$

$$\dot{\varepsilon}_{yz} = \frac{1}{2} \left(\frac{\partial \dot{y}}{\partial z} + \frac{\partial \dot{z}}{\partial y} \right) \quad (3.11e)$$

$$\dot{\varepsilon}_{zx} = \frac{1}{2} \left(\frac{\partial \dot{z}}{\partial x} + \frac{\partial \dot{x}}{\partial z} \right) \quad (3.11f)$$

and these strain rates are related to the rate of change of volume by:

$$\frac{\dot{V}}{V} = \dot{\varepsilon}_{xx} + \dot{\varepsilon}_{yy} + \dot{\varepsilon}_{zz} \quad (3.12)$$

Derivation of the elastic behavior of the material can be derived by using Equation (3.12) and Hooke's Law relations between the deviatoric stress rates and strain rates

$$\dot{s}_{xx} = 2G \left(\dot{\varepsilon}_{xx} - \frac{\dot{V}}{3V} \right) \quad (3.13a)$$

$$\dot{s}_{yy} = 2G \left(\dot{\epsilon}_{yy} - \frac{\dot{V}}{3V} \right) \quad (3.13b)$$

$$\dot{s}_{zz} = 2G \left(\dot{\epsilon}_{zz} - \frac{\dot{V}}{3V} \right) \quad (3.13c)$$

$$\dot{s}_{xy} = 2G \epsilon_{xy} \quad (3.13d)$$

$$\dot{s}_{yz} = 2G \epsilon_{yz} \quad (3.13e)$$

$$\dot{s}_{zx} = 2G \epsilon_{zx} \quad (3.13f)$$

3.3.3 Conservation of Energy

The pressure p is related to the density ρ and specific internal energy e through an equation of state

$$p = f(\rho, e) \quad (3.14)$$

Equation (3.14) must be solved simultaneously with the equation expressing *conservation of energy*:

$$\dot{e} = \frac{1}{\rho} \left(\sigma_{xx} \dot{\epsilon}_{xx} + \sigma_{yy} \dot{\epsilon}_{yy} + \sigma_{zz} \dot{\epsilon}_{zz} + 2\sigma_{xy} \dot{\epsilon}_{xy} + 2\sigma_{yz} \dot{\epsilon}_{yz} + 2\sigma_{zx} \dot{\epsilon}_{zx} \right) \quad (3.15)$$

3.3.4 Material Model

In most cases, the stress tensor may be separated into a uniform *hydrostatic pressure* (all three normal stresses equal) and a *stress deviatoric tensor* and these stress components are responsible for two different material deformations under impact conditions. First one is the volumetric-stress due to changes in volume (pressure) which is defined by the equation of state (EOS). The second one is deviatoric-stress due to changes in shape and it is defined by the strength model.

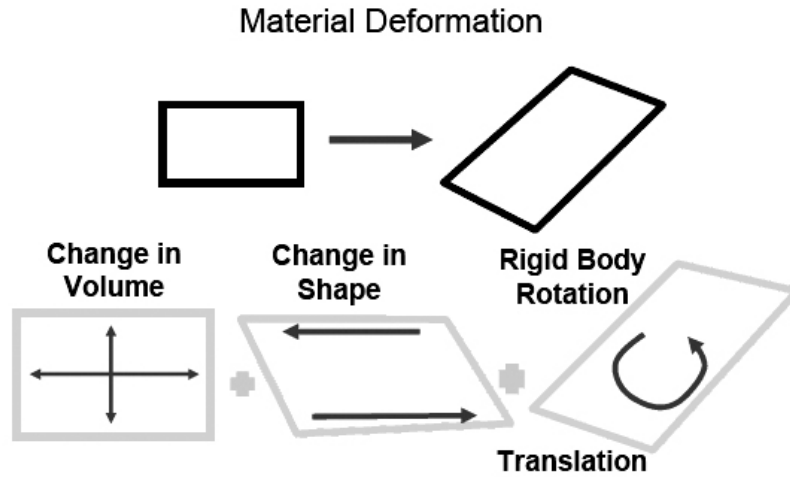


Figure 3.3 Material deformation histories [64].

In addition to these, for a solid, it is necessary to specify a failure criterion as materials can only sustain limited tensile stresses.

The state of stress (in 3D) on a material subject to small, linear, elastic strains (reversible deformation) can be described by six stress components ($\sigma_{xx}, \sigma_{yy}, \sigma_{zz}, \sigma_{xy}, \sigma_{yz}, \sigma_{xz}$). It is always possible to choose a coordinate system such that the shear stresses are zero ($\sigma_{12} = \sigma_{23} = \sigma_{31} = 0$) at the point under consideration which is known as the *Principal Axes*. The stresses in the direction of the principal axes on the surfaces normal to these axes are known as the *Principal Stresses* and are denoted as σ_1, σ_2 and σ_3 .

A perfectly elastic material has a linear relationship between stress and strain, and Hooke's law relates the stress at a point to the strain at the point. In terms of an incremental strain resulting in an incremental stress this may be written as

$$\dot{\sigma}_i = \lambda \left(\frac{\dot{V}}{V} \right) + 2G\dot{\epsilon}_i \quad i=1,2,3. \quad (3.16)$$

where λ and G are the Lamé constants (G is also known as the *Shear Modulus*), $\dot{\epsilon}_1, \dot{\epsilon}_2, \dot{\epsilon}_3$ are the strain rates in the directions of the principal axes, and V is the volume. The dot describes a time derivative along a particle path.

As mentioned earlier, the stresses can be decomposed into a hydrostatic and a deviatoric component

$$\sigma_i = -P + s_i \quad (3.17a)$$

$$P = -\frac{1}{3}(\sigma_1 + \sigma_2 + \sigma_3) \quad i = 1,2,3. \quad (3.17b)$$

where P is then hydrostatic pressure and s_i 's are the stress deviators.

As with the stresses the strain components are defined as the sum of a *mean normal strain* ϵ and *deviatoric strain* components θ_1, θ_2 and θ_3 where

$$\dot{\epsilon}_1 + \dot{\epsilon}_2 + \dot{\epsilon}_3 = \frac{\dot{V}}{V} \quad (3.18a)$$

$$\dot{\theta}_1 + \dot{\theta}_2 + \dot{\theta}_3 = 0 \quad (3.18b)$$

$$\dot{\epsilon} = \frac{\dot{V}}{3V} \quad (3.18c)$$

With the above definitions Hooke's law may be rewritten:

$$\dot{s}_i = 2G \left(\dot{\epsilon}_i - \frac{\dot{V}}{3V} \right) \quad i = 1,2,3 \quad (3.19a)$$

$$P = K \cdot \mu \quad (3.19b)$$

where

$$K = \left(\lambda + \frac{2G}{3} \right) \quad (3.20)$$

It also follows that:

$$\dot{s}_1 + \dot{s}_2 + \dot{s}_3 = 0 \quad (3.21)$$

and hence

$$s_1 + s_2 + s_3 = 0 \quad (3.22)$$

which may be interpreted as stating that the deviatoric components of the stresses do not contribute to the average (hydrostatic) pressure but only to distortion of the volume.

The concept of elastic distortion is that if the material is loaded and subsequently unloaded all the distortion energy is recovered and the material will revert to its initial configuration. However, real materials are unable to support arbitrarily large shear stresses so if the distortion is too great the material will reach its elastic limit and begins to distort plastically. If the material is subsequently unloaded only the elastic distortion energy will be recovered and the material will suffer permanent plastic strain.

Several proposed yield criteria are to be found in the literature, e.g. the Tresca condition which puts a predefined limit on the shear stress. This however does not define a smooth yield surface.

The differences between the various yield criteria are usually much smaller than the uncertainties in the applicable material constants. The *Von Mises yield criterion* is used in AUTODYN (as in most hydrocodes) to describe the elastic limit and transition to plastic flow.

This is a simple and convenient criterion to apply, defines a smooth and continuous yield surface and is a good approximation at high stress levels. This states that, given the principal stresses $(\sigma_1, \sigma_2, \sigma_3)$, the local yield condition is

$$(\sigma_1 - \sigma_2)^2 + (\sigma_2 - \sigma_3)^2 + (\sigma_3 - \sigma_1)^2 = 2Y^2 \quad (3.23)$$

where Y is the yield strength in simple tension. This can be also written as

$$(s_1 - s_2)^2 + (s_2 - s_3)^2 + (s_3 - s_1)^2 = 2Y^2 \quad (3.24)$$

and with Equation 3.22, Equation 3.24 reduces to

$$s_1^2 + s_2^2 + s_3^2 = \frac{2Y^2}{3} \quad (3.25)$$

Thus the onset of yielding, i.e. of plastic flow, is purely a function of the deviatoric stresses (distortion) and does not depend upon the value of the local hydrostatic pressure unless the yield stress Y itself is a function of pressure. The left hand side of Equation 3.25 is proportional to the elastic energy of distortion per unit volume or the energy required to change shape as opposed to the energy that causes a volume change. The expression states therefore that plastic flow begins when the elastic distortion energy reaches a limiting value $\{Y^2 / 6G\}$ and that this energy remains constant during the plastic flow when plastic work (i.e. irrecoverable work) will be done.

In $(\sigma_1, \sigma_2, \sigma_3)$ space, this equation describes the surface of a straight circular cylinder whose axis is equally inclined to the $\sigma_1, \sigma_2, \sigma_3$ system of coordinates as shown in Figure 3.4.

consideration has been given to the behavior of materials for densities less than normal.

The ideal equation of state would cover all regions in the phase plane as shown in Figure 3.5. The two-phase states should cover both the liquid-vapor regions at high temperatures and positive pressures and cavitated states where gaseous bubbles can form in a liquid when the pressure falls below a reference state and the temperature is also low. To determine a single analytic relationship to encompass all these greatly different regions of phase space would be impossible and many approaches have been made to provide analytic fits which are valid only in limited regions of the values of internal energy and volume, i.e. in (e,v) space.

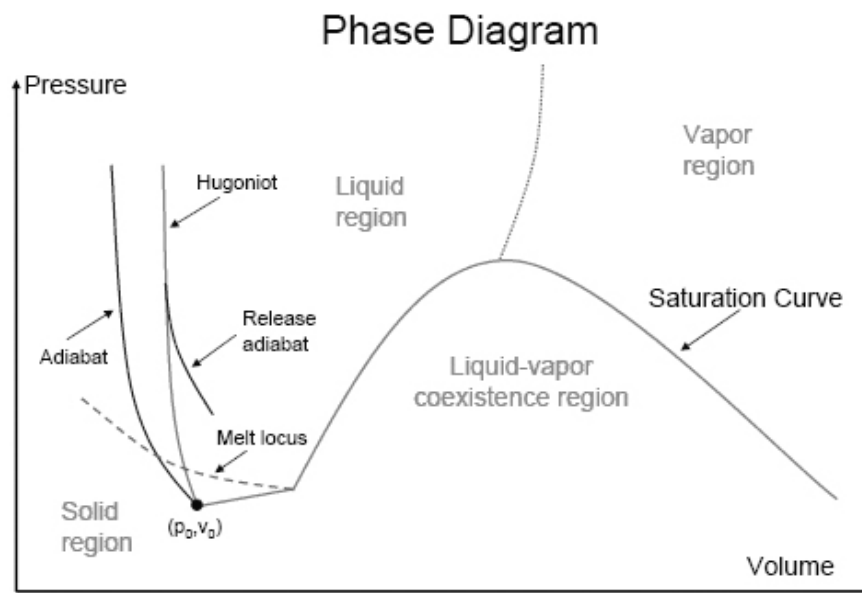


Figure 3.5 Phase Diagram, Hugoniot and Adiabats [64].

Since many of the early problems were of materials deformed by strong dynamic impact (or shocks), these forms of early equations of state concentrated on the material behavior on or near the region of states to which the material may reach if it is shocked from its initial state. The locus in the pressure-volume (p,v) plane

of all states achievable by shocking the material from an initial state (p_0, v_0) is known as the *shock Hugoniot*.

The experimental fact is that for most solids and many liquids, which do not undergo a phase change, the values on the shock Hugoniot for shock velocity U and material

velocity behind the shock u_p can be adequately fitted to a straight line

$$U = c_0 + su_p \quad (3.26)$$

where c_0 is the sound speed and s is the slope of the U - u_p relation.

This is the case even up to shock velocities around twice the initial sound speed and shock pressures of order 100 GPa. For materials where a linear fit is not adequate a quadratic form in u_p has sometimes been used or at other times piecewise linear or piecewise quadratic (U, u_p) forms have been used.

The equation of state can be determined from the knowledge of the thermodynamic properties of the material and ideally should not require dynamic data to build up the relationship. However, in practice, the only way to obtain the data on the behavior of the material at high strain rates is to carry out well-characterized dynamic experiments.

3.3.5 Failure Models

Most materials can only withstand relatively small tensile stresses and/or strains before they fail. The post-failure behavior of a cell can either be instantaneous (failure occurs the cycle the criteria is reached) or gradual (the ability of the material to sustain future tensile stresses is gradually reduced).

3.3.6 Lagrange Meshes

A specific region of interest covered by a set (or grid) of brick shaped zones, elements or cells on which the flow and state variables (position, velocity, pressure etc.) is known as *Lagrange subgrid* and it is defined within a Lagrangian coordinate system. A subgrid is a group of cells (or zones) which is regular in index space (I, J, K space) although it may form an irregular volume in (x,y,z) space. Each brick element within the subgrid has eight corner (3D) nodes forming in (x,y,z) space a generalized hexahedral shape with, in general, non-planar faces. The index space of each subgrid is independent of any of the other subgrids defined in the problem. As shown in Figure 3.6, each subgrid node is identified by its unique (I,J,K) index while each zone interior is defined by a unique (I,J,K) index which is identified with the upper-rightmost (in (I,J,K) space) node of the zone.

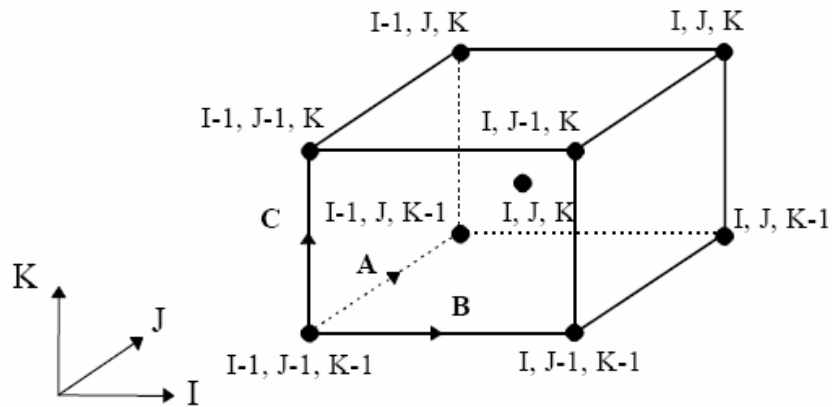


Figure 3.6 Lagrange subgrid [63].

The partial differential equations are replaced by the finite difference equations, based on cells of the subgrid, and these difference equations are solved to update the solution by successive time steps.

The series of calculations that are carried out in each incremental time step (or cycle) in a Lagrange subgrid are described in Figure 3.7. The boundary and/or interactive forces are updated and combined with the forces for inner zones computed during the previous time cycle. Then, for all non-interactive Lagrangian nodes the accelerations, velocities and positions are computed from the momentum equation and a further integration. From these values the new zonal volumes and strain rates maybe calculated. With the use of a material model together with the energy equation the zonal pressures, stresses and energies may be calculated, providing forces for use at the start of next integration cycle.

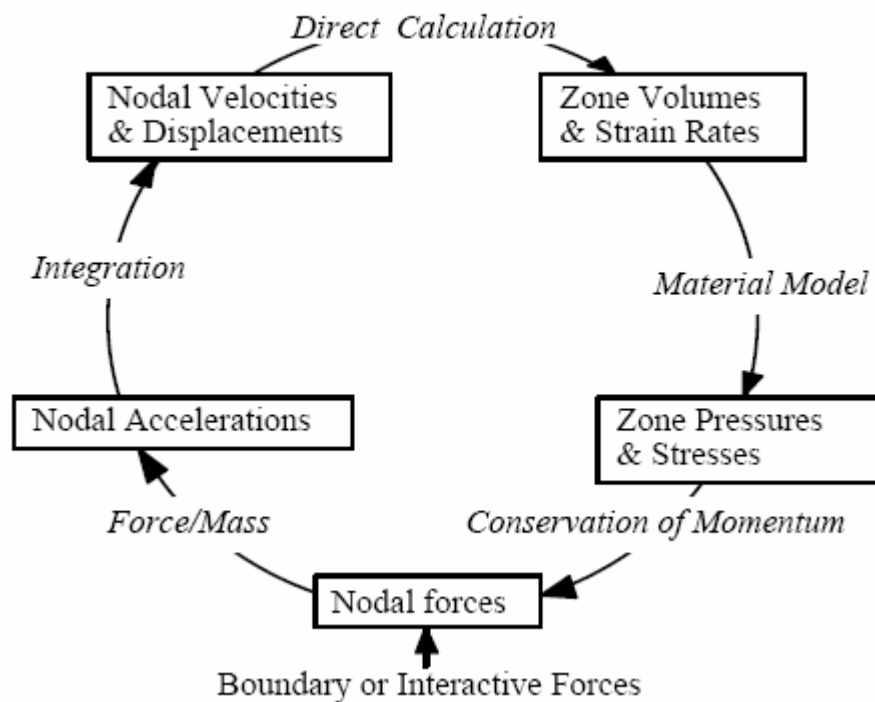


Figure 3.7 Calculation cycle [63].

3.3.7 Time Step

Since the numerical algorithm used in the software is an explicit scheme, there is a maximum time step of integration which must be observed if the numerical solution obtained is to be a reasonable representation of the true solution. The value of this time step depends on several parameters of the numerical method and solution so the local time step ensuring stability is calculated for each mesh point. The minimum value of all these local values is multiplied by a safety factor and this is chosen as the time step for the next update.

In a Lagrangian mesh, the time step must satisfy the CFL or Courant Condition,

$$\Delta t \leq \frac{d}{c} \quad (3.27)$$

where d is a typical length of a zone (defined as the volume of the zone divided by the square of the longest diagonal of the zone and scaled by $\sqrt{2/3}$) and c is the local sound speed. This ensures that a disturbance does not propagate across a zone in a single time step.

3.3.8 Smoothed Particle Hydrodynamics (SPH) Solver

SPH is a Lagrangian technique having the potential to be both efficient and accurate at modeling material deformation and flexible in terms of the inclusions of specific material models. In addition, SPH is a gridless technique so it does not suffer from the normal problem of grid tangling in large deformation problems.

The main potential advantages of SPH technique are:

- It does not require a numerical grid
- No grid tangling problems as in standard grid based Lagrangian techniques
- Efficient tracking of material deformation and history dependent behavior

The name SPH includes the term “Particle”. Although this is appropriate for describing the Lagrangian motion of mass points in SPH, it is misleading because the “Particles” are really interpolation points. Consider a rod of steel that is represented by a series of SPH particles as shown in Figure 3.8.

The density at particle I can be calculated using an expression such as

$$\rho^I = \sum_{j=1}^N m^J W^{IJ} (x^I - x^J h) \quad (3.28)$$

where

m^J : the mass of particle J,

W^{IJ} : a weighting function,

x : the position of the center of a particle,

h : smoothing length or particle size.

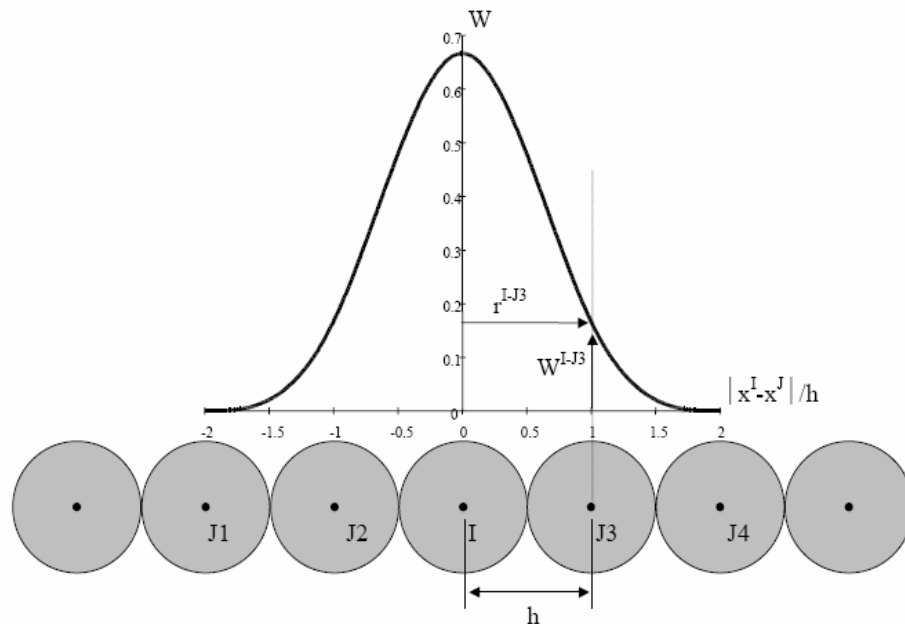


Figure 3.8 Rod of steel with SPH particles [63].

To calculate the value of a function at particle I , in this case the density, the value of the function at all neighboring particles (interpolation points $J1, J2, I, J3, J4$) multiplied by a weighting function. Hence, the SPH particles are not simply interacting mass points but they are interpolation points from which values of functions, and their derivatives, can be estimated at discrete points in the continuum. In SPH, the particle points at which all quantities are evaluated are placed at the center of the SPH particles.

The basic steps used in each calculation cycle in SPH are shown in Figure 3.9.

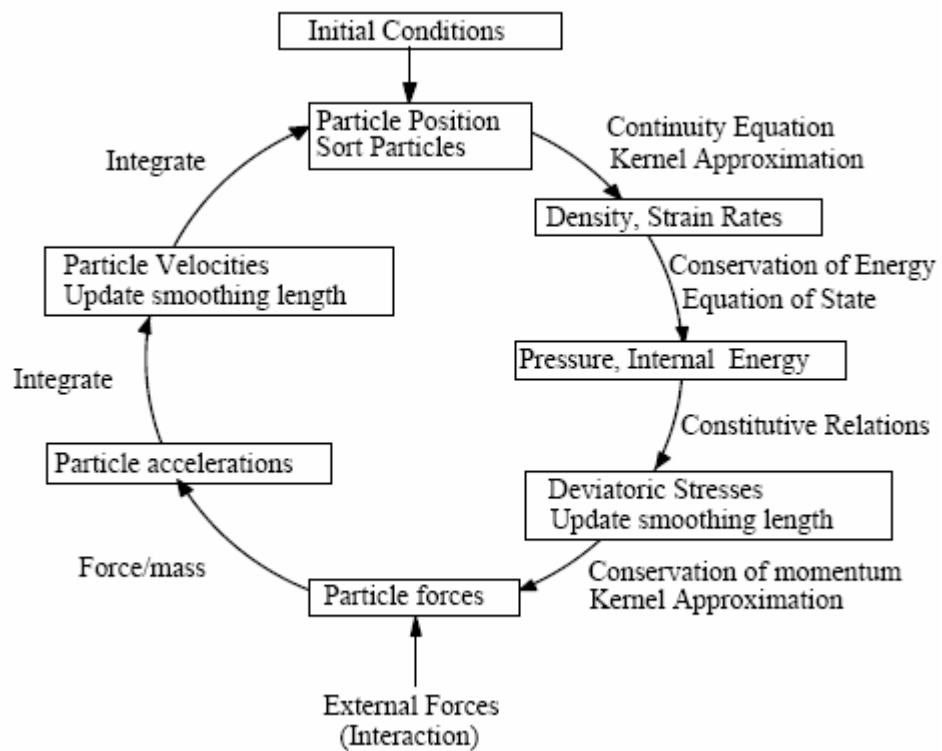


Figure 3.9 Calculation cycle (SPH).[63]

3.4 Description of the Material Models Used In Numerical Simulations

3.4.1 Johnson-Cook Strength Model For The Projectile

The model [65] for the von Mises flow stress, σ , is expressed as

$$\sigma = (A + B\varepsilon^n)(1 + C \ln \dot{\varepsilon}^*)(1 - T^{*m}) \quad (3.29)$$

where ε is the equivalent plastic strain, $\dot{\varepsilon}^* = \dot{\varepsilon} / \varepsilon_0^*$ is the dimensionless plastic strain rate for $\varepsilon_0^* = 1.0s^{-1}$ and T^* is the *homologous temperature*,

$$T^* = \frac{T - T_{room}}{T_{melt} - T_{room}} \quad (3.30)$$

The five material constants are A , B , n , C and m . A is the yield stress and B and n represent the effects of strain hardening and C is the strain rate constant. The expression in the first bracket gives the stress as a function of strain rate for $\dot{\varepsilon}^* = 1.0$ and $T^* = 0$. The expressions in the second and third bracket represent the effects of strain rate and temperature, respectively. The constants in these expressions were obtained by Johnson and Cook empirically by means of dynamic Hopkinson bar tensile tests over a range of temperatures and some other tests and checked by calculations of Taylor tests of impacting metal cylinders on rigid metal targets which provided strain rates in excess of $10^5 s^{-1}$ and strains in excess of 2.0 [65].

3.4.2 Johnson-Cook Failure Model For The Projectile

The damage to an element is defined [66],

$$D = \sum \frac{\Delta \varepsilon}{\varepsilon^f} \quad (3.31)$$

where $\Delta \varepsilon$ is the increment of equivalent plastic strain which occurs during an integration cycle, and ε^f is the equivalent strain to fracture, under the current conditions of strain rate, temperature, pressure and equivalent stress. Fracture is then allowed to occur when $D = 1.0$.

The general expression for the strain at fracture is given by

$$\varepsilon^f = \left(D_1 + D_2 e^{D_3 \cdot \sigma^*} \right) (1 + D_4 \ln \dot{\varepsilon}^*) (1 + D_5 T^*) \quad (3.32)$$

The dimensionless pressure stress ratio is defined as $\sigma^* = \sigma_m / \bar{\sigma}$ where σ_m is the average of the three normal stresses and $\bar{\sigma}$ is the von Mises equivalent stress. The dimensionless strain rate, $\dot{\varepsilon}^*$, and homologous temperature, T^* , are identical to those used in the Johnson-Cook Strength Model.

The expression in the first brackets reveals the pressure dependence of the fracture. It essentially says that the strain to fracture decreases as the hydrostatic tension, σ_m increases. The expression in the second set of brackets represents the effect of strain rate, and that in the third set of brackets represents the effect of temperature.

3.4.3 Johnson-Holmquist (JH) Strength Model For The Ceramic Armor

Ceramic materials have been considered for armor applications for many years. They are generally strong in compression, weak in tension, and can have considerable strength after failure when they are under compression [67].

The JH ceramic model is summarized in Figure 3.10, 3.11 and 3.12. Equivalent strength, σ , is dependent on the pressure, the dimensionless strain rate $\dot{\epsilon}^* = \dot{\epsilon} / \dot{\epsilon}_0^*$ (for $\dot{\epsilon}_0^* = 1.0s^{-1}$), and the damage, D . For undamaged material, $D = 0.0$; for partially damaged material, $0 < D \leq 1.0$; and for totally damaged (failed) material, $D = 1.0$. The strength is greatly reduced after the material fail, but it can be significant and cannot be ignored. T is the maximum tensile hydrostatic pressure the material can experience, and S_1 and S_2 are the strengths of the intact (undamaged) material (for $\dot{\epsilon}^* = 1.0$) at compressive pressures P_1 and P_2 , respectively. After the material has failed ($D = 1.0$), the slope of the strength of the failed material is given by α , and the maximum failure strength is S_{\max}^f (for $\dot{\epsilon}^* = 1.0$).

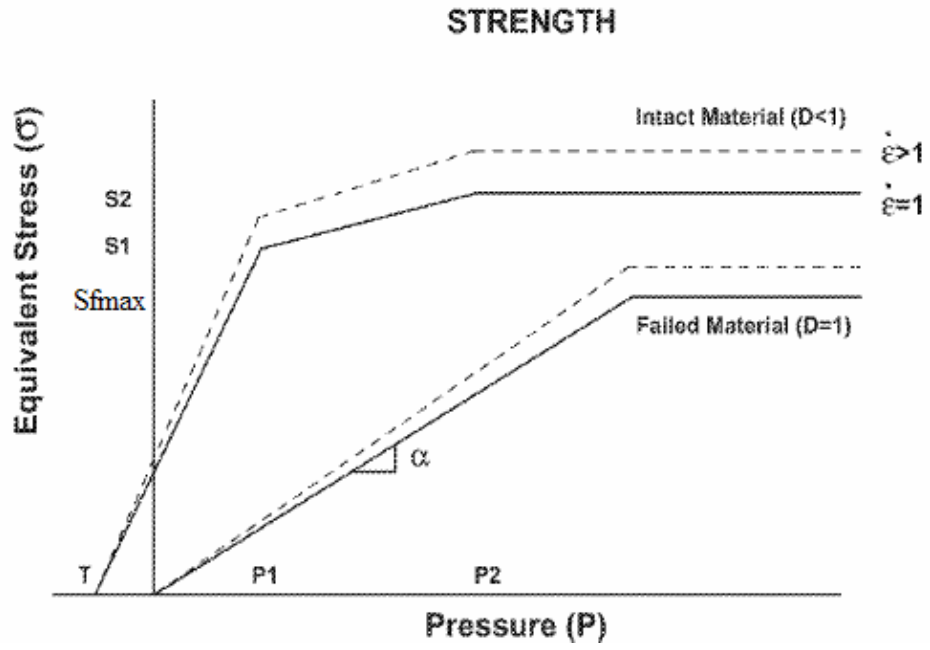


Figure 3.10 JH-1 Strength Model [67].

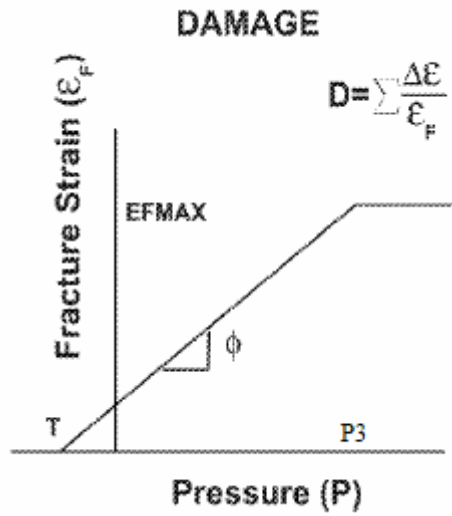


Figure 3.11 JH-1 Damage Model [67].

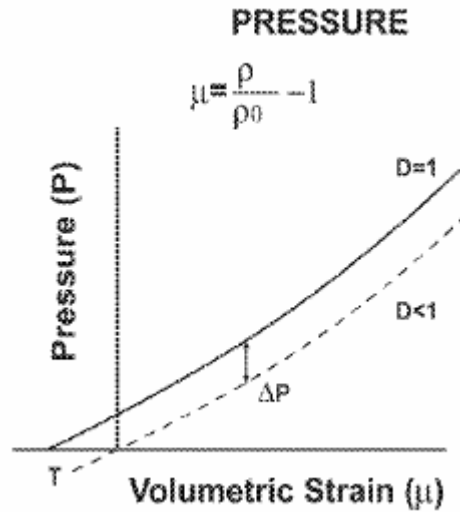


Figure 3.12 Pressure-volumetric strain [67].

The strain rate constant is C . If σ_0 is the available strength at $\dot{\epsilon}^* = 1.0$, then the strength at the other strain rates is

$$\sigma = \sigma_0 (1.0 + \ln \dot{\epsilon}^*) \quad (3.33)$$

It can be seen that the strength increases significantly with pressure, which is consistent with well-known fact that brittle materials are much stronger in compression.

3.4.4 Johnson-Holmquist (JH) Fracture Model For The Ceramic Armor

The damage for fracture [68] is accumulated in a similar manner to that used in the Johnson-Cook fracture model. It is expressed as

$$D = \sum \frac{\Delta \epsilon^p}{\epsilon_p^f} \quad (3.34)$$

where $\Delta\varepsilon^p$ is the plastic strain during a cycle of integration and $\varepsilon_p^f = f(P)$ is the plastic strain to fracture under a constant pressure, P . From Figure 3.11, the material cannot undergo any plastic strain at the maximum hydrostatic tension, T , but it increases to $\varepsilon_p^f = \varepsilon_{\max}^f$ at a compressive pressure of $P=P_3$.

The hydrostatic pressure before failure ($D < 1.0$) is simply

$$P = K_1\mu + K_2\mu^2 + K_3\mu^3 \quad (3.35)$$

where K_1 , K_2 and K_3 are constants (K_1 is the bulk modulus); and $\mu = V_0/V - 1 = \rho/\rho_0 - 1$ for current volume V , initial volume V_0 , current density ρ , and initial density ρ_0 . For tensile pressures ($\mu < 0$), Equation 3.35 is replaced by

$$P = K_1\mu \quad (3.36)$$

After failure (when $D=1.0$) *bulking* (pressure increase and/or volumetric strain increase) can occur. This provides an additional incremental pressure ΔP , such that

$$P = K_1\mu + K_2\mu^2 + K_3\mu^3 + \Delta P. \quad (3.37)$$

The pressure increment is determined from energy considerations. From Figure 3.10, it can be seen that there is a drop in strength when the material goes from an intact state ($D < 1.0$) to a failed state ($D=1.0$). This represents a loss in the elastic internal energy of the deviator and shear stress. The general expression for this internal energy is

$$U = \left[s_x^2 + s_y^2 + s_z^2 - 2\nu(s_x s_y + s_y s_z + s_z s_x) + 2(1 + \nu)(\tau_{xy}^2 + \tau_{yz}^2 + \tau_{zx}^2) \right] / (2E), \quad (3.38)$$

where s_x, s_y, s_z are the normal deviator stresses; $\tau_{xy}, \tau_{yz}, \tau_{zx}$ are the shear stresses; ν is the Poisson's ratio; and E is the modulus of elasticity.

The loss in this elastic internal energy can be expressed as

$$\Delta U = U_i - U_f \quad (3.39)$$

where U_i is the elastic energy of the intact material before failure ($D < 1.0$) and U_f is the elastic energy immediately after failure ($D=1.0$).

This energy loss (of deviator and shear stresses) can be converted to potential hydrostatic energy by adding ΔP . An approximate equation for the energy conversion is

$$\Delta P \mu_f + \Delta P / (2K_1) = \beta \Delta U \quad (3.40)$$

where μ_f is μ at fracture and β is the fraction ($0 \leq \beta \leq 1.0$) of the elastic energy loss converted to potential hydrostatic energy. The first term ($\Delta P \mu_f$) in Equation 3.40 is the approximate potential energy for $\mu > 0$, and the second term ($\Delta P / (2K_1)$) is the corresponding potential energy for $\mu < 0$. Solving for ΔP gives

$$\Delta P = -K_1 \mu_f + \sqrt{(K_1 \mu_f)^2 + 2\beta K_1 \Delta U} \quad (3.41)$$

Note that $\Delta P = 0$ for $\beta = 0$ and that ΔP increases as ΔU increases and/or μ_f decreases.

3.4.5 Orthotropic Material Model For The Composite Armor

In general the behavior of composite laminates can be represented through a set of orthotropic constitutive relations. Some of the relationships are described which assume the material behavior remains elastic and the volumetric response linear. For more complicated material response a methodology was developed [69] which allows a non-linear equation of state to be used in conjunction with an orthotropic stiffness matrix. This is important when modeling applications such as hypervelocity impacts. In order to model such observed non-linear behavior an orthotropic hardening model has been implemented [70].

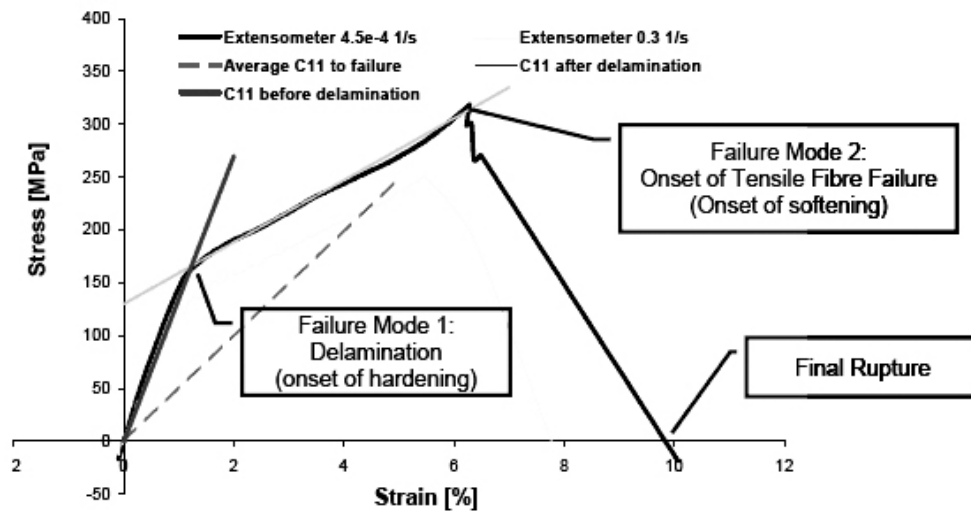


Figure 3.13 Typical in-plane stress-strain behavior of Kevlar™-epoxy [70].

For composites, the macroscopic properties are not identical in all directions. In general, the behavior of such materials is represented through a set of orthotropic constitutive relations. Constitutive relations for this type of material are conventionally based on a total stress formulation, as opposed to dividing the total stress into hydrostatic and deviatoric components. Thus, the incremental stress-strain relations can be expressed as

$$[\sigma]^{n+1} = [\sigma]^n + [C][\dot{\epsilon}]\Delta t \quad (3.42)$$

where $[C]$ is the stiffness matrix, $[\dot{\epsilon}]$ strain rate tensor and Δt is the time step.

The material model developed in [71] provides a mechanism in an orthotropic material to calculate:

- The contributions to pressure from the isotropic and deviatoric strain components,
- The contributions to the deviatoric stress from the deviatoric strains.

Further, this methodology gives rise to the possibility for incorporating non-linear effects (such as shock effects) that can be attributed to the volumetric straining in the material. To use this model 'Ortho' is selected as the equation state for the material and either 'Polynomial' or 'Shock' for the volumetric response option.

The incremental linear elastic constitutive relations for an orthotropic material can be expressed as

$$\begin{pmatrix} \Delta\sigma_{11} \\ \Delta\sigma_{22} \\ \Delta\sigma_{32} \\ \Delta\sigma_{23} \\ \Delta\sigma_{31} \\ \Delta\sigma_{12} \end{pmatrix} = \begin{pmatrix} C_{11} & C_{12} & C_{13} & 0 & 0 & 0 \\ & C_{22} & C_{23} & 0 & 0 & 0 \\ & & C_{33} & 0 & 0 & 0 \\ & & & C_{44} & 0 & 0 \\ & & & & C_{55} & 0 \\ & sym. & & & & C_{66} \end{pmatrix} \begin{pmatrix} \Delta\epsilon_{11} \\ \Delta\epsilon_{22} \\ \Delta\epsilon_{33} \\ \Delta\epsilon_{23} \\ \Delta\epsilon_{31} \\ \Delta\epsilon_{12} \end{pmatrix} \quad (3.43)$$

In order to include non-linear shock effects in the above linear relations, it is first desirable to separate the volumetric (thermodynamic) response of the material from its ability to carry shear loads (strength). Hence, it is convenient to split the strain increments into their average, $\Delta\epsilon_{ave}$, and deviatoric, $\Delta\epsilon_{ij}^d$, components;

$$\Delta\epsilon_{ij} = \Delta\epsilon_{ij}^d + \Delta\epsilon_{ave} \quad (3.44)$$

Now, defining the average direct strain increment, $\Delta\epsilon_{ave}$, as a third of the trace of the strain tensor;

$$\Delta\epsilon_{ave} = \frac{1}{3}(\epsilon_{11} + \epsilon_{22} + \epsilon_{33}) \quad (3.45)$$

and assuming, for small strain increments, the volumetric strain increment is defined as

$$\Delta\epsilon_{vol} \approx \epsilon_{11} + \epsilon_{22} + \epsilon_{33} \quad (3.46)$$

The total strain increments can be expressed in terms of the volumetric and deviatoric strain increments resulting in the following orthotropic constitutive relation

$$\begin{pmatrix} \Delta\sigma_{11} \\ \Delta\sigma_{22} \\ \Delta\sigma_{32} \\ \Delta\sigma_{23} \\ \Delta\sigma_{31} \\ \Delta\sigma_{12} \end{pmatrix} = \begin{pmatrix} C_{11} & C_{12} & C_{13} & 0 & 0 & 0 \\ & C_{22} & C_{23} & 0 & 0 & 0 \\ & & C_{33} & 0 & 0 & 0 \\ & & & C_{44} & 0 & 0 \\ & & & & C_{55} & 0 \\ & sym. & & & & C_{66} \end{pmatrix} \begin{cases} \Delta\epsilon_{11}^d + \frac{1}{3} \Delta\epsilon_{vol} \\ \Delta\epsilon_{22}^d + \frac{1}{3} \Delta\epsilon_{vol} \\ \Delta\epsilon_{33}^d + \frac{1}{3} \Delta\epsilon_{vol} \\ \Delta\epsilon_{23} \\ \Delta\epsilon_{31} \\ \Delta\epsilon_{12} \end{cases} \quad (3.47)$$

To find the equivalent pressure increment, the pressure is defined as a third of the trace of the stress increment tensor

$$\Delta P = -\frac{1}{3}(\sigma_{11} + \sigma_{22} + \sigma_{33}) \quad (3.48)$$

If Equation 3.47 are expanded, the deviatoric and volumetric terms grouped and the direct stress increments are substituted in Equation 3.48:

$$\begin{aligned}
\Delta P = & -\frac{1}{9}[C_{11} + C_{22} + C_{33} + 2(C_{12} + C_{23} + C_{31})]\Delta\epsilon_{vol} \\
& -\frac{1}{3}(C_{11} + C_{21} + C_{31})\Delta\epsilon_{11}^d \\
& -\frac{1}{3}(C_{12} + C_{22} + C_{32})\Delta\epsilon_{22}^d \\
& -\frac{1}{3}(C_{13} + C_{23} + C_{33})\Delta\epsilon_{33}^d
\end{aligned} \tag{3.49}$$

from which the contributions to the pressure from volumetric and deviatoric components of strain can clearly be identified.

The first term in Equation 3.49 can be used to define the volumetric (thermodynamic) response of an orthotropic material in which the effective bulk modulus of the material K' is,

$$K' = \frac{1}{9}[C_{11} + C_{22} + C_{33} + 2(C_{12} + C_{23} + C_{31})] \tag{3.50}$$

For the inclusion of non-linear shock effects, the contribution to pressure from volumetric strain is modified to include non-linear terms. The final incremental pressure calculation becomes

$$\begin{aligned}
\Delta P = & \Delta P_{EOS}(\epsilon_{vol}, e) \\
& -\frac{1}{3}(C_{11} + C_{21} + C_{31})\Delta\epsilon_{11}^d \\
& -\frac{1}{3}(C_{12} + C_{22} + C_{32})\Delta\epsilon_{22}^d \\
& -\frac{1}{3}(C_{13} + C_{23} + C_{33})\Delta\epsilon_{33}^d
\end{aligned} \tag{3.51}$$

where the pressure contribution ΔP_{EOS} from volumetric strains can include the non-linear shock (thermodynamic) effects and energy dependence as in a conventional equation of state.

The quadratic yield/flow surface was selected to represent non-linear hardening effects

$$\begin{aligned}
 f(\sigma_{ij}) = & a_{11}\sigma_{11}^2 + a_{22}\sigma_{22}^2 + a_{33}\sigma_{33}^2 + 2a_{12}\sigma_{11}\sigma_{22} + \\
 & 2a_{23}\sigma_{22}\sigma_{33} + 2a_{13}\sigma_{11}\sigma_{33} + 2a_{44}\sigma_{23}^2 + \\
 & 2a_{55}\sigma_{31}^2 + 2a_{66}\sigma_{12}^2 = k
 \end{aligned} \tag{3.52}$$

The yield function is quadratic in material stress space and includes nine material constants, a_{ij} , to represent the degree of anisotropy in the material behavior. The parameter K varies with the effective inelastic strain in the material and can be used to represent hardening behavior.

After initial yielding, material behavior will be partly elastic and partly plastic. In order to derive the relationship between the plastic strain increment and the stress increment it is necessary to make a further assumption about the material behavior. The incremental plastic strains are defined as follows:

$$d\varepsilon_{ij}^p = d\lambda \frac{\partial f}{\partial \sigma_{ij}} \tag{3.53}$$

These are the Prandtl-Reuss equations, often called an associated flow rule, and state that the plastic strain increments are proportional to the stress gradient of the yield function. The proportionality constant, $d\lambda$, is known as the plastic strain-rate multiplier. Written out explicitly the plastic strain increments are given by

$$\begin{pmatrix} d\varepsilon_{11}^p \\ d\varepsilon_{22}^p \\ d\varepsilon_{33}^p \\ d\varepsilon_{23}^p \\ d\varepsilon_{31}^p \\ d\varepsilon_{12}^p \end{pmatrix} = \begin{pmatrix} 2a_{11}\sigma_{11} + 2a_{12}\sigma_{22} + 2a_{13}\sigma_{33} \\ 2a_{12}\sigma_{11} + 2a_{22}\sigma_{22} + 2a_{23}\sigma_{33} \\ 2a_{13}\sigma_{11} + 2a_{23}\sigma_{22} + 2a_{33}\sigma_{33} \\ 4a_{44}\sigma_{23} \\ 2a_{55}\sigma_{31} \\ 2a_{66}\sigma_{12} \end{pmatrix} d\lambda \quad (3.54)$$

3.4.6 Orthotropic Failure Model For The Composite Armor

For the fiber failure and matrix cracking criteria out of plane shear stresses are included. The failure initiation criteria are listed below

$$\text{11-plane} \quad e_{11f}^2 = \left(\frac{\sigma_{11}}{\sigma_{11fail}} \right)^2 + \left(\frac{\sigma_{12}}{\sigma_{12fail}} \right)^2 + \left(\frac{\sigma_{31}}{\sigma_{31fail}} \right)^2 \geq 1 \quad (3.55a)$$

$$\text{22-plane} \quad e_{22f}^2 = \left(\frac{\sigma_{22}}{\sigma_{22fail}} \right)^2 + \left(\frac{\sigma_{12}}{\sigma_{12fail}} \right)^2 + \left(\frac{\sigma_{23}}{\sigma_{23fail}} \right)^2 \geq 1 \quad (3.55b)$$

$$\text{33-plane} \quad e_{33f}^2 = \left(\frac{\sigma_{33}}{\sigma_{33fail}} \right)^2 + \left(\frac{\sigma_{23}}{\sigma_{23fail}} \right)^2 + \left(\frac{\sigma_{31}}{\sigma_{31fail}} \right)^2 \geq 1 \quad (3.55c)$$

Failure is initiated when the stress reaches the value required for failure σ_{fail} . At this point the crack strain, ε_{cr} , is zero. A linear softening slope is assumed and therefore the ultimate crack strain, ε^u , the strain at which tensile stresses can no longer be sustained, is calculated as:

$$\varepsilon^u = \frac{2G_f}{\sigma_{fail}L} \quad (3.56)$$

where

G_f : fracture energy,

σ_{fail} : failure stress,

L : characteristic cell dimension in the direction of failure.

The gradient of the linear softening slope is given by:

$$h = \frac{\sigma_{fail}^2 L}{2G_f} \quad (3.57)$$

In Figure 3.14, the area under the softening portion of the stress/strain curve is related to G_f , which is a material property.

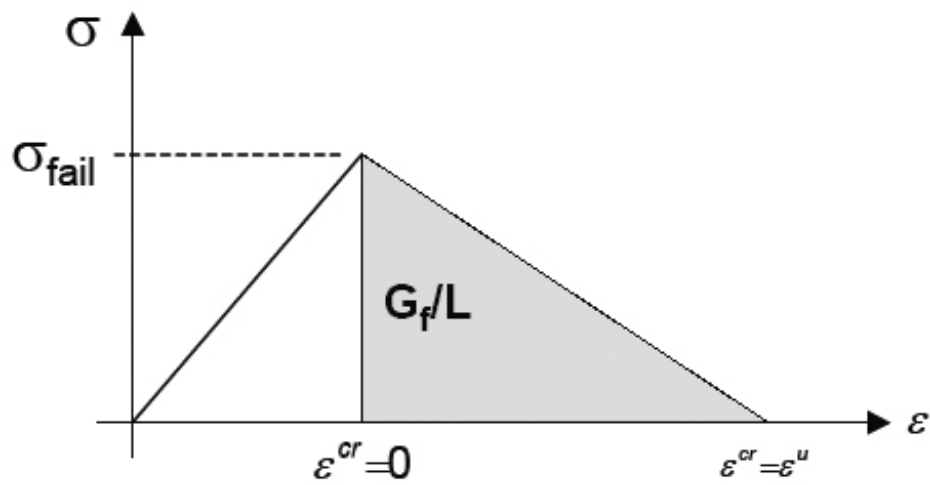


Figure 3.14 Schematic illustration of crack softening algorithm [71].

3.5 Validation of Material Models

3.5.1 Validation of Ceramic Model

The ceramic layer (front plate) of composite armor shall be of silicon carbide (SiC). As the reference for the validation of SiC model, the study of Straßburger et al.[72] shall be used. In this study, thin ceramic plate of silicon carbide is impacted by a blunt cylindrical projectile. The plate is of the dimensions 100 mm x 100 mm x 10 mm. The steel projectile has a diameter of 30 mm and a length of 23 mm. The objective of this study was to obtain damage/failure velocities in the thin ceramic target.

The model created in Ansys-Autodyn is shown in Figure 3.15. In order to save computation time, the planar symmetry conditions in a quarter model is used, i.e. $x=0$ and $y=0$ planes are used as planes of symmetry.

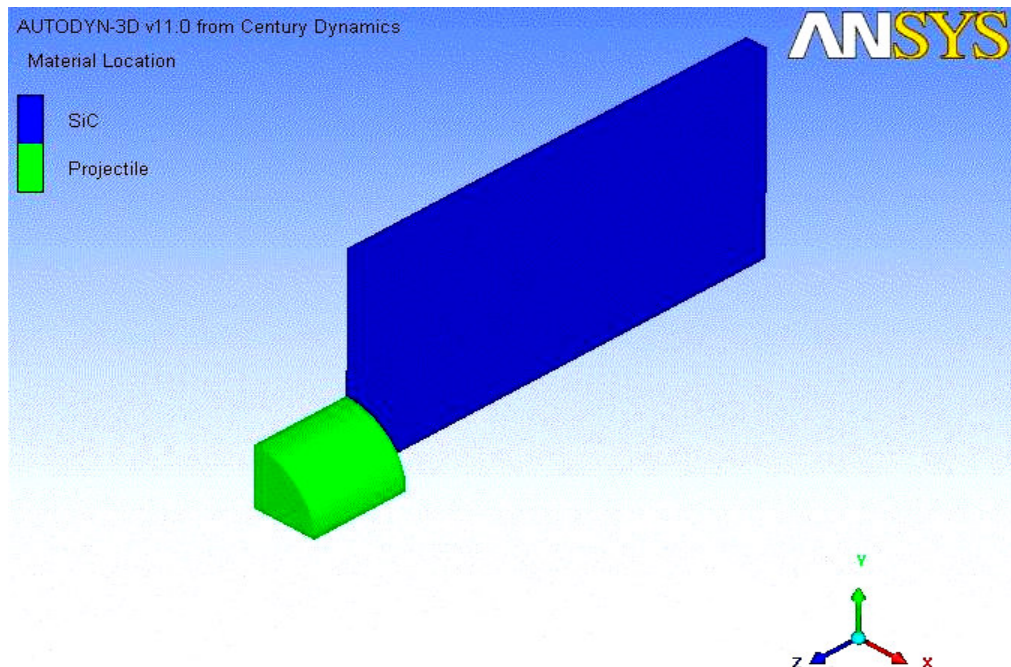


Figure 3.15 Edge-on impact (quarter) model.

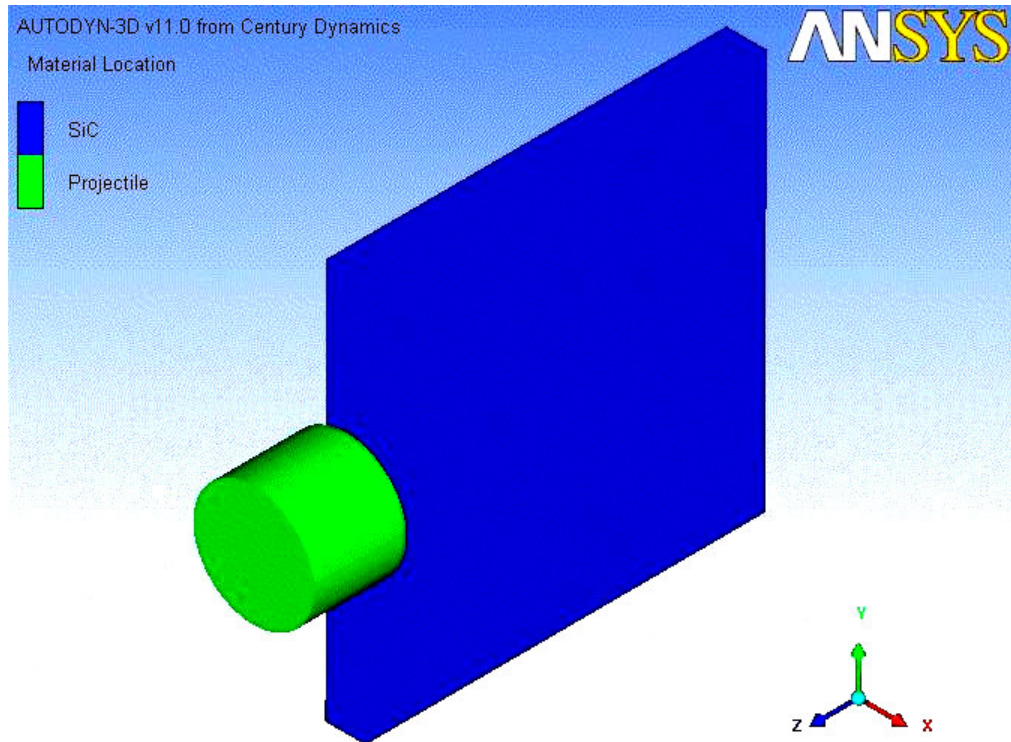


Figure 3.16 Edge-on impact (full) model.

As a start point the ceramic plate is meshed with 98,000 8-noded brick elements. The impact area is meshed with elements having a side length of 0.5 mm. The mesh is made coarser to the outer rim of the target (in the positive y -direction) and to the non-impact zone (in the negative z -direction). Computations with this model did not yield satisfactory results. Then, the ceramic plate is modeled by using 225,000 8-noded brick elements. The impact area is meshed with elements having a side length of 0.3 mm. The mesh is made coarser to the outer rim of the target (in the positive y -direction) and to the non-impact zone (in the negative z -direction). The projectile is meshed with 59,840 8-noded brick elements. Again, mesh intensity is decreased to the non-impact zone (in the positive z -direction).

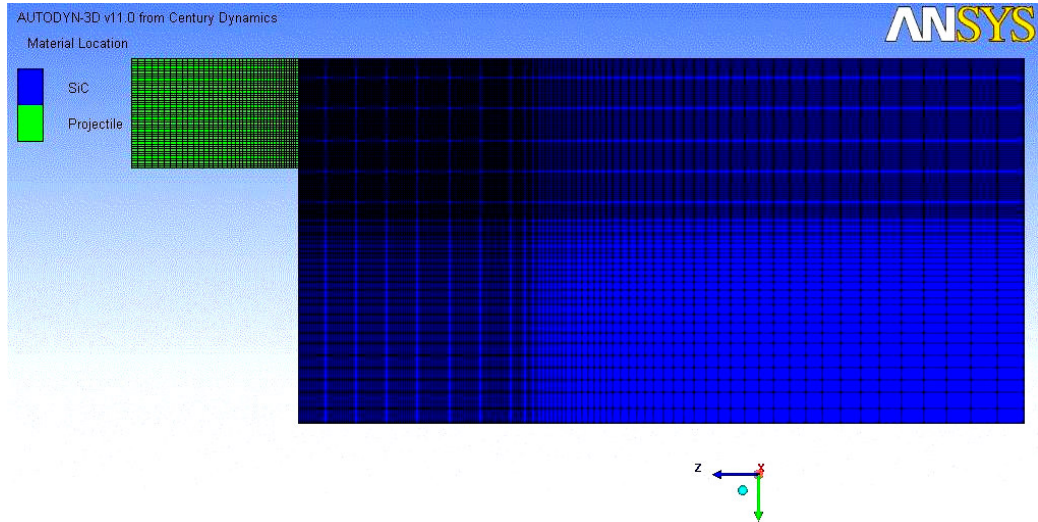


Figure 3.17 Meshed (quarter) model.

The boundary conditions on the ceramic plate are applied in such a way that upper and lower faces of the plate are firmly clamped.

The material constants for silicon carbide and steel projectile (4340 steel is assumed) used in the computations are given in Table 3.1 and Table 3.2 respectively.

Table 3.1 Material properties and constants for SiC [73]

SiC	
Density (g/cm^3)	3.215
Equation of State Data (Linear)	
Bulk Modulus- A_1 (GPa)	220.0
Strength Data	
Shear Modulus (GPa)	193.0
Hugoniot Elastic Limit-HEL (GPa)	11.7
Intact Strength Constant- S_1 (GPa)	7.1
Intact Strength Constant- P_1 (GPa)	2.5
Intact Strength Constant- S_2 (GPa)	12.2
Intact Strength Constant- P_2 (GPa)	10.0
Strain Rate Constant- C	0.009
Max. Fracture Strength- S_{fmax} (GPa)	1.3
Failed Strength Constant- α	0.40
Failure Data	
Hydro Tensile Limit- T (GPa)	-0.75
Damage Constant- E_{fmax}	1.2
Damage Constant- P_3 (GPa)	99.75
Bulking Constant- β	1.0

Table 3.2 Material properties and constants for 4340 steel [74]

4340 Steel	
Density (g/cm^3)	7.850
Equation of State Data (Linear)	
Bulk Modulus- A_1 (GPa)	164.0
Strength Data	
Shear Modulus (GPa)	78.0
Yield Stress- A (GPa)	0.91
Hardening Constant- B (GPa)	0.586
Hardening Exponent- n	0.26
Strain Rate Constant- C	0.014
Thermal Softening Exponent- m	1.03
Failure Data	
Damage Constant- D_1	-0.8
Damage Constant- D_2	2.1
Damage Constant- D_3	-0.5
Damage Constant- D_4	0.002
Damage Constant- D_5	0.61

In both of the materials linear equation of state (EOS) is used, i.e. there is a linear relation between the bulk modulus and the volumetric strain. In order to have a non-linear relation between these quantities (using e.g. a Mie-Gruneisen type of EOS which is much used), both the pressures and the impact velocities need to be higher. A much used rule-of-thumb is that if the impact velocity is less than 2000 m/s a non-linear EOS is unnecessary. For higher impact velocities a non-linear EOS should be used [75].

Three numerical analyzes are performed and the initial velocity of the steel projectile is varied as 400 m/s, 700 m/s, 900 m/s, respectively.

For the experimental data, Straßburger et al. obtained the damage/failure velocities using a Cranz-Schardin camera. For the computed results herein, the damage/failure velocity is based on the leading edge of the damaged region at times of 4.0 and 6.0 μs . The experimental and computed results are summarized in Figure 3.18 and the damage plots at 4.0 and 6.0 μs for velocities 400 m/s, 700 m/s and 900 m/s are given in Figure 3.19-3.24.

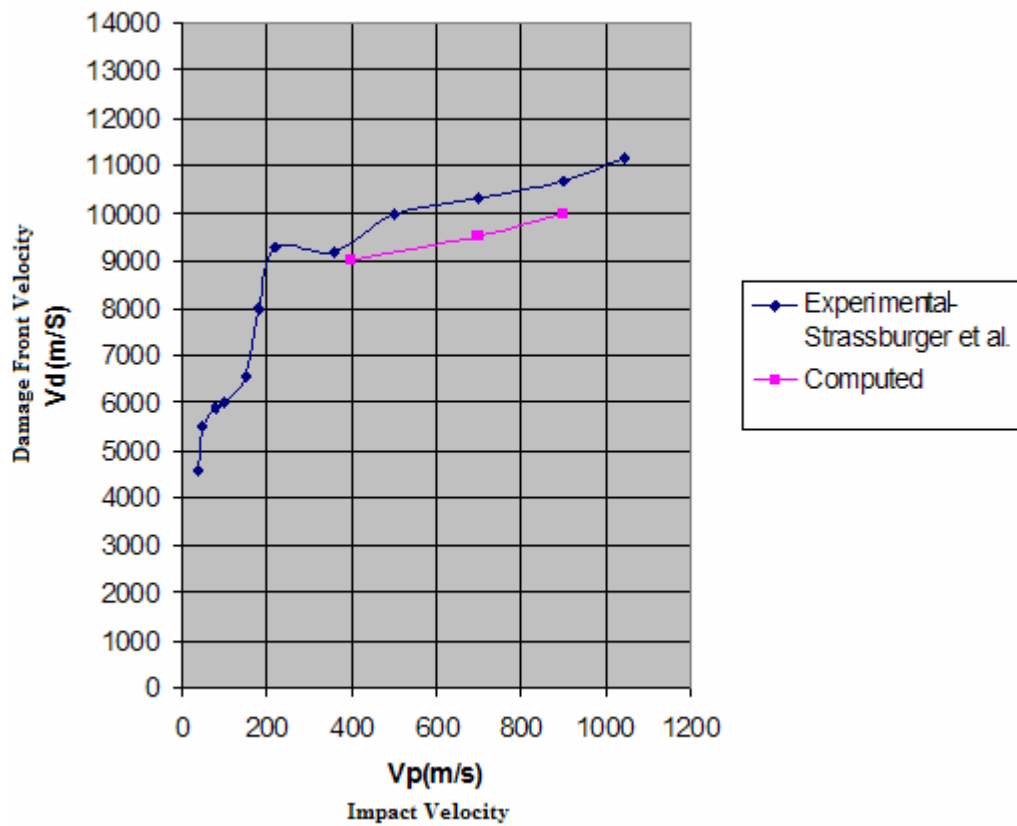


Figure 3.18 Damage velocity versus impact velocity [72].

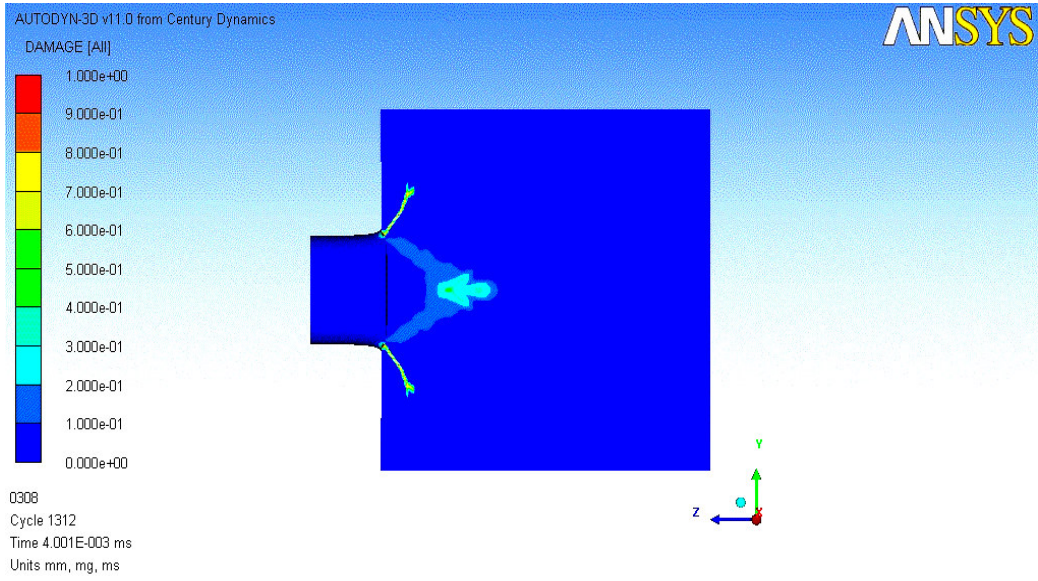


Figure 3.19 Damage plot for initial velocity of 400 m/s at 4.0 μ s.

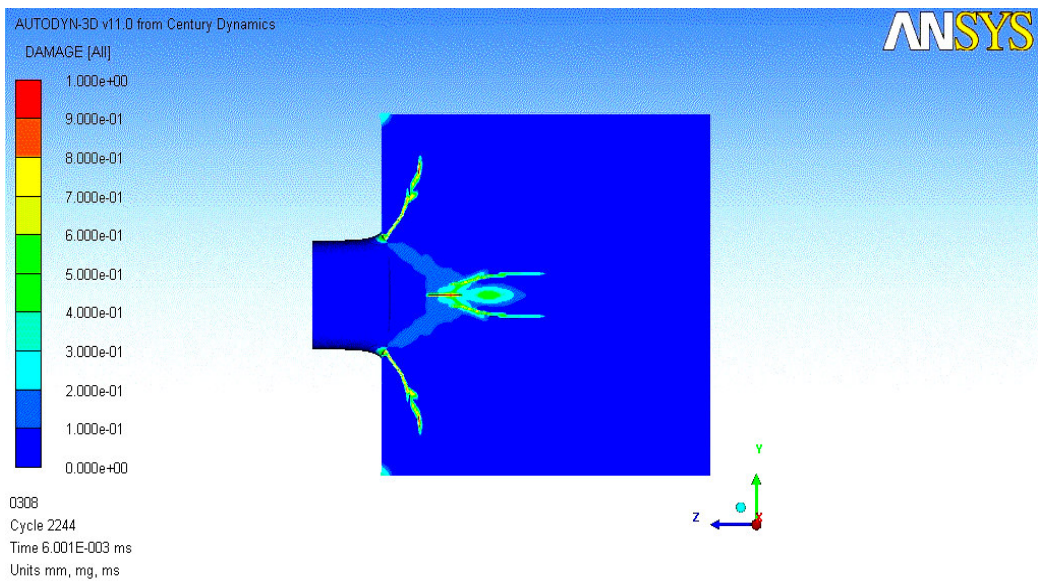


Figure 3.20 Damage plot for initial velocity of 400 m/s at 6.0 μ s.

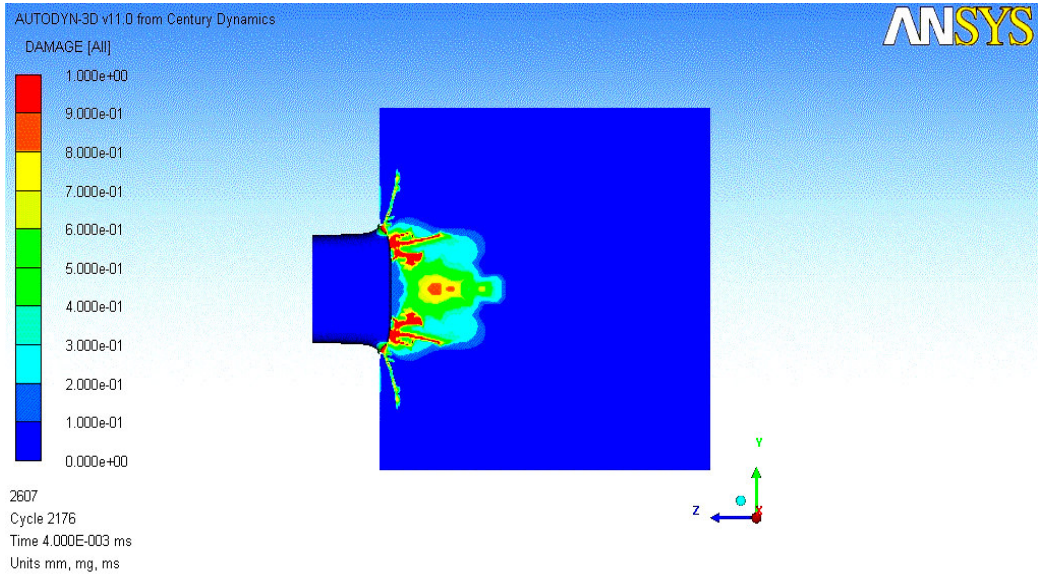


Figure 3.21 Damage plot for initial velocity of 700 m/s at 4.0 μ s.

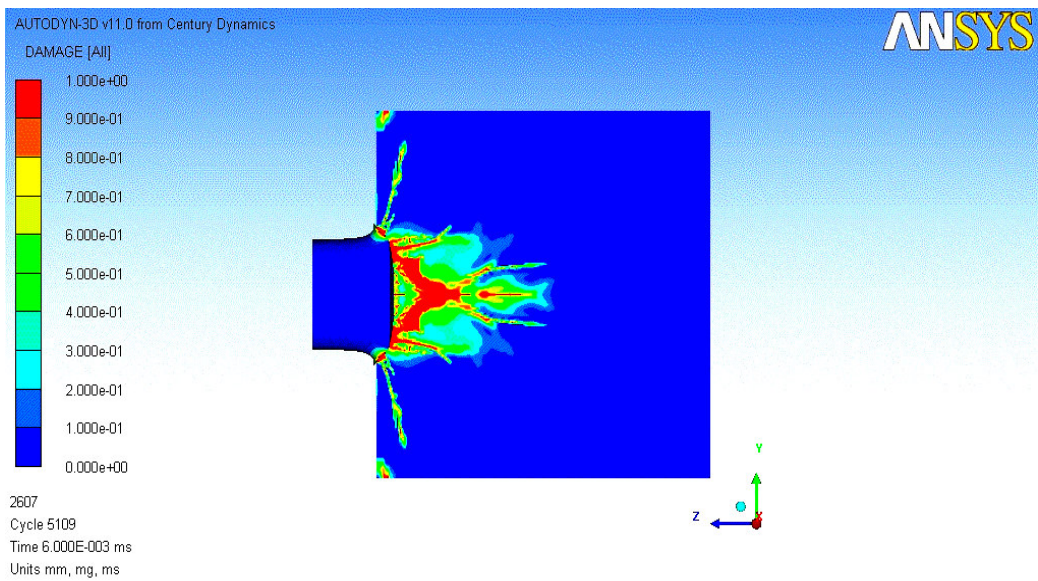


Figure 3.22 Damage plot for initial velocity of 700 m/s at 6.0 μ s.

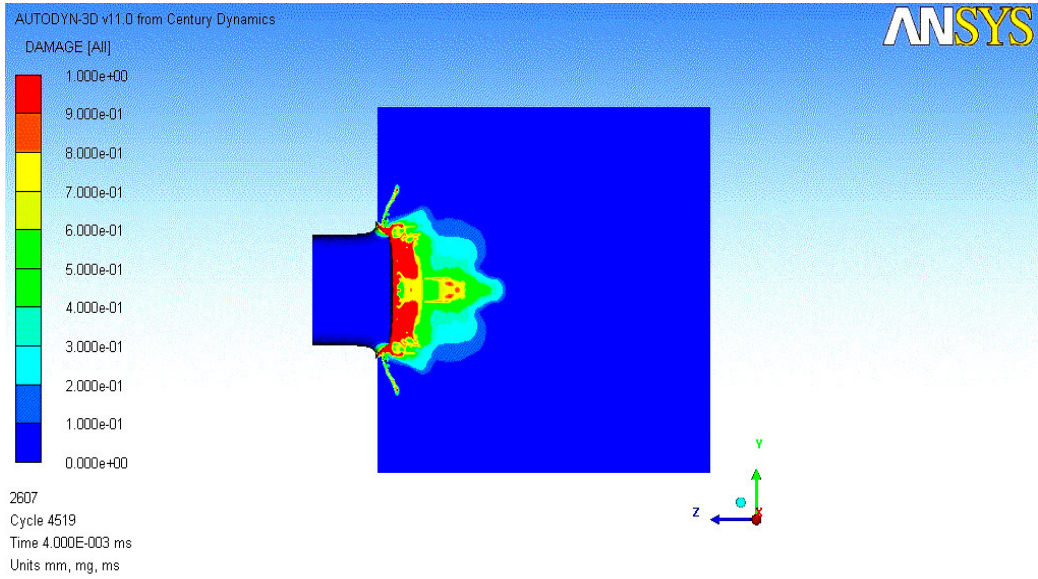


Figure 3.23 Damage plot for initial velocity of 900 m/s at 4.0 μ s.

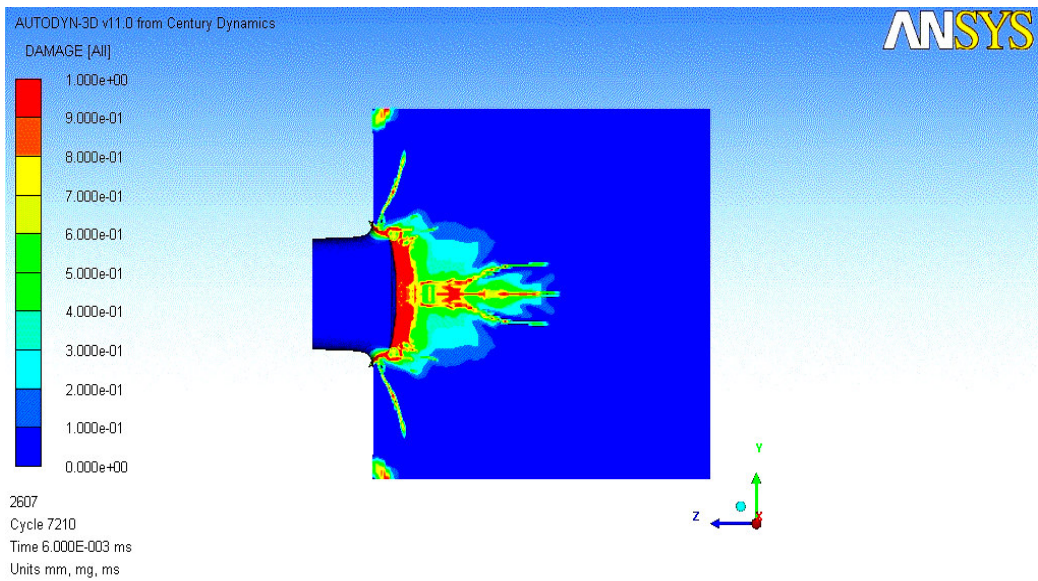


Figure 3.24 Damage plot for initial velocity of 900 m/s at 6.0 μ s.

In the computations, the initial velocity of the projectile is chosen as 400 m/s, 700 m/s and 900 m/s. For the first computation, i.e. for the initial velocity of 400 m/s, the computed damage velocity is 9000 m/s, whereas the experimentally found

damage velocity for 400 m/s projectile velocity was 9200 m/s. The percentage error here is about 2.2%. For the 700 m/s initial velocity of the projectile, the damage velocity is calculated to be 9500 m/s. In the experimental study, the damage velocity for the same velocity was found to be about 10300 m/s. The percentage error between the computational and the experimental studies is 7.7%. For the initial velocity of 900 m/s for the projectile, the damage velocity is found as 10,000 m/s. In the study of Straßburger et al., the damage velocity for 900 m/s projectile velocity was happened to be nearly 10,700 m/s. The percentage error between the computational and the experimental studies is 6.5%.

The reasons for these errors may be listed as follows:

- The steel projectile is chosen as 4340 steel. Nevertheless, Straßburger et al. did not mention any specific steel type for the projectile.
- The SiC that is used in the experiments may include some imperfections like micro voids, non-homogeneity etc.
- In the numerical analyzes, the projectile is assumed the hit the target at perfectly normal incident. But in the experiment, it is probable that perfectly normal impact conditions may have not been reached.
- There are, of course, some errors coming from the instrumentation used in the experimental setup and numerical tool used.

The damage velocity trends of the ceramic plate reported here is well correlation with the experimental results performed by Straßburger et al. This behavior of SiC shall be used in the computations in the following sections. The crack patterns, damage levels, however, could not have been validated since enough experimental data for these could not have been found in the literature; in fact there was no data available for the public use.

3.5.2 Validation of Kevlar™ Model

Material models suitable for anisotropic behavior have been developed in AUTODYN. Numerical simulations are performed by Century Dynamics Ltd. (CDL) in order to validate the developed material model. In one of these numerical simulations [76], Kevlar™ Fiber Reinforced Panel (homogeneously distributed [0/90] fiber orientation) is impacted by 1.1g steel Fragment Simulating Projectile (FSP) having an initial velocity of 483 m/s. The 4340 hardened steel is used for the projectile's material and Johnson-Cook strength model [65] is used for FSP. The results of this numerical study are compared with instrumented ballistic impact experiments carried out at TNO Prins Maurits Laboratory. The findings of the numerical study and those of the experiments are summarized in Figure 3.25 and Figure 3.26.

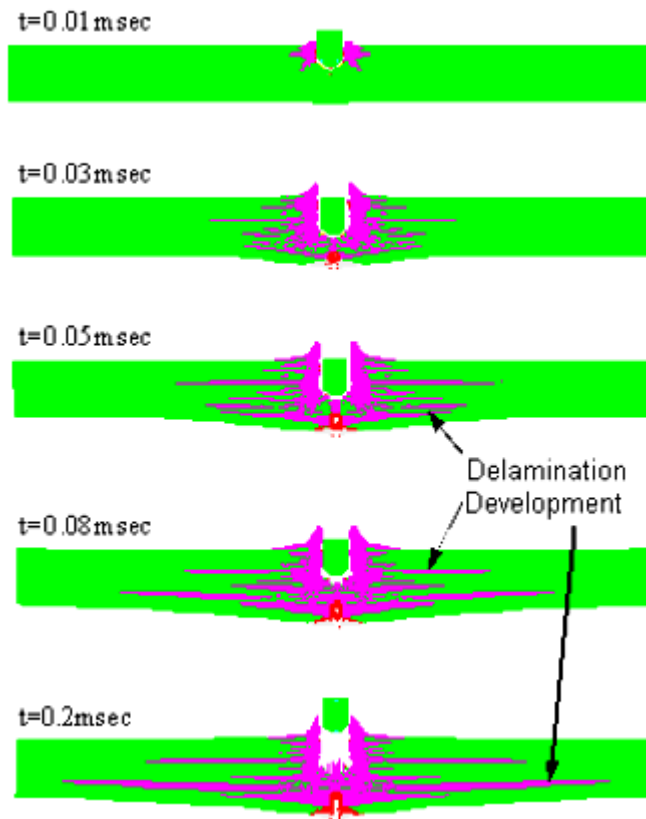


Figure 3.25 Simulated Damage Development [76].

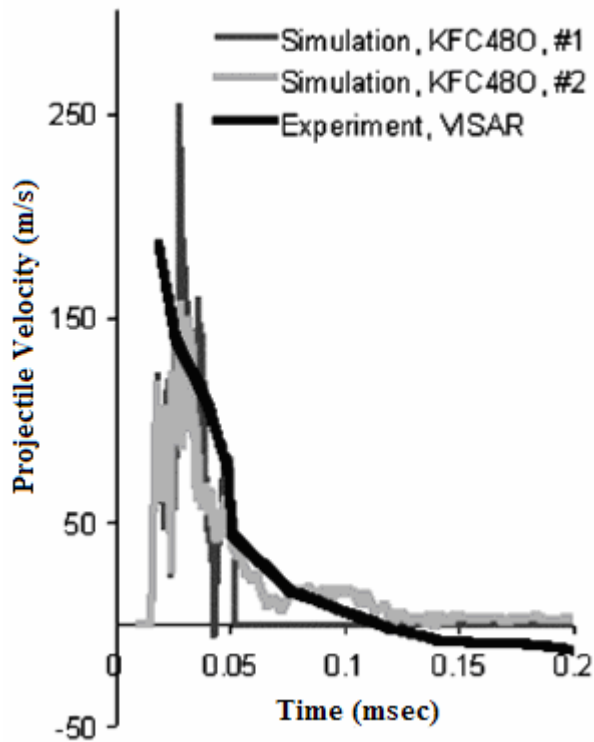


Figure 3.26 Back surface velocity [76].

From Figure 3.26, it is understood that the simulated velocity time history compares well with the experiment.

3.6 Numerical Simulations of the Advanced Composite Armor

In the simulations that will be presented, silicon carbide ceramic tile backed by KevlarTM fiber composite is impacted by 7.62mm armor piercing (AP) projectile orthogonally. In all of the simulations the initial velocity of the projectile is 850m/s. Different backing thickness will be used to investigate the optimum ceramic/composite thickness ratio.

3.6.1 Finite Element Models of the Armor System and the Projectile

The silicon carbide tile and the Kevlar™ backing are selected to be 100x100mm and the silicon carbide has a thickness of 8mm. The thickness of Kevlar™ backing is varied as 2mm, 4mm, 6mm and 8mm. The symmetry condition (about $y=0$ plane) is benefited for the complete model in order to reduce the computation time for the simulations.

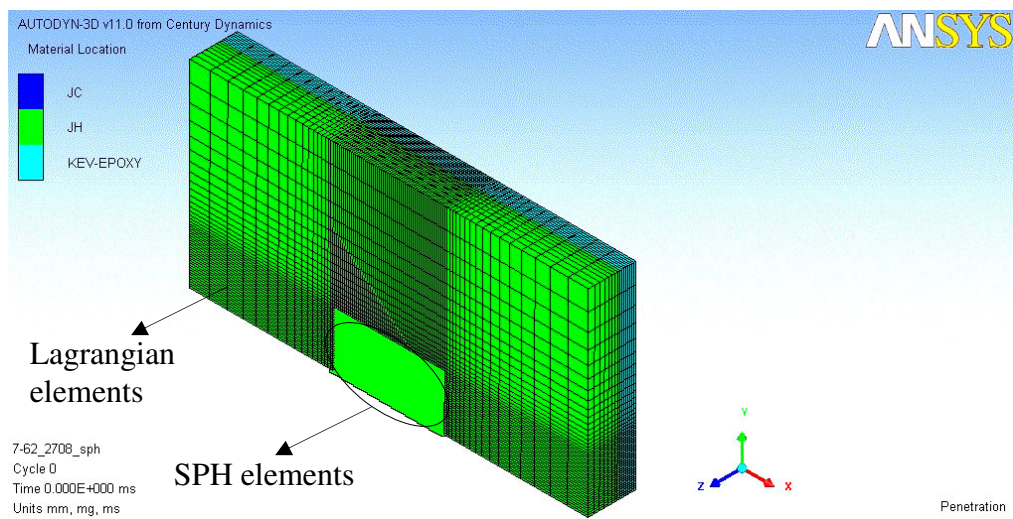


Figure 3.27 Finite element model (half model) of the composite armor system

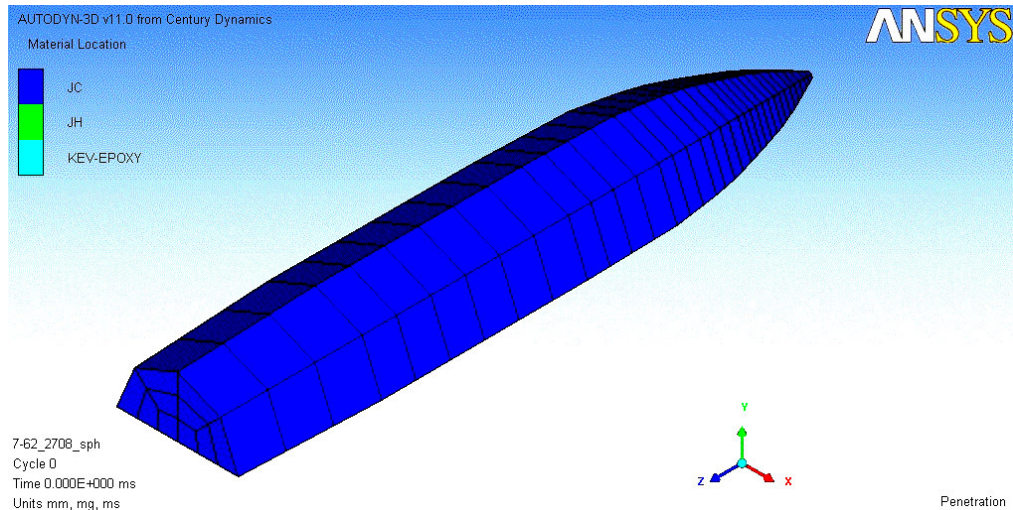


Figure 3.28 Finite element model (half model) of the projectile

The projectile model is comprised of total 11 parts. There are 340 brick elements (in the half model) used for the projectile. The projectile model is meshed in such a way that the elements are made finer to the tip of the projectile. The half model for the projectile is shown in Figure 3.28.

The silicon carbide ceramic tile is modeled both with Lagrangian and SPH elements. The center of the ceramic tile (a volume of 28x14x8mm in the half model) is modeled using 28,101 SPH elements of size 0.5mm. The reason for using SPH elements is that it enables to visualize main events in failure process of the ceramic tile like shattering of the ceramic tile and simulating the rejected ceramic particles through the analysis. The rest of the ceramic tile is modeled by 19,856 Lagrangian elements. The elements are made coarser to the outer rim of the ceramic tile. The interaction between the SPH elements and Lagrangian elements is handled automatically by the Autodyn program [63].

The KevlarTM composite backing plate is modeled by using Lagrangian brick elements. The elements are made coarser to the outer rim of the KevlarTM composite. The number of elements for different backing thicknesses is given in Table 3.3.

Table 3.3 Number of elements for backing plates

Configuration name	Thickness of the backing plate (mm)	Number of elements
C1	2	16,200
C2	4	32,400
C3	6	48,600
C4	8	64,800

The projectile is modeled by Johnson-Cook [65, 66] strength and failure model. Johnson-Holmquist strength and failure model is used for the silicon carbide tile. Finally Kevlar™ backing plate is modeled by using the available Autodyn library data. Since the fiber orientation is unidirectional (homogeneously distributed [0/90] fibers), the principal material direction is coincident with the fiber directions with the through thickness direction being the 3rd principal direction.

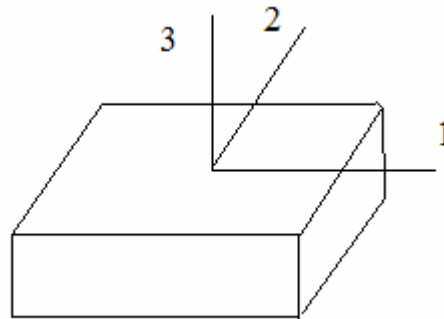


Figure 3.29 Principal material directions for the composite

The material properties and constants for the projectile and for the silicon carbide were given in Table 3.1 and Table 3.2, respectively. The material constants for Kevlar™ plate is given in Table 3.4.

Table 3.4 Material properties and constants for Kevlar™ plate

Kevlar™ plate	
Density (g/cm ³)	1.650
Equation of State Data (Ortho)	
Young's Modulus-11 (GPa)	13.06924
Young's Modulus-22 (GPa)	13.06924
Young's Modulus-33 (GPa)	3.248184
Poisson's ratio-12	0.062540
Poisson's ratio-23	0.077551
Poisson's ratio-31	0.312031
Strength Data	
Shear Modulus (GPa)	1.00
Failure Data	
Tensile failure strain 11	0.08
Tensile failure strain 22	0.08
Tensile failure strain 33	0.01

The composite armor system is assumed to be perfectly clamped around its periphery, i.e. linear and rotational velocities of the peripheral nodes are bounded to be zero.

Boundary conditions about the symmetry plane are not defined by the user since the program automatically accounts for symmetry boundary conditions once the symmetry plane (or axis) is defined. In words, translational motion has no component normal to a plane of symmetry and rotational vectors have no component in a symmetry plane.

By its nature, very large deformations are involved in the impact events. But, the highly distorted elements have to be removed from the finite element model since the accuracy of the integration is heavily depended on the level of zonal deformation. Removal of the highly distorted elements is termed as *erosion*

technique. The erosion is a numerical procedure allowing the automatic deletion of the highly distorted elements from the finite element model. Degenerate projectile elements are allowed to erode at an instantaneous geometric strain of 1.5 while heavily distorted silicon carbide tile elements are eroded at an instantaneous geometric strain of 1.0. The erosion strain for the KevlarTM plate elements is defined to be 2.5.

3.6.2 Numerical Results

The numerical simulations are performed by changing the backing thickness. All of the analyses are continued until the termination time, which is 100 μ s, is reached. Each simulation has lasted about 72 hours with a laptop equipped with Intel Core2 Duo T7200 (2.0 GHz) processor and has a 2.0 GB of RAM. Various results for different configurations of the composite armor system are presented below.

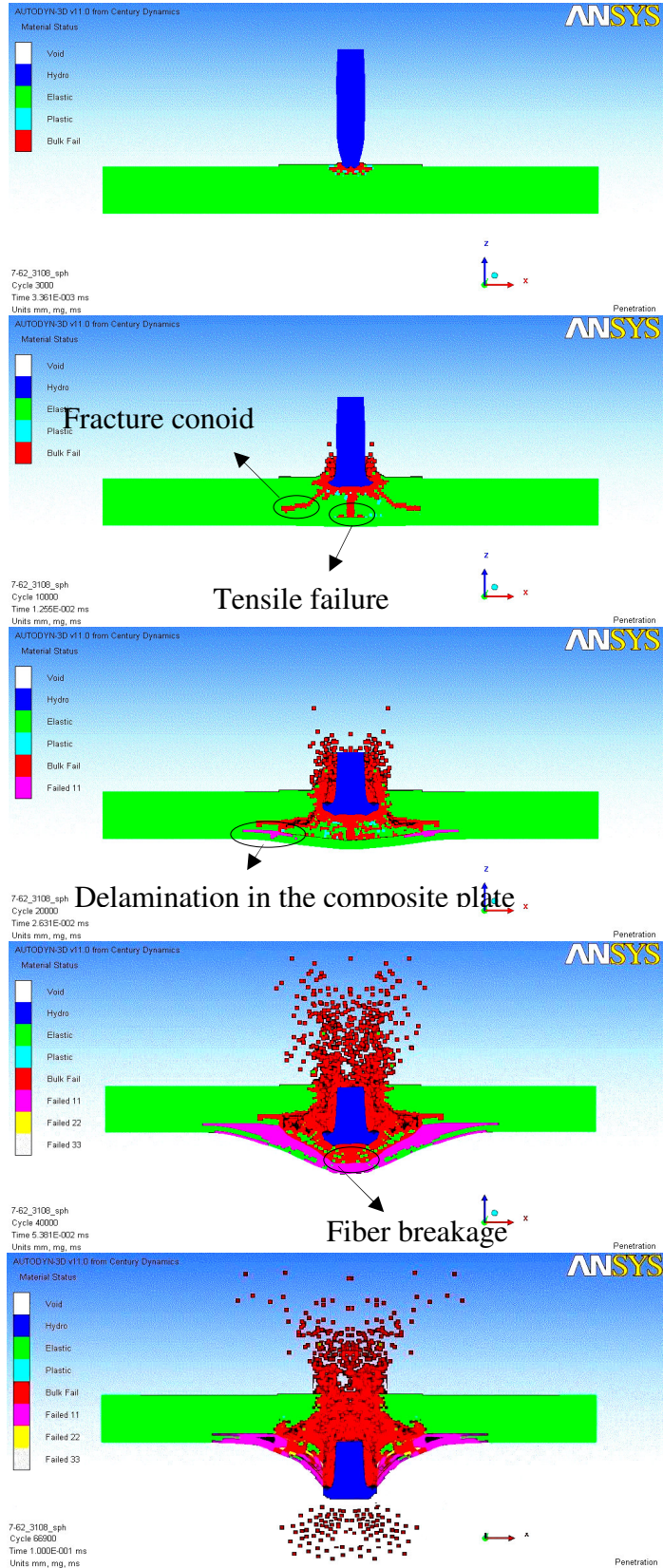


Figure 3.30 Progress of the damage for configuration C1

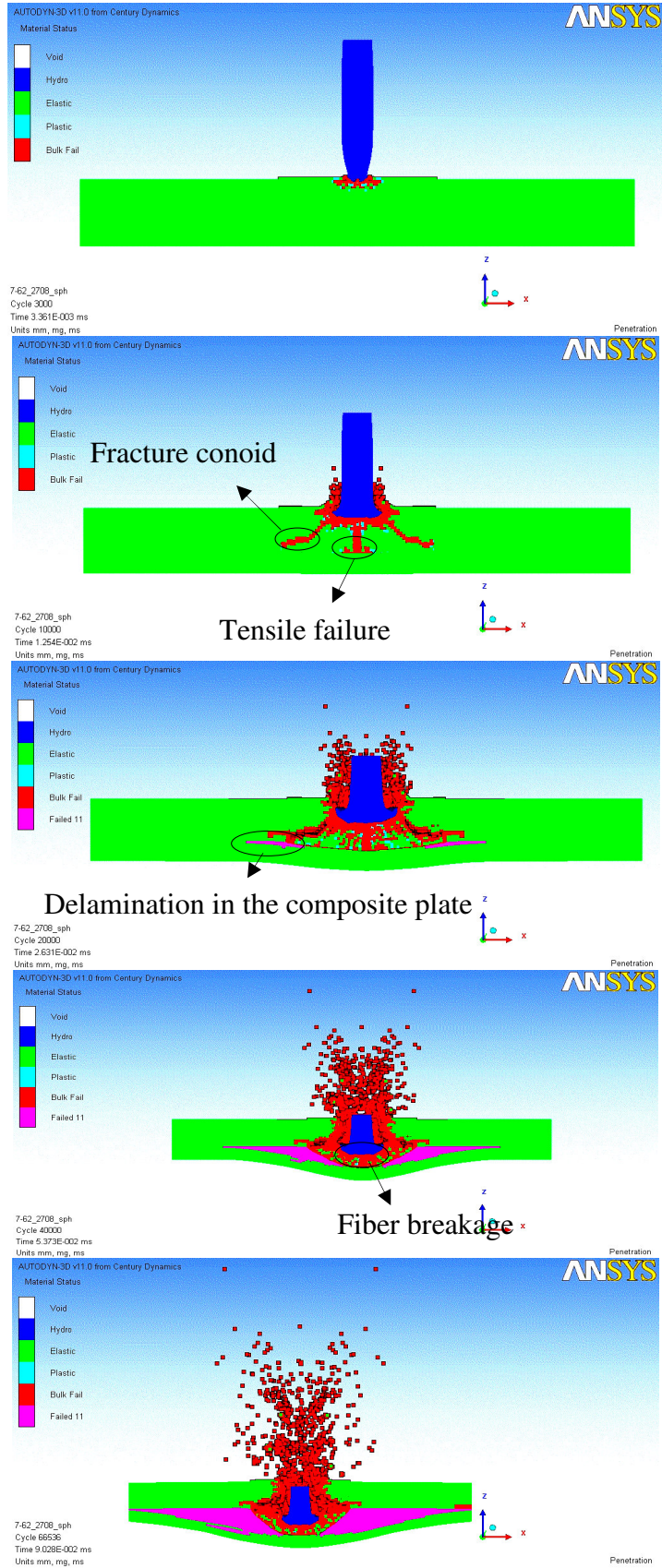


Figure 3.31 Progress of the damage for configuration C2

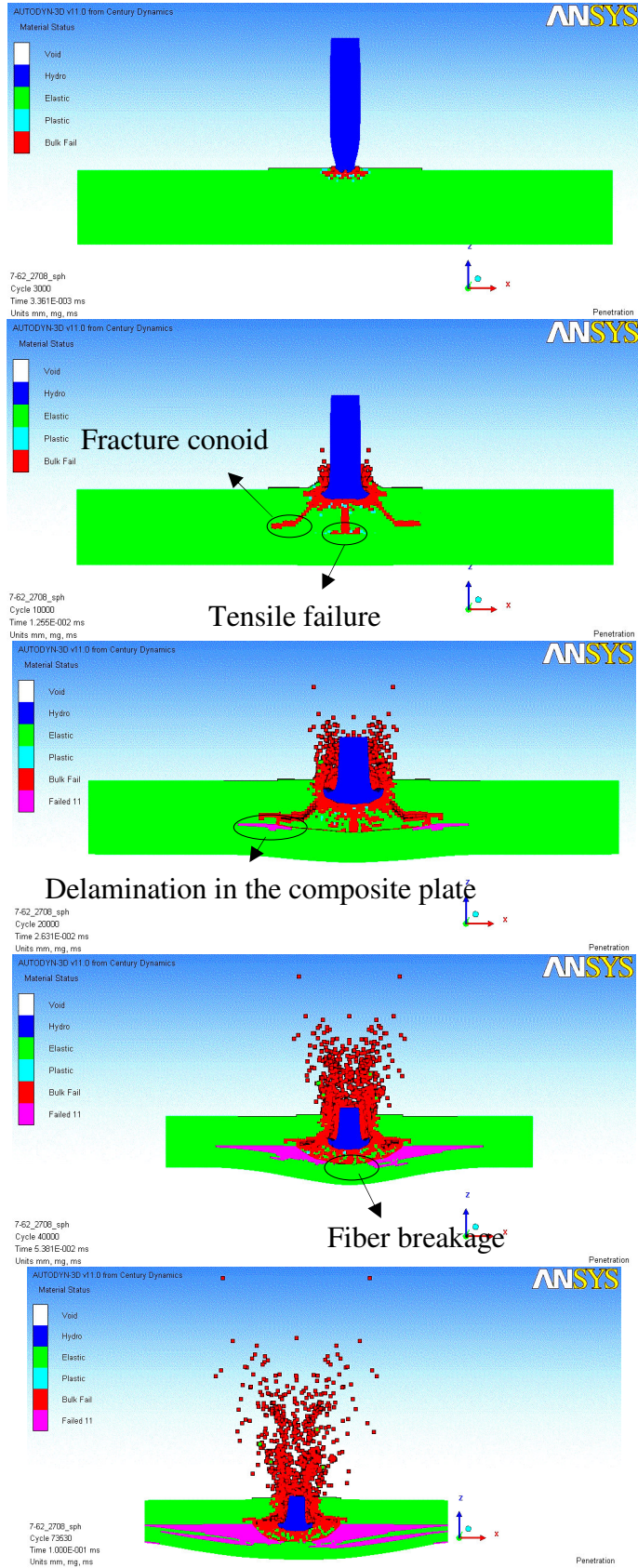


Figure 3.32 Progress of the damage for configuration C3

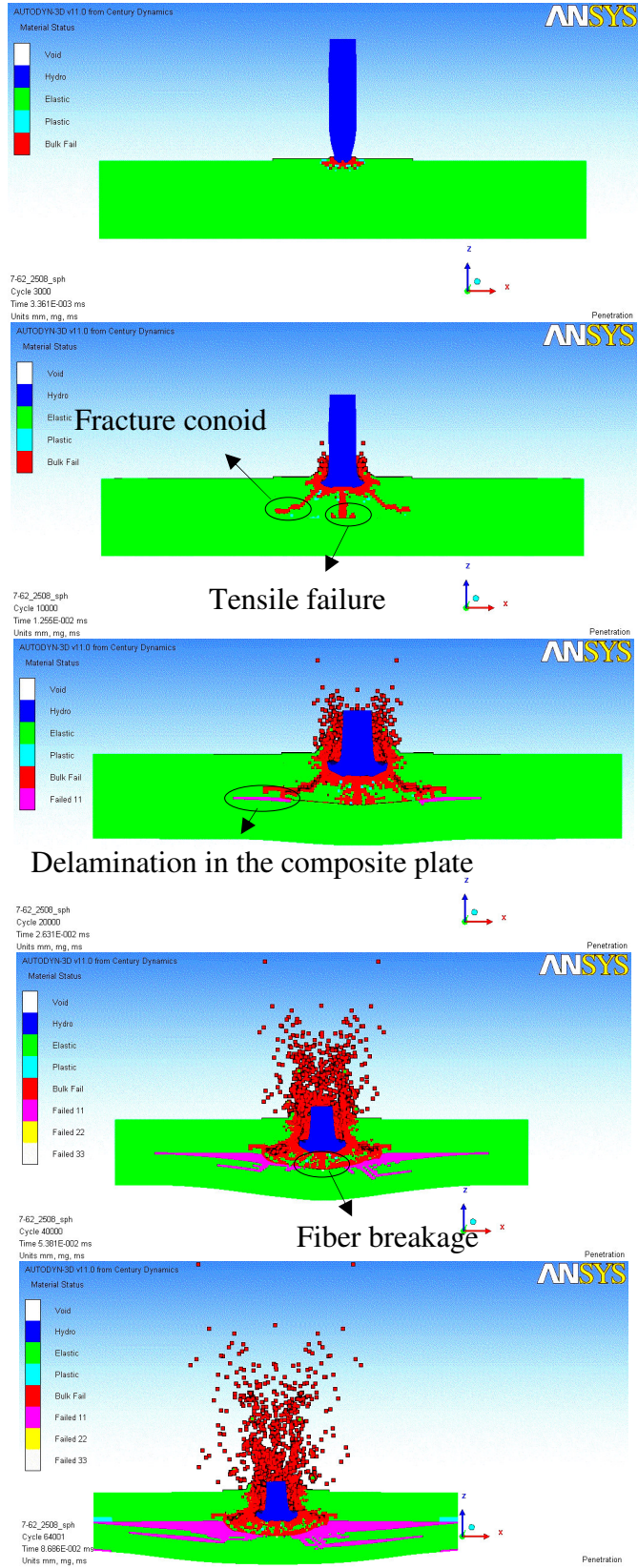


Figure 3.33 Progress of the damage for configuration C4

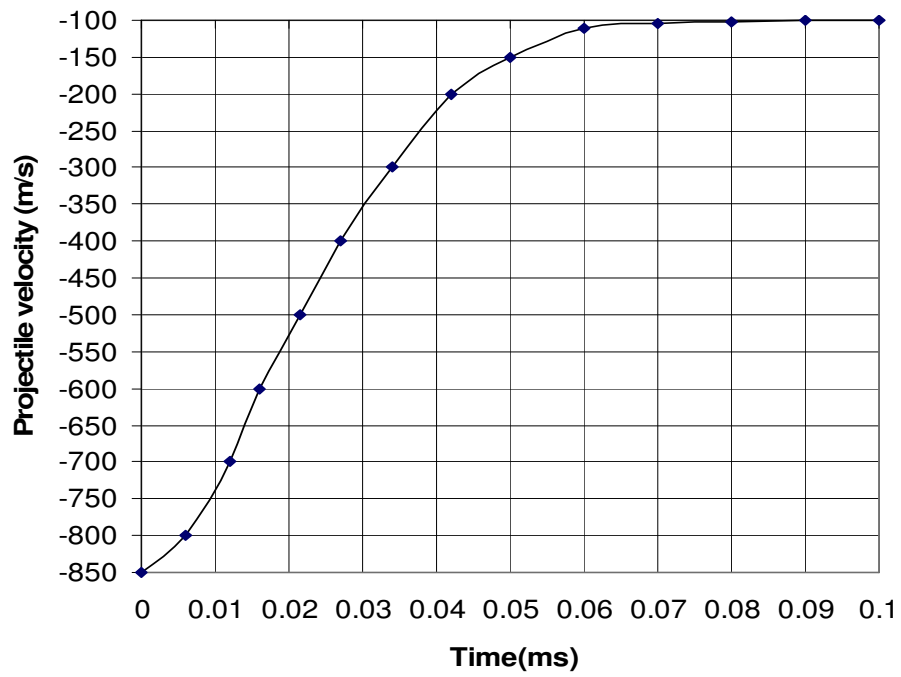


Figure 3.34 Velocity history of the projectile for configuration C1

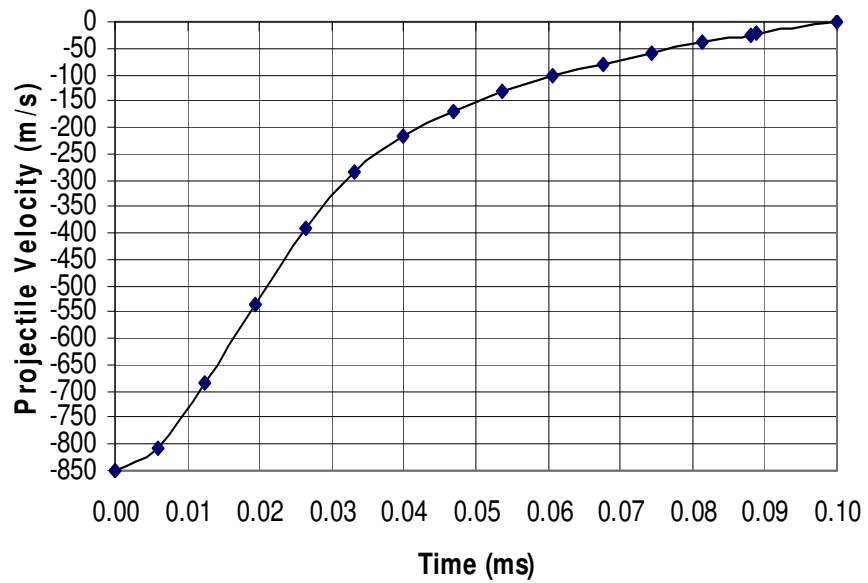


Figure 3.35 Velocity history of the projectile for configuration C2

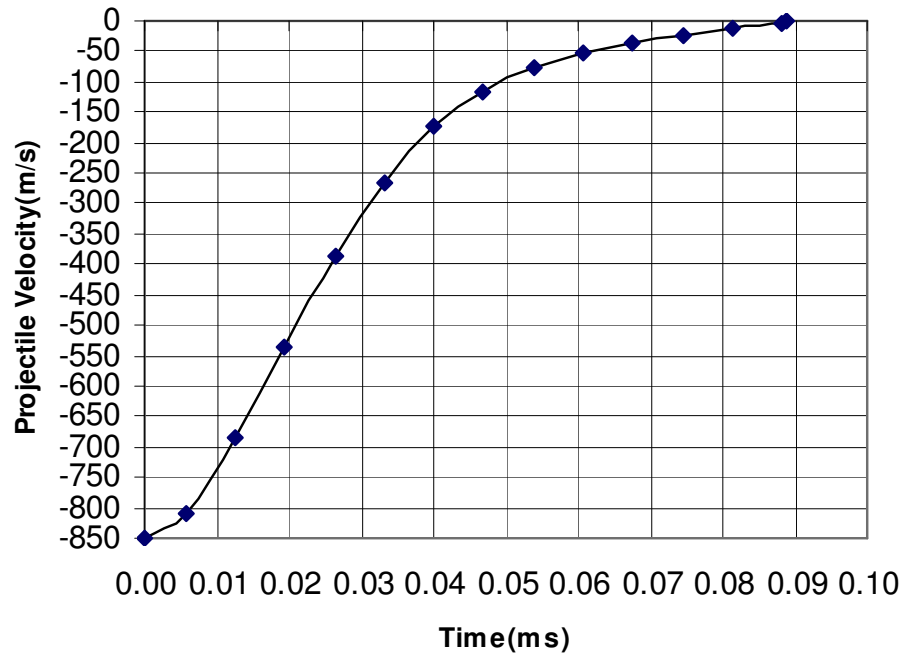


Figure 3.36 Velocity history of the projectile for configuration C3

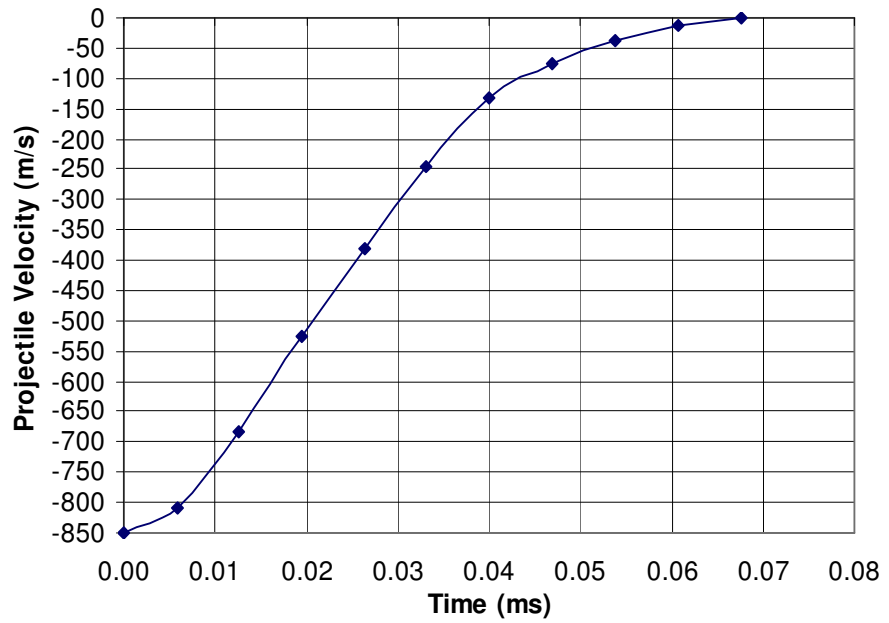


Figure 3.37 Velocity history of the projectile for configuration C4

In all of the configurations through C1-C4, crack initiations in the ceramic tile are observed at the early stages of the analysis, i.e. at time 3.36 μ s. This situation is an expected behavior of the silicon carbide which is highly brittle. Moreover, the projectile tip is defeated and it becomes nearly blunt at the interface of the ceramic tile. No clear difference is observed between different configurations of the armor system.

At time 12.5 μ s, the fracture conoid formation starts to develop in all of the configurations. The formation of conoid distributes the load over a larger area causing smaller stresses on the composite plate. There is also tensile failure of the silicon carbide at the ceramic/composite interface. Ceramic materials are weak in tension (but very strong under compression) and tensile waves at the ceramic/composite interface cause ceramic tile to fail.

The projectile penetrates further (at time 26.3 μ s) and fracture conoid becomes clearer for all of the configurations. After this point on, KevlarTM plate starts to fail, i.e. delaminates, which is a characteristic failure mode for fiber composite materials. The level of delamination slightly decreases as the thickness of the composite backing plate is increased. For the configuration C1, the projectile advances much more into the ceramic plate than those for the other configurations. Progressive delamination is the most desirable failure mode in high energy impact situations [81]. High shear stresses cause the delamination between the neighboring layers. In the delamination zone, advancing crack is captured and its propagation is prevented. Hence, the plate has still capacity to carry further load until the fibers in the next layer fail in tension. Energy absorbed during delamination depends on the interlaminar shear fracture energy, the length of delamination and the number of delaminations. Progressive delamination causes a ductile material behavior in the composite and significant amount of impact energy is absorbed.

The delamination of the composite backing plate progresses at nearly time 53.7 μ s. In addition to delamination, fiber breakage, which is another failure mode in fiber composite materials under impact loading, occurs in the composite plate.

The degree of delamination decreases as the thickness of the backing plate is increased.

The damage level for each configuration at the end of the simulation cycle is represented in the above figures. All of the configurations of the armor system, except that of C1, are able to stop the projectile (Figures 3.35-3.37). The configuration C1 is perforated by the projectile and the residual velocity of the projectile after perforation is happened to be about 100 m/s (Figure 3.34). The damage level on the surface of the ceramic tile is also given in the below figures.

At time $19.4\mu\text{s}$, the rear side of the ceramic plate is investigated (Figures 3.38-3.41). In all of the configurations, the rear side of the ceramic plate is failed (cracked). The degree of damage progressively decreases as the thickness of the backing plate is increased.

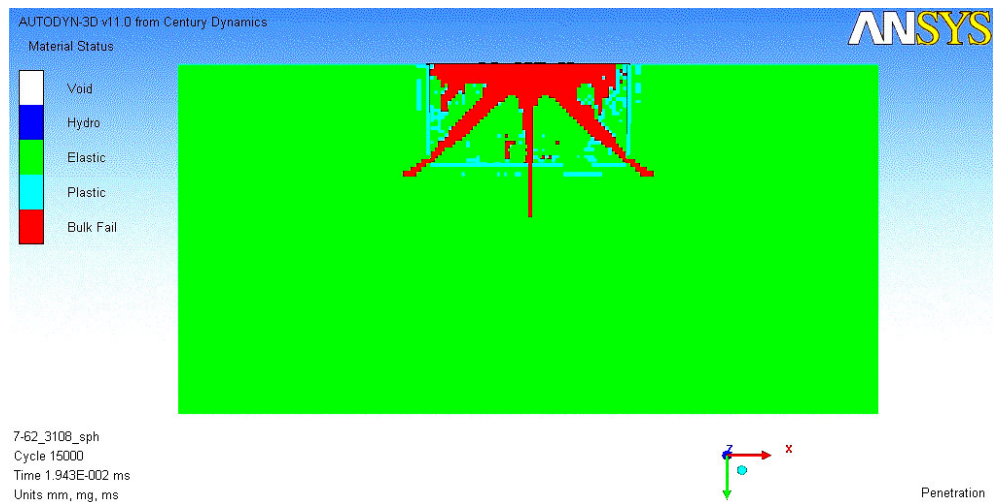


Figure 3.38 Crack propagation on the rear side of the ceramic tile for configuration C1

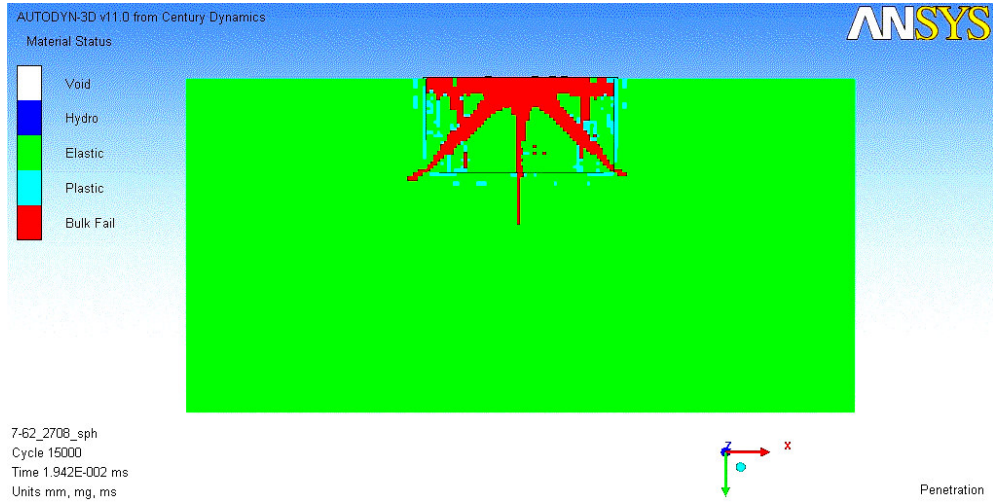


Figure 3.39 Crack propagation on the rear side of the ceramic tile for configuration C2

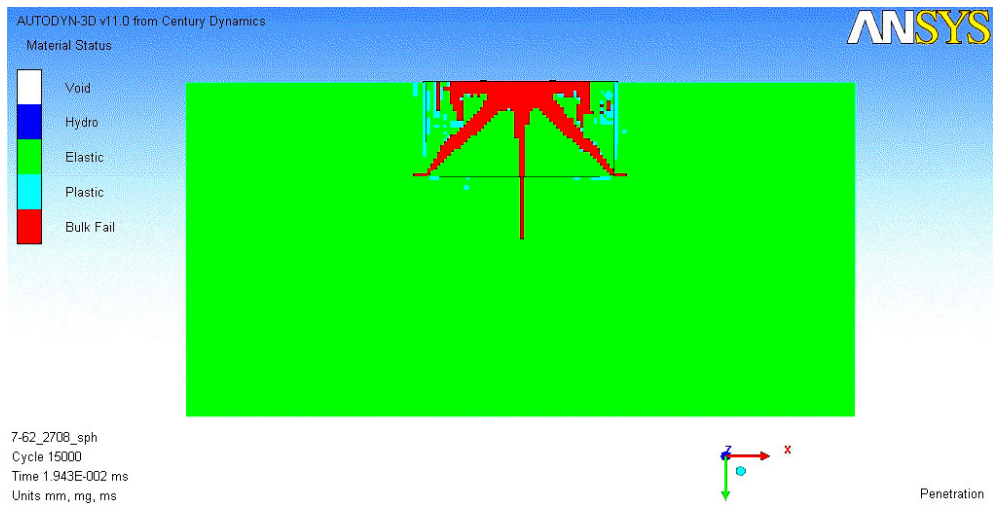


Figure 3.40 Crack propagation on the rear side of the ceramic tile for configuration C3

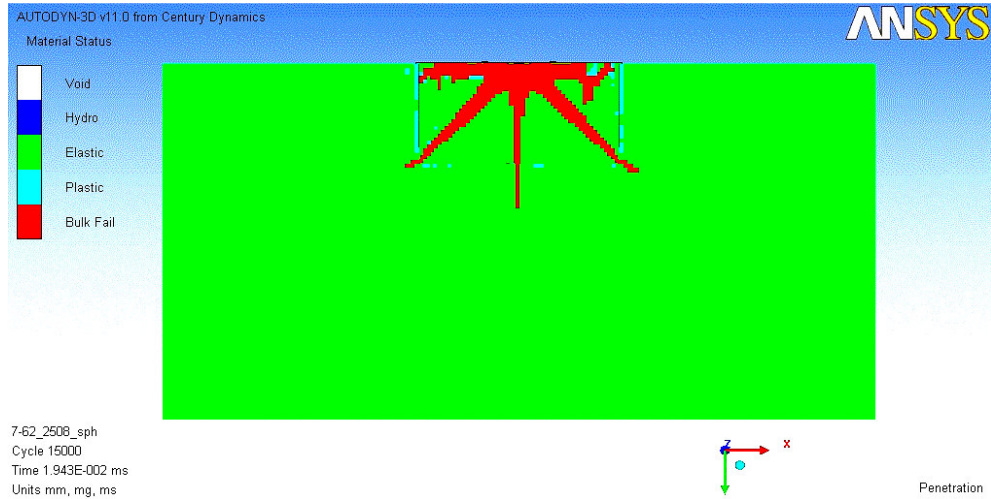


Figure 3.41 Crack propagation on the rear side of the ceramic tile for configuration C4

At the end of the simulations, the surface of the ceramic is investigated (Figures 3.42-3.45). For all of the configurations, there are random surface cracks on the ceramic surface and the level of the cracking decreases as the backing thickness increases.

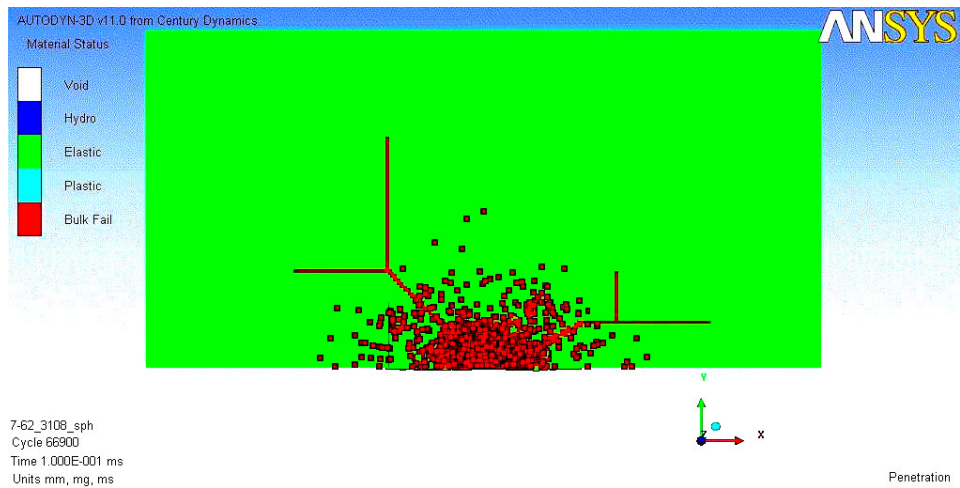


Figure 3.42 Damage level on the surface of the ceramic tile at the end of the simulation for configuration C1

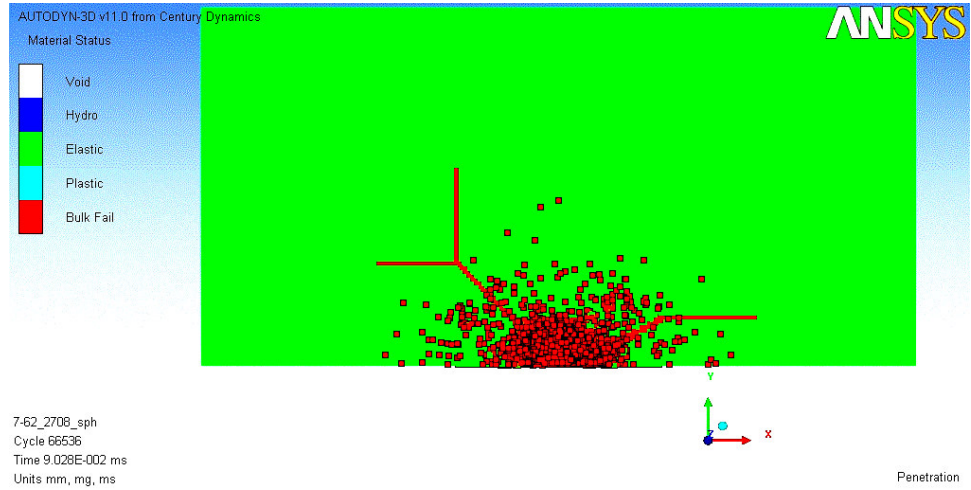


Figure 3.43 Damage level on the surface of the ceramic tile at the end of the simulation for configuration C2

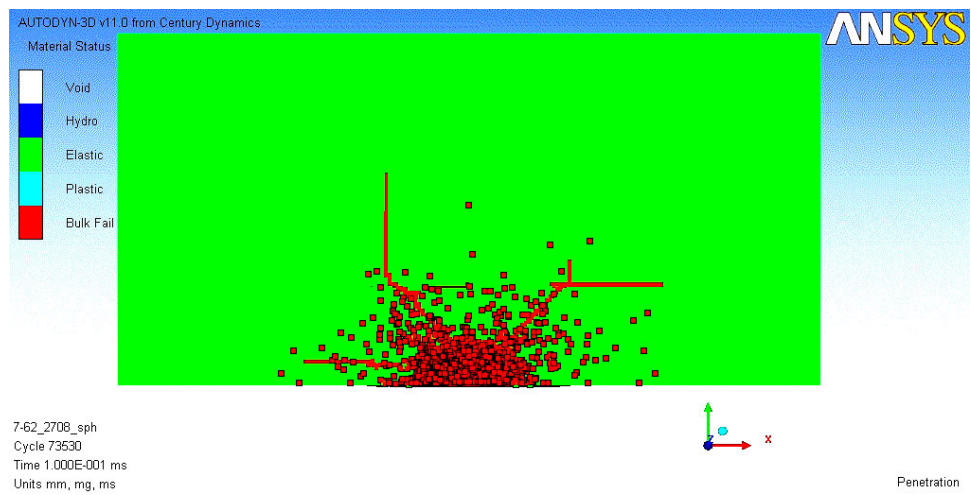


Figure 3.44 Damage level on the surface of the ceramic tile at the end of the simulation for configuration C3

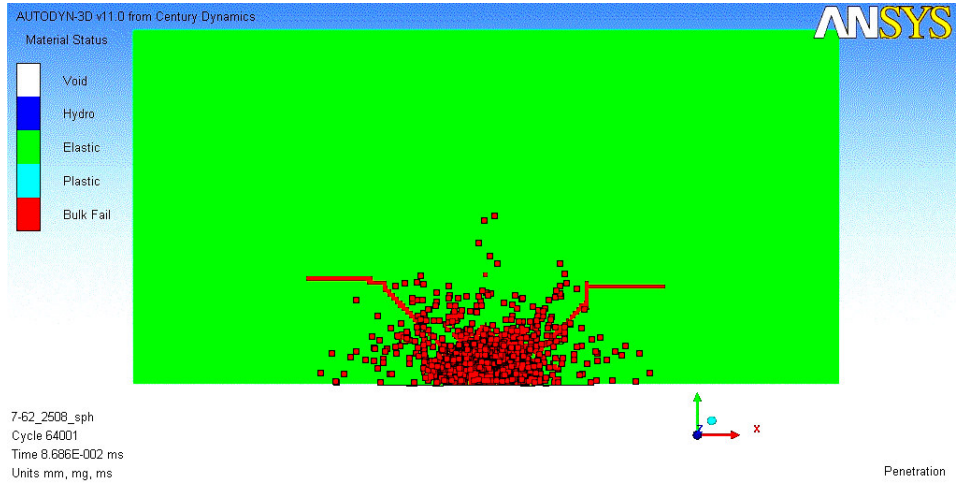


Figure 3.45 Damage level on the surface of the ceramic tile at the end of the simulation for configuration C4

CHAPTER 4

DISCUSSION AND CONCLUSION

4.1 Discussion of Results

In this study, the finite element analysis of the ballistic impact of 7.62mm.armor piercing (AP) projectile onto the silicon carbide ceramic tile backed by KevlarTM composite plate is performed by using AUTODYN hydrocode. The ceramic plate thickness is kept constant at 8mm and the backing plate thickness is gradually changed in order to find out the optimum ceramic/composite thickness ratio.

Throughout the analyses, various damage mechanisms are observed in the participating materials. To begin with the silicon carbide ceramic; being highly brittle, ceramic materials tend to shatter (or cracks) upon impact. This tendency is mostly captured in the numerical simulations. The fracture conoid formation in the silicon carbide tile is also represented in all of the simulations. However, the conoid is not very intense at the beginning of the simulations, i.e. at the time of projectile defeat on the interface of the ceramic tile. It becomes clearer as the projectile penetrates into the ceramic plate. Due to the fact that ceramic materials are very weak in tension, the tensile waves that passes through the ceramic plate can easily cause it fail (like spallation) and such phenomena is also observed in the numerical simulations. If Figures 3.30-3.37 are carefully analyzed, it is easily seen that even if the ceramic material fails under impact, it has still some degree of strength to decelerate the projectile. This fact is summarized in the material model description of the silicon carbide [67]. It is well known that some of the shattered pieces of ceramic tile disperse around and such rejection of the ceramic particles is also represented by SPH particles in the numerical simulations. It would not be possible to simulate these rejected particles by using Lagrangian elements, and this is why the local impact area zone of the silicon carbide tile is modeled by using SPH elements. The surface damage of the ceramic plate is very

limited at the end of the simulations for all configurations which is an unexpected result. The ceramic tile should shatter (or crack) thoroughly on the surface. We can conclude with this behavior that the ceramic model used in the simulations is not able to well simulate the surface crack patterns which should actually be distributed all over the surface of the ceramic tile. There is not notable difference on the damage levels of ceramic plates for different configurations. This is not surprising since the ceramic plate thickness is the same for all configurations and slight differences are most probably due to the different thickness valued backing plates.

Secondly, the projectile is analyzed. For the projectile material, 4340 hardened steel is used in the simulations. However, 7.62mm AP projectiles manufactured by MKE are made of Steel 100 Cr 6 (DIN 671). Johnson-Cook material model [65, 66] constants for this material are unavailable. For this reason, 4340 steel, which is commonly used as an AP projectile material in the literature, is used in all of the simulations. As a first notice, the projectile is defeated and its tip is made blunt by the ceramic plate. As the projectile advances in the silicon carbide, it assumes a shape like a mushroom, which is named as mushrooming [82]. The most important point that can be withdrawn from the projectile behavior lays in Figures 3.33-3.37. The projectile is mostly decelerated when it propagates in the ceramic material. These cases are consistent with the fact that the ceramic material in a composite armor system is mainly responsible for breaking the projectile tip and absorbing great amount of projectile's kinetic energy.

As for the backing material, KevlarTM, it exhibits characteristic failure modes that composite materials have like delamination and fiber breakage and these aspects are clearly observed in the numerical simulations for all different configurations of the armor system. The level of delamination increases as more and more ceramic particles in the conoid zone pushes the composite plate and when the tensile strength of the fiber is exceeded, fiber finally ruptures (fiber breakage). There is one more failure mode for composite materials which is matrix cracking. The model that is used in the simulations does not have the capability to simulate

such a failure mode. In order to be able to represent this behavior, fiber and matrix materials should be separately modeled and different material models be used for these two materials.

From the simulations presented, the effect of target thickness becomes obvious only in the configuration C1, which corresponds a backing thickness of 2mm. All of the other configurations through C2-C4 are able to stop the projectile. Hence, from these results, the optimum ceramic/composite thickness ratio could easily be found. The thickness of the ceramic plate is 8mm, and the minimum backing thickness that can stop the projectile is 4mm. As a result, the optimum thickness ratio of the ceramic to backing plate is happened to be 2.

4.2 Conclusion

In this study, it is aimed at determining the optimum thickness ratio between the ceramic and the composite material and comparing this value with the analytical result obtained for the ceramic/composite armor system in the literature. For the ceramic material, silicon carbide and for the composite material KevlarTM is selected. After the materials are selected, armor systems having different backing thickness values are analyzed by performing numerical simulations. At the end of the simulations, the optimum thickness ratio of the ceramic/composite plates is found to be about 2.

The areal densities corresponding different configurations of the armor system are represented in Table 4.1. Areal density of the armor system can be easily calculated by adding the multiplication of the density and thickness values of ceramic and composite materials.

Table 4.1 Areal densities of different configuration of the armor system

Configuration	Areal Density (kg/m ²)
C1	29.02
C2	32.32
C3	35.62
C4	38.92

From Table 4.1, it is concluded that using 2mm less thickness for the backing material saves 3.3 kg in every square meters of the armor. By performing such an analysis can greatly reduce the total weight of land vehicle or air vehicle, thus improving the vehicle' s mobility to a great extent.

The extensions of the present study can be listed as follows:

- In the simulations only the core of the AP projectile is used. The jacket and the antimon lead part of the AP projectile can also be modeled and the simulations can be performed with this projectile.
- The material constants for silicon carbide, KevlarTM and the projectile can be obtained by performing tests on these materials and simulations can be performed by using these constants.
- Firing tests can be held by using the same materials and same configuration. The results of these tests can be used to validate the numerical simulation results
- In the real case, there exists some bonding material between the armor plates. This bonding material can also be modeled and simulations can be performed.
- Multiple tiles can be added to the simulation in order to investigate the interaction between this tiles. Also some rubber materials can be used between this tiles in order to absorb shocks coming from neighboring tiles.

REFERENCES

- [1] Tytler, I.F.B., Thompson, N.H., Jones, B.E., Wormell, P.J.H., Ryley C.E.S, “Vehicles And Bridging” ,METU Library, UG446.5 V37, 1985.
- [2] Ogorkiewicz, R., “Armored Fighting Vehicles (AFV)” Seminar, UK, 2006.
- [3] Wang, B., Chou, S.M, “The Behavior of Laminated Composite Plates As Armor”, [Journal of Materials Processing Technology](#), Volume 68, Number 3, 15, pp. 279-287(9), August 1997.
- [4] Guden, M., Yildirim, U, Hall, I.W. “Effect Of Strain Rate On The Compression Behavior Of A Woven Glass Fiber/SC-15 Composite” 2003.
- [5] Silva, M. A. G, Cismaşiu C., Chiorean, C.G., “Numerical Simulation of Impact on Composite Laminates, 2003.
- [6] Smith, P. D, Hetherington, J. G, “Blast and Ballistic Loading of Structures” Butterworth-Heinemann Ltd. 1994.
- [7] Zukas, J.A., Nicholas, T., Swift, H.F., Greszczuk, L.B., Curran, D., “Impact Dynamics”, John Wiley & Sons, Inc., 1982.
- [8] Florence, A.L., “Interaction of projectiles and composite armor, Part II,” Standford Research Institute, Menlo Park, California, AMMRC-CR-69-15, 1969.
- [9] Zouheir, F., Kamran B., Yigui, X., “Optimum Design of Two-Component Composite Armors Against High-Speed Impact” [Composite Structures Volume 73, Issue 3](#), Pages 253-262, June 2006.
- [10] Z. Fawaz, W. Zheng, K. Behdinin, “Numerical Simulation of Normal and Oblique Ballistic Impact On Ceramic Composite Armors” [Composite Structures Volume 63, Issues 3-4](#), Pages 387-395, February-March 2004.
- [11] Zhou, G., Reid, S.R., “Impact Behavior of Fiber-Reinforced Composite Materials and Structures”, CRC, October 31, 2000.
- [12] Sung, H. A., Woo, K.J., Hee, J.K., “Development Trends of Ceramic Composite Armors for Combat Vehicles”, Journal of the Korean Society of Precision Engineering, Vol. 22, No. 7, July 2005.
- [13] Cristescu, N., Malvern, L.E., and Sierakowski R.L., “Failure Mechanisms in Composite Plates Impacted by Blunt-Ended Penetrators, In: Foreign Object Impact Damage to Composites Materials”, ASTM STP 568, American Society for Testing and Materials, pp. 159-172, 1975.

- [14] Wilkins, M. L., "Mechanics of Penetration and Perforation", *Int. J. of Eng. Sci.* Vol. 16. pp. 793-807, 1978.
- [15] Zheng-Dong, M., Hui, W., Yushun, C., Douglas, R., Adria, S., Donald, O., "Designing an Innovative Composite Armor System for Affordable Ballistic Protection", 25th Army Science Conference, Orlando, Florida, December 2006.
- [16] Sierakowski, R.L., Takeda, N., "An Investigation of In-Plane Failure Mechanisms in Impacted Fiber Reinforced Plates, In: *Composite Materials*", Proc. Japan-U.S. Conf., Tokyo, pp. 12-21, 1981.
- [17] Sun, C.T., Wang, T., "Impact Wave Response and Failure in Composite Laminates, In: *Mechanical Behavior of composites and lam*"; Proc. 214th European Mechanics Colloq., Kupari, Yugoslavia, 16-19 September, Elsevier Sci. Publ., 1987, pp. 19-31, 1986.
- [18] Ruiz, C., Duffin, R., "Experimental Study of Soft Body Impact at Subordnance Velocities, In: *Experimental Mechanics, Advances in Design, Testing and Analysis*", Proc. of the 11th Int. Conf. On Experimental Mechanics, Oxford, UK, Balkema, Rotterdam, 1998, pp. 143-148, 24-28 August, 1998.
- [19] Bruchey, W., Horwath, E., "System Considerations Concerning the Development of High Efficiency Ceramic Armors", 17th Int. Sym. On Ballistics, Midrand, South Africa, 1998.
- [20] Gellert, E.P., Cimpoeru, S.J., Woodward, R.L., "A Study of the Effect of Target Thickness on the Ballistic Perforation of Glass-Fiber-Reinforced Plastic Composites", *Int. J. Impact Eng.*, v. 24, pp. 445-456, 2000.
- [21] Fink, B.K., "Composite Armor: Providing Multifunctional Materials for Future Ground Vehicles",
ARL website: <http://www.arl.army.mil/wmrd/Tech/CompositeArmor-both.pdf>.
- [22] Kaufmann, C., Cronin, D., Worswick, M., Pageau, G., and Beth, A. "Influence of Material Properties on the Ballistic Performance of Ceramics for Personal Body Armour", *Shock and Vibration*, 10, 51-58, 2003.
- [23] Dechaene, R., Degrieck, J., Iannucci, L., Willows, M., "A Constitutive Model for Glass Fibre Fabric Composites under Impact", *J. Composite Materials*, v.36, n. 8, pp. 983-1004, 2002.
- [24] Fujii, K., Aoki, M., Kiuchi, N., Yasuda, E., Tanabe, Y., "Impact Perforation Behavior of CFRPs Using High-Velocity Steel Sphere", *Int. J. Impact Eng.*, v. 27, n. 5, pp. 497-508, 2002.

- [25] Hammond, R.I., Proud, W.G., Goldrein, H.T., Field, J.E., “High-resolution Optical Study of the Impact of Carbon-fiber Reinforced Polymers with Different Lay-ups”, *Int. J. Impact Eng.*, v. 30, n. 1, pp. 69-86, 2004.
- [26] Hetherington, J., “The Optimization of Two Component Composite Armour”, *International Journal of Impact Engineering*, Volume 12 No:3, pp. 409-414, 1992.
- [27] Wang, B, Lu, G., “On the optimization of two-component plates against ballistic impact”. *J Mater Process Technol*; 57(1–2):141–5, 1996.
- [28] Benloulo, I.S.C., Sánchez-Gálvez, V., “A New Analytical Model To Simulate Impact onto Ceramic/Composite Armors”, *Int. J. Impact Eng.*, v. 21, n. 6, pp. 461-471, 1998.
- [29] Ben-Dor, G., Dubinsky, A., Elperin, T., “Optimization of Two-Component Composite Armor Against Ballistic Impact”, *Composite Structures*, 69 , 89-94, 2004.
- [30] Nandlall, D., Williams, K., Vaziri, R. “Numerical Simulation of the Ballistic Response of GRP Plates”, *Composites Science and Technology* 58, 1463-1469, 1998.
- [31] Mahfuz, H., Zhu, Y, Haque, A., Vaidya, U, Jeelani, S, "Investigation of High Velocity Impact on Integral Armor Using Finite Element Method," *International Journal of Impact Engineering*, Vol. 24, No. 2, pp. 203-217, 2000.
- [32] Jovicic, J., Zavaliangos, A., Ko, F., “Modeling of the Ballistic Behavior of Gradient Design Composite Armors”, *Composites: Part A* 31, 773–784,2000.
- [33] Yen, C.F., “Ballistic Impact Modeling of Composite Materials”, 7th *International LS-DYNA Users Conference*, 2002.
- [34] “Ballistic Impact On Ceramic/Aramid Armour Systems”, Report-draft version, 2003.
- [35] Mahdi, S., J. W. Gillespie, Jr., “Finite Element Analysis of Tile-Reinforced Composite Structural Armor Subjected to Bending Loads,” *Composites Part B: Engineering*, Vol. 35, pp. 57-71, 2004.
- [36] Z. Fawaz, W. Zheng, K. Behdinan, “Numerical Simulation of Normal and Oblique Ballistic Impact on Ceramic Composite Armors”, *Composite Structures* 63 , 387–395, 2004.
- [37] Ala, T., Weitao, Y., Robert, G, “Non-linear Strain Rate Dependent Micro-Mechanical Composite Material Model for Finite Element Impact and Crashworthiness Simulation”, *International Journal of Non-Linear Mechanics* 40, 957 – 970, 2005.

- [38] Aydinel, A., Yıldırım, R. O. Ögel, B., “Numerical and Analytical Investigation of Al_2O_3 Ceramic-GFRP Composite Armor Systems Against 7.62mm AP”, USMOS 2005, ODTÜ, Ankara, June 2nd-3rd 2005.
- [39] Grujicic, M., Pandurangan, B., Zecevic, U., Koudela, K.L., Cheeseman, B.A., “Ballistic Performance of Alumina/S-2 Glass-Reinforced Polymer-Matrix Composite Hybrid Lightweight Armor Against Armor Piercing (AP) and Non-AP Projectiles”, [Multidiscipline Modeling in Materials and Structures](#), Volume 3, Number 3, pp. 287-312(26), 2007.
- [40] Asay, J.R., Shahinpoor, M., “High-Pressure Shock Compression of Solids”, Springer-Verlag New York, Inc., 1993.
- [41] Faik, S., Witteman, H., “Modeling of Impact Dynamics: A Literature Survey”, International ADAMS User Conference, 2000.
- [42] Achenbach, J. D., “Wave Propagation in Elastic Solids”, American Elsevier, New York, 1975.
- [43] Timoshenko, S.P., Goodier J. N, “Theory of Elasticity,” 3rd edition, McGraw Hill, New York, 1951.
- [44] Goldsmith, W., “Impact”, Edward Arnold Publishers, London, 1960.
- [45] Johnson, K. L., “Contact Mechanics”, Cambridge University Press, 1985.
- [46] Karman, T. von, Nat. Def. Res. Counc. Rep. A-29, 1942.
- [47] Taylor, G.I., British Ministry of Home Security, Civil Defense Rs. Comm. Rep. RC329, 1942.
- [48] Rakhmatulin, K.A., Prikl. Mat. Mekh., 9, 91; 1945.
- [49] Karman, T. von, Duwez, P., Journal of Applied Physics, 21,987, 1950.
- [50] Malvern, L.E., Journal of Applied Mechanics, Trans. ASME, 18, 203, 1951a.
- [51] Malvern, L.E., Quart. Appl. Math., 8, 405, 1951b.
- [52] Zukas, J.A., “Introduction to Hydrocodes”, Elsevier, 2004.
- [53] Ochoa, O.O., Reddy, J.N., “Finite Element Analysis of Composite Laminates”. Dordrecht: Kluwer Academic Publishers, 1992.
- [54] Reddy, J.N., “Energy and Variational Methods in Applied Mechanics”, John Wiley and Sons, New York (1984)

- [55] Lempriere, B.M., "Poisson's Ratio in Orthotropic Materials", AIAA J., 6 (11), 2226-2277, 1968,
- [56] Sierakowski, R.L., "Dynamic Loading and Characterization of Fiber-Reinforced Composites", John Wiley and Sons, 1997.
- [57] Dobyns, A.L., "Analysis of Simply Supported Plates Subjected to Static and Dynamic Loads", AIAA J., 19(5), 642-650, 1981.
- [58] Whitney, J.M. and Pagano, N.J., "Shear Deformation In Heterogeneous Anisotropic Plates", Journal of Applied Mechanics", 37, 1031-1036, 1970.
- [59] Sierakowski, R.L., Chaturvedi, S.K., "Dynamic Loading and Characterization of Fiber-Reinforced Composites", John Wiley and Sons, New York, 1997.
- [60] Abrate, S., "Impact on Composite Structures", Cambridge University Press, 1998.
- [61] Cook, R.D, Malkus D.S., Plesha, M.E., Witt, R.J., Concepts and "Applications of Finite Element Analysis", John Wiley and Sons, New York, 2002.
- [62] Tekkaya, E., "Explicit Finite Element Method", Seminar, 2006.
- [63] Century Dynamics, Inc., "AUTODYN Theory Manual, Century Dynamics, Inc., San Ramon, California, USA", 1999.
- [64] Century Dynamics, Inc., "AUTODYN Training Course, V6.0", Century Dynamics, Inc., San Ramon, California, USA, 2006.
- [65] Johnson, G.R., Cook, W.H., "A Constitutive Model and Data for Metal Subjected to Large Strains, High Strain Rates and High Temperatures", Proc. 7th Symp. on Ballistics, The Hague, The Netherlands, 541-547, 1983.
- [66] Johnson, G.R., Cook, W.H (1985). "Fracture Characteristics of Three Metals Subjected to Various Strains, Strain Rates, Temperatures and Pressures." Engineering Fracture Mechanics, 21(1), 31-48.
- [67] Holmquist, T.J., Johnson, G.R., "Response of Silicon Carbide to High Velocity Impact," Journal of Applied Physics, 91(9), 2002.
- [68] Johnson, G.R., Holmquist, T.J., "A Computational Constitutive Model for Brittle Materials Subjected to Large Strains, High Strain Rates, and High Pressures", Shock-Wave and High-Strain-Rate Phenomena in Materials, edited by M.A. Meyers, L.E. Murr, and K.P. Staudhammer, Marcel Dekker Inc., New York, pp. 1075-1081, 1992.

- [69] Hiermaier, S., Riedel, W., Hayhurst, C.J., Clegg, R.A., Wentzel, C.M., “Advanced Material Models for Hypervelocity Impact Simulations”, EMI-Report No. E43/99, ESA CR(P) 4305,1999.
- [70] Century Dynamics, Inc., “Composite Modeling in AUTODYN, Revision 1.0”, Century Dynamics, Inc., San Ramon, California, USA, 2005.
- [71] Resnyansky, A.D., “The Impact Response of Composite Materials Involved in Helicopter Vulnerability Assessment: Literature Review - Part 2”, Weapons Systems Division Defence Science and Technology Organisation, DSTO-TR-1842 Part 2, 2006.
- [72] Straßburger, E., Senf, H., Rothenhäusler, "Fracture Propagation During Impact in Three Types of Ceramics" Colloque C8, supplement au Journal de Physique III, Volume 4, septembre 1994.
- [73] Holmquist, T.J., Johnson, G.R., "Response of Silicon Carbide to High Velocity Impact," Journal of Applied Physics,91(9), 2002.
- [74] Holmquist, T.J., Johnson, G.R., Templeton, D.W., Bishnoi, K.D., “Constitutive Modeling of Aluminum Nitride for Large Strain, High Strain Rate and High Pressure Applications,” Int. J. Impact Engineering, 25, 211-231, 2001.
- [75] M.A. Meyers, Dynamic Behavior of Materials, Wiley, New York, 1994
- [76] Clegg, R., Hayhurst, C., Leahy, J., Deutekom, M., “Application of a Coupled Anisotropic Material Model To High Velocity Impact Response of Composite Textile Armour” 18th International Symposium and Exhibition on Ballistics, San Antonio, Texas USA, 1999.
- [77] Backman, M.E., Goldsmith, W., “The Mechanics of Penetration of Projectiles into Targets”, International Journal of Engineering Science, Vol. 16, pp. 1-99, 1978.
- [78]Yunus, E.K., “Low Velocity Impact Characterization of Monolithic and Laminated AA 2024 Plates by Drop Weight Test”, MSc. Thesis, 2003.
- [79] Lundberg, P., Renström, R., Lundberg, B., “Impact of Metallic Projectiles on Ceramic Targets: Transition Between Interface Defeat and Penetration”; International Journal of Impact Engineering, 24, 259-275, 2000.
- [80] Zukas, J.A., Jonas, G.H., “Mechanics of Penetration; Analysis and Experiment”, International Journal of Engineering Science, Vol. 16, pp. 879-903, 1978.
- [81] Mallick, P.K., “Fiber-Reinforced Composites, Materials, Manufacturing and Design”, Marcel Dekker,Inc.,1988.

[82] Chen, J.K., Medina D.F., “ The effects of Projectile Shape on Laminated Composite Perforation”, *Composite Science and Technology*, 58, 1629-1639. ,1998.